

AD-A264 728



2

WL-TR-93-7023

## A Ceramic Fracture Model for High Velocity Impact

William H. Cook

Wright Laboratory, Armament Directorate  
Munitions Division  
Warheads Branch  
Eglin AFB FL 32542-6810

DTIC  
ELECTE  
MAY 20 1993  
S A D

MAY 1993

FINAL REPORT FOR PERIOD OCTOBER 1985 - FEBRUARY 1993

Approved for public release; distribution is unlimited.

93 5 19 10 8

93-11261

WRIGHT LABORATORY, ARMAMENT DIRECTORATE

Air Force Materiel Command ■ United States Air Force ■ Eglin Air Force Base

## NOTICE

When Government drawings, specifications, or other data are used for any purpose other than in connection with a definitely Government-related procurement, the United States Government incurs no responsibility or any obligation whatsoever. The fact that the Government may have formulated or in any way supplied the said drawings, specifications, or other data, is not to be regarded by implication, or otherwise as in any manner construed, as licensing the holder, or any other person or corporation; or as conveying any rights or permission to manufacture, use, or sell any patented invention that may in any way be related thereto.

This technical report has been reviewed and is approved for publication.

The Public Affairs Office has reviewed this report, and it is releasable to the National Technical Information Service (NTIS), where it will be available to the general public, including foreign nationals.

FOR THE COMMANDER

*Martin F. Zimmer*

MARTIN F. ZIMMER  
Technical Director  
Munitions Division

Even though this report may contain special release rights held by the controlling office, please do not request copies from the Wright Laboratory, Armament Directorate. If you qualify as a recipient, release approval will be obtained from the originating activity by DTIC. Address your request for additional copies to:

Defense Technical Information Center  
Cameron Station  
Alexandria VA 22304-6145

If your address has changed, if you wish to be removed from our mailing list, or if your organization no longer employs the addressee, please notify WL/MNMW, Eglin AFB FL 32542-6810, to help us maintain a current mailing list.

Do not return copies of this report unless contractual obligations or notice on a specific document requires that it be returned.

REPORT DOCUMENTATION PAGE			Form Approved OMB No 0704-0188	
Public reporting burden for this collection of information is estimated to average 1 hour per response, including the time for reviewing instructions, searching existing data sources, gathering and maintaining the data needed, and completing and reviewing the collection of information. Send comments regarding this burden estimate or any other aspect of this collection of information, including suggestions for reducing this burden, to Washington Headquarters Services, Directorate for Information Operations and Reports, 1215 Jefferson Davis Highway, Suite 1204, Arlington, VA 22202-4302, and to the Office of Management and Budget, Paperwork Reduction Project (0704-0188), Washington, DC 20503				
1. AGENCY USE ONLY (Leave blank)	2. REPORT DATE May 1993	3. REPORT TYPE AND DATES COVERED Final, October 1985 - February 1993		
4. TITLE AND SUBTITLE A Ceramic Fracture Model for High Velocity Impact			5. FUNDING NUMBERS PE: 62601F PR: 2302 TA: BW WU: 11	
6. AUTHOR(S) William H. Cook			7. PERFORMING ORGANIZATION NAME(S) AND ADDRESS(ES) Wright Laboratory, Armament Directorate Munitions Division Warheads Branch (WL/MNMW) Eglin AFB FL 32542-6810	
8. PERFORMING ORGANIZATION REPORT NUMBER			9. SPONSORING / MONITORING AGENCY NAME(S) AND ADDRESS(ES) Same as Block 7.	
10. SPONSORING / MONITORING AGENCY REPORT NUMBER WL-TR-93-7023			11. SUPPLEMENTARY NOTES Availability of report specified on verso of front cover. This report not edited by TESCO, Inc.	
12a. DISTRIBUTION / AVAILABILITY STATEMENT Approved for public release; distribution is unlimited.			12b. DISTRIBUTION CODE A	
13. ABSTRACT (Maximum 200 words) The objectives of this research program were to develop, implement, and demonstrate a failure model for aluminum oxide ceramic under impact loading. A comprehensive test program for Coors AD-85 was conducted. Four types of experiments provided a basis for the development of the ceramic failure model. A phenomenological damage-based failure model for compressive fracture of impacted aluminum oxide was developed with emphasis placed on predicting fragment sizes of failed ceramic. Test data suggested a fragment size correlation with loading rate. A model was developed incorporating the data and implemented in the EPIC hydrocode. Comparisons of the results of this model to penetration test were positive.				
14. SUBJECT TERMS Ceramic, Fracture, Impact			15. NUMBER OF PAGES 184	
16. PRICE CODE			17. SECURITY CLASSIFICATION OF REPORT UNCLASSIFIED	
18. SECURITY CLASSIFICATION OF THIS PAGE UNCLASSIFIED		19. SECURITY CLASSIFICATION OF ABSTRACT UNCLASSIFIED		20. LIMITATION OF ABSTRACT UL

PREFACE

This report documents work performed by the author in partial fulfillment of the requirements for a Doctor of Philosophy degree at the University of Florida (UF). The work was performed at the Wright Laboratory, Armament Directorate, Munitions Division, Warheads Branch (WL/MNMW), Elgin AFB, Florida under the Air Force Office of Scientific Research (AFOSR) sponsorship, Work Unit 2302BW11, during the period from October 1985 through February 1993.

The author wishes to express his thanks to Dr. E. K. Walsh, dissertation advisor, for his support, encouragement, and valuable guidance throughout this research. The technical guidance and support provided by Drs. L. E. Malvern, M. A. Eisenberg, J. E. Milton, and K. J. Anusavice were also invaluable.

Special thanks are due to Dr. A. M. Rajendran of the University of Dayton Research Institute (UDRI) and Dr. T. Nicholas of the Wright Laboratory, Materials Directorate, Wright-Patterson AFB, Ohio. Their suggestions and insightful discussions regarding this research were largely responsible for its direction.

The experimental support of Dr. N. S. Brar, UDRI, and several colleagues in WL/MNMW including L. Wilson, T. Wallace, J. House, and L. Perillo is gratefully acknowledged.

The support of the management of the Armament Directorate was essential to the completion of this work, particularly Mr. Ron Boulet and Dr. Sam Lambert.

Finally, Lt Col G. Haritos and Dr. W. Jones of AFOSR are acknowledged for financial support throughout this program.

UNCLASSIFIED

iii/iv (Blank)

Accession for	
NTIS GRA&I	J
DTIC TAB	
Unannounced	
Justification	
3	
DTIC	
DTIC	
A-1	

## TABLE OF CONTENTS

Section	Title	Page
1	INTRODUCTION .....	1
	Background .....	1
	Objective .....	12
	Approach .....	13
	Hypothesis .....	13
	Experiments .....	14
	Quasi-static compressive tests .....	15
	Hopkinson bar tests .....	15
	Plate impact tests .....	15
	Rod-on-rod impact tests .....	16
	Penetration experiments .....	16
	Theoretical .....	16
	Computational .....	17
	Overview .....	18
2	THE MECHANICS OF PENETRATION .....	20
	Penetration Mechanics .....	20
	Classifications .....	20
	Analysis Methods .....	22
	Empirical models .....	23
	Analytical models .....	23
	Hydrocodes .....	24
	Processes for Penetration of Confined Ceramics ..	26
	Failure and Penetration .....	27
3	FRACTURE MODELS .....	29
	General Fracture Models .....	29
	Plasticity Based Models .....	29
	Nucleation and Growth Models .....	33
	Fragmentation Models .....	37

TABLE OF CONTENTS (Continued)

Section	Title	Page
	Compressive Fracture Mechanisms .....	43
	Ceramic Impact and Fracture .....	47
	Ceramic Fracture Models .....	52
4	MATERIAL DATA .....	57
	Mechanical Properties of Alumina .....	57
	Micrographic Study of Undamaged Ceramic .....	58
5	EXPERIMENTS .....	63
	Experimental Program .....	63
	Instron Tests .....	63
	Hopkinson Bar Tests .....	64
	Plate Impact Tests .....	74
	Rod-on-rod Impact Tests .....	81
	Penetration Experiments .....	94
6	ANALYSIS OF EXPERIMENTS .....	96
	Micrographic Study of Damaged Ceramic .....	96
	Crack sizes and distribution .....	96
	Failure surface analysis .....	102
	Damage as a Function of Loading .....	102
7	PROPOSED FAILURE MODEL .....	110
	Discussion .....	110
	Proposed Model .....	112
	Determination of Constants .....	119
	Implementation .....	120
	Model Limitations .....	121
8	COMPUTATIONAL PROGRAM .....	124
	Model Implementation in EPIC-2 Hydrocode .....	124
	Summary of Calculations .....	127
	Hopkinson Bar Analysis .....	129
	Computational Model .....	129
	Strain Rate Effect .....	136
	Fracture Predictions .....	142
	Plate Impact Analysis .....	145
	Computational Model .....	145
	Fracture Predictions .....	146
	Rod-on-rod Impact Analysis .....	150
	Computational Model .....	150
	Fracture Predictions .....	150
	Penetration Predictions .....	156
	Computational Model .....	156
	Fracture Predictions .....	157
	Zone Size Study .....	158

TABLE OF CONTENTS (Concluded)

Section	Title	Page
9	SUMMARY AND CONCLUSIONS .....	161
APPENDIX	DETERMINATION OF MATERIAL CONSTANTS .....	163
REFERENCES	.....	166

## LIST OF FIGURES

Figure	Title	Page
1	Hydrocode Calculation With Mohr-Coulomb Model . . . .	7
2	Low Velocity Penetration Experiment . . . . .	9
3	Penetration Experiment . . . . .	11
4	Five Stages of Ceramic Penetration . . . . .	25
5	Mohr-Coulomb Model . . . . .	32
6	Crack Size vs. Load and Duration . . . . .	36
7	Fragmenting Body for Grady Fragmentation Model . . .	38
8	Development of Cracks Under Compressive Load . . . .	43
9	Goodier's Mechanism . . . . .	44
10	SEM Photomicrograph of Typical Void Structure . . . .	59
11	TEM Photomicrographs of Baseline Materials (a) Twinning in alumina grains (b) Dislocation in alumina grains . . . . .	60
12	Optical and SEM Photomicrographs Baseline Material (20X, 120X, 1000X, and 2500X) ..	61
13	Split Hopkinson Pressure Bar Apparatus . . . . .	65
14	Miniature Compressive Test Specimen . . . . .	66
15	Fixture for Hopkinson Bar . . . . .	66
16	Hopkinson Bar Test 19 Incident Stress . . . . .	69
17	Hopkinson Bar Test 19 Transmitted Stress . . . . .	69
18	Hopkinson Bar Test 19 Detailed Stress . . . . .	70
19	Hopkinson Bar Test 18 Detailed Stress . . . . .	70
20	Transmitted Stresses in Tests 6-8 . . . . .	71

LIST OF FIGURES (Continued)

Figure	Title	Page
21	Compressive Stress vs. Strain Rate .....	73
22	Low vs. High Strain Rate Failed Compressive Specimen (4X) .....	73
23	Plate Impact Setup .....	75
24	Plate Impact Test Hardware .....	76
25	Original Plate Impact Test Hardware .....	77
26	Spall Strength vs. Shock Stress .....	77
27	Compressive Stress Achieved Based on Hugoniot's ...	80
28	Compressive Stress as a Function of Impact Velocity .....	80
29	Rod-on-rod Test Apparatus .....	82
30	Rod-on-rod Impact Test Specimen .....	83
31	Rod-on-rod Impact, 500,000 Frames/Sec (Tests 7, 10, 13, and 14) .....	87
32	Stress vs. Time in Target Rod for Test 6 .....	92
33	Stress vs. Time in Target Rod for Test 22 .....	92
34	Measured Stresses in Rod-on-rod Impact Experiments .....	93
35	Penetration Experimental Setup .....	95
36	Optical and SEM Photomicrographs 343,000 psi (20X, 120X, 1000X, and 3000X) .....	98
37	Optical and SEM Photomicrographs 361,000 psi (20X, 120X, 1000X, and 3000X) .....	100
38	Post Test Porosity of Compressive Specimens .....	103
39	Typical Plate Impact Damage at 52.3X Magnification .....	104
40	Damage in Impacted Plates vs. Load Magnitude .....	105
41	Damage in Impacted Plate vs. Load Duration .....	106
42	Damage in Impacted Plate vs. Impactor Material ....	107
43	Crack Surface Area vs. Load Pulse Magnitude .....	108

LIST OF FIGURES (Continued)

Figure	Title	Page
44	Crack Surface Area vs. Load Pulse Duration .....	109
45	Proposed Failure Model .....	115
46	Hopkinson Bar Calculational Configuration .....	132
47	Stress Field in Specimen at 4 microseconds .....	133
48	Stress versus Time at Stations A, B, C, and D in Test 1 .....	134
49	Hopkinson Bar Calculation, Test 6, Stress Field for Strain Rates of 600 sec <sup>-1</sup> and 800 sec <sup>-1</sup> .....	137
50	Stress Histories at Station E .....	139
51	Strain Rate Histories at Station E .....	140
52	(Mean Pressure/Axial Stress) Histories for Station E .....	141
53	Transmitted Stress - Hopkinson Bar Calculation, Test 1 .....	143
54	Failure Contours in Split Hopkinson Bar .....	144
55	Plate Impact Calculational Configuration .....	145
56	Contours of Stress for Plate Impact Test 1 .....	147
57	Time History for Element in Plate - Strain Rate, Pressure, and Axial Stress for Station E .....	148
58	Calculated vs. Experimental Fragment Sizes .....	149
59	Rod-on-Rod Calculation, Test 14 .....	149
60	Rod-on-Rod Calculation, Test 6 .....	152
61	Rod-on-Rod Calculation, Test 22 .....	152
62	Calculated Rod Impact Sequence .....	153
63	Recovered Target Rod Damage .....	154
64	Calculated Target Rod Damage .....	154
65	Calculated Axial Stress, Test 22 .....	155
66	Calculated Axial Stress, Test 6 .....	155

LIST OF FIGURES (Concluded)

Figure	Title	Page
67	Penetration Computational Configuration .....	157
68	Calculation of Penetration Test .....	159
69	Zone Size Study for Penetration .....	160

## LIST OF TABLES

Table	Title	Page
1	Test Plan .....	14
2	AD85 Material Properties .....	47
3	Availability of Material Data .....	58
4	Servohydraulic Compressive Tests .....	64
5	Hopkinson Bar Compressive Tests .....	68
6	Pore Size after Compressive Loading .....	74
7	Material Properties for Stress Predictions .....	81
8	Plate Impact Tests .....	81
9	Rod-on-rod Impact Tests .....	84
10	Confined Ceramic Penetration Experiments .....	94
11	Crack Surface Area and Fragment Data .....	108
12	Model Characteristics .....	123
13	Data Used in Computational Models .....	126
14	Summary of Calculations .....	128

CHAPTER 1  
INTRODUCTION

Background

A topic of long-standing interest to military engineers and of recent interest to spacecraft designers has been the ability of a structure to withstand impact of a projectile and prohibit penetration or the generation of lethal debris spalling from the rear surface. In the fifties and sixties, materials technologies were successfully exploited to develop highly effective lightweight protective shields and body armors manufactured from laminated metals, metals and ceramics, or composite materials such as Kevlar. Such designs are exemplified by reentry vehicle heat shields, meteorite shields in spacecraft, and lightweight armors employed by the military. More substantial penetration shields such as heavy mobile ground armors employed in armored vehicles also benefit from careful selection of materials and construction of specialized lightweight armors. The extension of knowledge from thin protective shields to thick protective shields is not simple, and the ability to design or defeat such shields requires a thorough understanding of the basic physical processes of fracture and high loading rate material behavior. One of many

protective systems of interest is a system of ceramic sandwiched between metal plates.

Many types of ceramics are available to the designer interested in developing impact resistant structures. The broad classification of ceramic materials includes materials containing phases which are compounds of metallic and non-metallic elements, including such diverse substances as glass, brick, stone, concrete, porcelain, refractory materials, special magnetic core materials, etc. [1]. Two large classes of ceramic materials are of particular importance regarding their impact response. High temperature, high strength ceramics have received a great deal of attention for ultrahigh velocity impacts because of the requirement of space vehicles to withstand meteorite impact as well as survive heating during re-entry [2]. High strength and high toughness ceramics have also received much attention as candidate materials for armor. Armor ceramics typically include inexpensive, readily available, and reasonably tough ceramics such as aluminum oxides, titanium diborides, beryllium oxides, etc.

The damage and subsequent fracture of ceramics when subjected to impulsive loading are critical factors in analyzing the failure of protective systems. The impact of a moving mass and penetration of a ceramic employed as a protective shield results in a complex sequence of processes. Confined ceramics are most effective in stopping

penetration. The confinement contains the ceramic as it fractures on impact. It also complicates the entry and exit phases because of added interfaces and the structural aspect of the confining materials. Degradation of the structural properties of the ceramic is important to understanding the penetration process, leading to a need to predict the failure of ceramics in a way that provides information on the timing of the failure, the energy consumed in the failure process, and the size of the fragmented material. Fracture models that employ damage concepts appear more relevant than crack growth models for this application.

This research adopts existing fracture model concepts and extends them through applications in an existing finite element continuum mechanics code (hydrocode) to the prediction of the damage and fracture processes for one ceramic (Coors AD85 alumina). The basis for the extension is property determination by experiments including compressive tests, instrumented plate impact tests, and rod-on-rod impact tests. Experiments with metal rods penetrating confined ceramic plates are then used to test the predictions of the model. The objective is improved understanding of the damage and failure process for ceramic as demonstrated by better penetration predictions. Emphasis is placed on compressive failure.

Wilkens performed extensive pioneering research dealing with a computational approach to the treatment of

penetration of thin ceramic laminate armors [3]. He employed two-dimensional hydrocodes with simplified fracture criteria to evaluate characteristics of a desirable ceramic armor. These criteria were

- (1) fracture initiates on the surface
- (2) a maximum principal stress greater than 45,000 PSI in tension causes fracture
- (3) there is a time delay for the complete fracture of a zone
- (4) a fractured zone becomes a source for fracture of neighboring zones
- (5) fracture occurs only within a range of distance equal to or less than the time step times the crack velocity in the ceramic

Wilkins' work considered alumina among other materials. A notable achievement was his flash x-ray coverage of the penetration process, illustrating damage profiles with very good comparison between computationally predicted damage and experimental results. Among other conclusions, Wilkins noted the importance of the time scale of the break-up of the ceramic on the penetration result.

Mayseless et al. [4] reported on experimental research on the penetration response of confined ceramics. They performed an extensive set of experiments (approximately 150) with the objective of, "[providing] reliable data on the ballistic performance of the ceramic targets and the projectile erosion in order to create a basis for the development of an analytical model of the process" [4, p. 373]. The work extended Wilkins' earlier work, concluding that for thin confined ceramic plates at velocities below

250 meters/second a simple metal plate is more effective at resisting penetration from hardened, pointed penetrators, while above 250 meters/second a single confined ceramic plate is more effective. Based on assumptions of particle size distributions for the fractured ceramic and based on the assumption that the work of erosion equals the product of the yield strength and the volume of target removed, they concluded that, "the fracture of the ceramic consumes a negligible amount of energy compared to that required for erosion" [4, p. 378]. A simple model for penetrator erosion was presented assuming no wave propagation, a linear mass loss of the projectile during penetration, and a force history derived from displacement measurements. The model was found to be accurate in the lower velocity range of this work.

Mescall and Tracy [5] investigated the selection of ceramic material for application in armors. They implemented the model proposed by Griffith [6] in a version of Wilkens' HEMP hydrocode, and observed that properly treating the compressive brittle failure of the ceramic is critical to modeling correctly the penetration process. The following observations are quoted directly from their conclusions:

- (1) Compressive strength of ceramics is an important parameter for optimal ballistic performance. Fracture under triaxial compression conditions appears to occur prior to tensile fracture; it also occurs in a region close to the penetrator.
- (2) The range of tests of ceramic materials under

triaxial compression needs to be extended to states which better define fracture in the compressive quadrant. Systematic variations of . . . [maximum and minimum principal stresses]. . . are needed.

- (3) The ability of broken, even rubblized, ceramic to resist compressive loading and to erode a penetrator is a critical parameter in assessing ballistic performance. Considerable attention should be given to this problem which presently is ill-defined.
- (4) The role of high rates of loading on the failure locus has not been explored, yet such data is quite important.
- (5) More and better direct experimental observations of fracture under ballistic conditions are needed. Both flash X-rays of opaque targets and photographic observations of transparent ones would be useful [5, pp. 12-13].

Penetration mechanics dealing with confined ceramic targets is a developing science. A better understanding of the failure process is required at both the level of mechanisms involved and the mechanics of the failure process. This includes understanding the speed of propagation of a damage zone, the processes occurring in the active damage zone, and the size of fragments generated (perhaps as a function of energies associated with the impact). Also, improved material properties data are required for the post-fractured ceramic material. In order to predict penetration response of the post-fractured ceramic, improved granular material models are necessary for use in continuum mechanics codes. In order to apply Lagrangian hydrocodes where the fixed-in-material reference frame can most accurately track the small energy differences involved in the fracture processes, improved computational

methods are needed to treat the penetration and target interface (enhanced slide line techniques or entirely new boundary element methods.) The use of damage tracking failure models in Eulerian hydrocodes demands more attention to improved advection schemes and experience with transporting measures of damage successfully from one element to another in a laboratory, fixed-in-space reference frame.

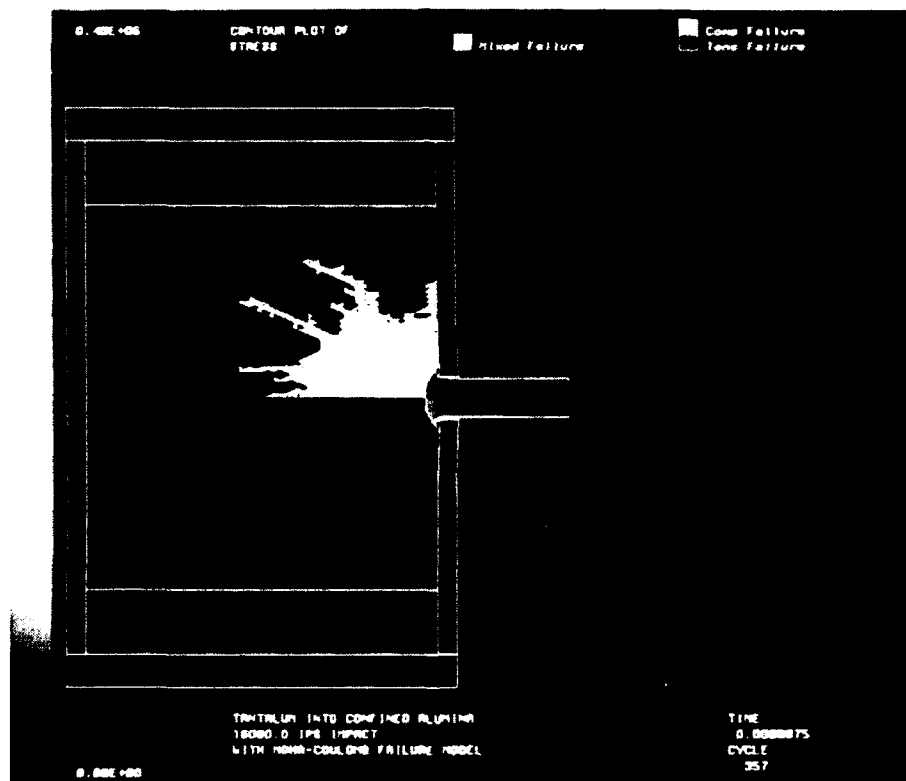


Figure 1. Hydrocode Calculation With Mohr-Coulomb Model

The need to identify and understand the failure mechanisms is fundamental to the understanding of the penetration process. Figure 1 illustrates a hydrocode calculation of a penetration process modeled with a simple Mohr-Coulomb failure surface. This figure is similar in layout to several other figures presented in Chapter 8. Since all calculations are for two-dimensional axisymmetric configurations, the upper and lower parts of the contour plots can be used to show different variables, recognizing that each of the variables is valid reflected about the axis. The lower half shows complete contours of the variable defined in the upper left corner (stress), over a range described by the bar on the left (0 to 400,000 PSI). The upper half of the figure shows failure contours filled with white for failure where principal stresses are all compressive, grey where principal stresses are of mixed sign, and black with a white outline where principal stresses are all tensile. The meaning of each color is indicated by the failure legends on the top of the figure. Unfailed regions in the upper half of the figure do not show the contour values shown in the lower half of the figure in order to highlight the failure zones. The original analysis of these contour plots employed a color range for the variable shown in the lower half of the plot, rather than the grey scale required for publication. Considerable loss

of detail in the contours resulted from the use the grey scale, but the discussions of contours was retained based on analysis from the color plots.

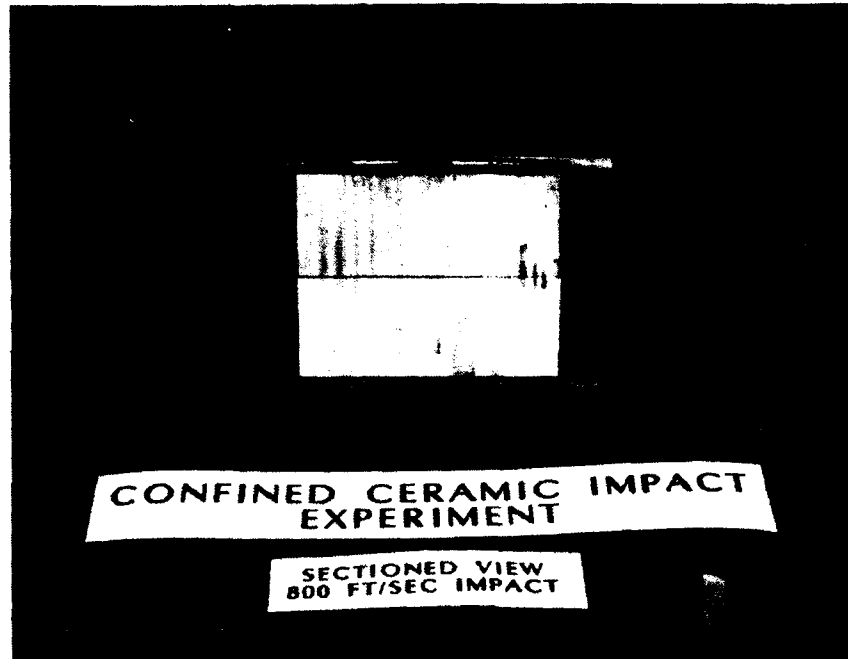


Figure 2. Low Velocity Penetration Experiment

All contour plots show an impactor on the right side of the figure moving to the left into a target material. For the calculation in Figure 1, a one inch long by 0.3 inch diameter tantalum rod in the center is moving to the left at 16080 inches per second. It is impacting a confined ceramic block surrounded by a preperforated front plate of aluminium, an aluminum backplate, an epoxy ring around the sides (top and bottom), and an outer steel ring on the sides. Differences in tensile, compressive, and mixed

compressive and tensile stress conditions at failure are shown to illustrate the conditions occurring at different positions in the target.

Figure 2 shows the actual experimental hardware for a low velocity impact where no ceramic damage occurred, and Figure 3 shows experimental results for a similar configuration where the impact velocity was sufficient to cause some failure in the target. The test in Figure 3 corresponds to the calculation in Figure 1. Both figures show similar experimental configurations with a one inch long projectile fired through a predrilled hole in an aluminum cover plate. Confinement on all sides was provided with steel momentum trapping plates. The target was carefully sectioned with an oil cooled diamond saw. Coloration of the cracked areas is oil residue from the sawing process.

For impact velocities above those in Figure 3, the target was recovered as powder and rubble. The simple Mohr-Coulomb model allowed the role of the compressive failure of the ceramic to be observed. These calculations confirm the observations of Mescall and Tracy, and demonstrate that a Mohr-Coulomb model provides comparable results to the Griffith model they employed. Compressive failure is evidently a very critical process in the penetration of confined ceramics at high velocity impact. The importance

of compressive failures in brittle materials in general has also recently been emphasized by a National Material Advisory Board report [7].

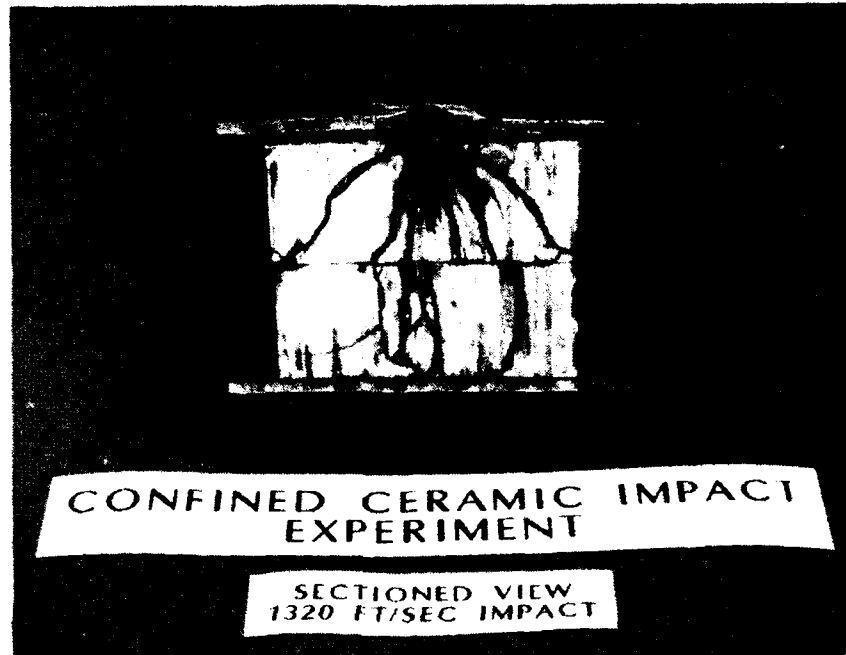


Figure 3. Penetration Experiment

Several aspects of the failure of ceramics under impulsive loading require research in order to model adequately the penetration process of confined ceramic plates. One of the most critical research needs is in the understanding of the damage and fragmentation process of the material in order to express the post-fractured material in terms of a range of particulate sizes. This understanding should lead to models useful in continuum mechanics wave propagation codes.

A very desirable aspect of this modeling would be directly relating physical material property inputs to the fracture process. For example, void and inclusion characteristics based on statistical data from micrographic examinations of material specimens could provide typical initial nucleation sites. In order for such material properties to be employed in fracture models, a framework must be provided to allow micromechanical processes to be considered in continuum mechanics treatments. In lieu of detailed micromechanical models, improved phenomenological models would contribute significantly.

#### Objective

The objective of this program was to develop and implement a physically based fracture model to permit both compressive and tensile failure of ceramic to be predicted under high velocity impact loads. The program employed an experimental and computational approach. Emphasis was placed on extending current concepts to consider fully compressive failure and accurately predict resultant fragment particle size distributions. For the compressive failure, experimental methods were developed and data gathered to permit verification of this model for a widely available alumina ceramic. The model was validated by implementation in a two-dimensional hydrocode and demonstrated as applied to a penetration problem.

### Approach

Alumina (Coors AD85) was selected as the ceramic of interest in this program because of its ready availability, widespread use, and the amount of research and testing already performed on this material. The approach involved experimental, theoretical, and computational aspects, but experiments and computational analysis predominated. The aspects of each phase of the research are discussed below following a discussion of the hypothesis that determined the approach to be taken.

### Hypothesis

Compressive damage of ceramic under impact loading can be critical to the failure process, and the final damaged state of the ceramic can be critical to any processes of penetration through the ceramic. Confining pressure and high rates of strain are major factors contributing to the response of both unfragmented and fragmented ceramic. In unfragmented ceramic, magnitude and duration of load both contribute to crack initiation and growth at multiple sites. Crack interactions and directionality of failure may be important, but their importance is secondary, so that useful models may be developed without treating these aspects directly. The ceramic is assumed to be an elastic, homogeneous, isotropic material before failure, and an isotropic, frictional material after failure.

### Experiments

Five types of laboratory experiments were conducted: servohydraulic compressive tests (Instron machine), Hopkinson bar tests, plate impact tests, rod-on-rod impact tests, and penetration experiments. A brief summary of each type of test and its objective is outlined below, with specific details discussed in Chapter 5.

Table 1. Test Plan

Test Summary	
Test Description	Number of Tests
Compressive Loading	
Servohydraulic	13
Hopkinson Bar	20
Plate Impact	13
Rod-on-rod Impact	
0.3 Inch Diameter	19
0.5 Inch Diameter	3
Penetration	9

Table 1 provides a comprehensive summary of the tests for the AD85 specimens. Nondestructive test methods including x-rays, magnafluxing, and optical surface examination ensured that the specimens contained no major flaws and were undamaged during sample preparation. All specimens were carefully machined from a single hot pressed plate that initially measured 0.75 inches by 12.0 inches by 12.0

inches. Ceramic target plates in the penetration experiments were cut from plates taken from the same production lot.

#### Quasi-static compressive tests

A standard servohydraulic material test system under crosshead displacement control was used to measure compressive stress-strain curves under quasistatic and intermediate strain rates.

#### Hopkinson bar tests

Hopkinson pressure bar experiments were performed to determine dynamic strength at high rates of loading and to create controlled loading conditions for evaluation of damage states in test materials.

#### Plate impact tests

Plate impact tests using metallic flier plates against encapsulated alumina targets were used in plate impact recovery experiments to evaluate fracture response due to uniaxial strain loading (compressive failure under dynamic loading with confining pressure.) The method of Rosenberg [8] was initially used to determine peak stresses. After confirmation that stresses were predictable based on impact velocity measurements, the manganin gages were deleted to reduce test complexity. Plate impact tests were not used to obtain Hugoniot Elastic Limit data and spall strength signals, because adequate previous tests were available in this area.

### Rod-on-rod impact tests

Rod-on-rod impact tests using 30 caliber alumina rods launched from an air gun against similar stationary alumina rods were used to evaluate fracture under mixed stress loading and to provide supplemental information on high strain rate strength. Similar tests with 50 caliber rods were performed to observe scaling effects. An arrangement using one ceramic rod impacting a similar ceramic rod was used to simplify analysis of the results. Front lighting with high speed photography was used to observe fracture propagation in the rods. Embedded manganin gages at multiple locations in the stationary rod provided direct measurements of stress histories. Surface mounted strain gages were also used to supplement the manganin stress gages.

### Penetration experiments

Gun launched projectiles were fired at confined ceramic assemblies in field tests to observe the macroscopic characteristics of the penetration response of confined ceramic. Recovered assemblies were sectioned and examined for fracture patterns. Instrumentation was limited to velocity measurements at the impact point.

### Theoretical

This program originally was expected to extend the microstatistical fracture mechanics methods popularized by Curran and associates at SRI to the compressive fracture of

confined alumina ceramics. These methods, described as nucleation and growth models, are built on the observation that material failures occur from the growth of either cracks or voids that nucleate from "heterogeneities on the scale of the graininess of the solid where the material no longer appears to be a continuum" [9, p. 256]. In ceramics, flaws might be considered as heterogeneities with sizes on the order of the alumina grain sizes. Nucleation data are generated from the plate impact tests such as those described above, provided that sufficient information can be obtained to generate nucleation rates as functions of stress or strain. The tests performed on alumina did not provide acceptable data for a microstatistical model. Damage was never stopped at intermediate states during the dynamic tests, so direct observations of damage from stopped tests were not possible. Instead, the fragmentation data were reduced and correlated to an energy balance model for the prediction of fragment sizes under dynamic loads, and the fragment size predictions were proposed as a basis for selecting a yield surface in a frictional model representing the post-fractured ceramic.

#### Computational

A modified version of the two-dimensional explicit finite element code EPIC-286 was used in this program [10,11]. EPIC is an acronym for Elastic Plastic Impact Computations, and it is a large program of approximately 12,000 lines of

FORTRAN. EPIC provides a first order accurate solution to the equations of conservation of mass, momentum, and energy subject to material equations of state and constitutive laws. EPIC was modified to provide constitutive and fracture models suitable for ceramics. Throughout this work, either triangular or quadrilateral element types were used in the axisymmetric 2D mode. The development of a fracture model suitable for implementation in this type of continuum mechanics code was a major part of the challenge of this research. The unfailed ceramic material was treated as an elastic Hookean solid, utilizing the dynamic material data generated in the test program outlined above. Several simple fracture models were implemented and compared to experimental results, leading to a proposed comprehensive model.

#### Overview

The next Chapter provides further background on the mechanics of penetration, emphasizing the need for ceramic penetration research. Chapter 3 discusses general fracture models and concludes with the present status of ceramic fracture models implemented in hydrocodes. Chapter 4 provides a review of the current availability of material properties for ceramics, leading to the experimental program described in Chapter 5. The results of the experiments are analyzed in Chapter 6, leading to a proposed failure model that is described in Chapter 7. Chapter 8 discusses the

calculational implementation of the proposed model and applications of that model to the experimental configurations. Chapter 9 summarizes the research with conclusions and recommendations.

CHAPTER 2  
THE MECHANICS OF PENETRATION

Penetration Mechanics

Classifications

Penetration mechanics is a relatively mature field. For simple geometries with a metallic penetrator and a metallic target, the field is complete with well documented techniques and well characterized mechanical processes. Many references are available summarizing the current state of the art in penetration mechanics, including the extensive works by Bachman [12], Bachman and Goldsmith [13], Zukas et al. [14], and the course notes from the penetration mechanics short course offered by Southwest Research Institute [15].

There are several useful methods of categorizing penetration. Categorization by impact speed often considers three velocity regimes of interest:

- (1) low velocity (0-1000 meters/second, where structural response is very important)
- (2) intermediate to high velocity (1000-10,000 meters/second where strength and failure properties of materials are significant)
- (3) hypervelocity (10,000-40,000 meters/second, where hydrodynamic behavior predominates and material phase changes become important)

The predominant field of current interest for ceramic protective systems (armors) is for high velocity

penetration. This range of velocities from 1,000 to 10,000 meters/second includes most gun launched or otherwise propelled kinetic energy penetrators as well as chemical energy penetrators such as shaped charges and explosively formed projectiles.

As another means of categorizing penetration, the evaluation of the penetration capabilities of projectiles against armors is frequently performed by considering the phases of the penetration process, consisting of three phases:

- (1) front surface entry
- (2) steady state penetration
- (3) exit from the rear surface

These phases are well documented for solid projectiles penetrating monolithic metallic armors. The processes are greatly complicated for multi-constituent metallic armors or spaced plate metallic armors. Processes are even more complex for non-metallic armors. The importance of each phase is dependent on the target, often characterized as one of the following:

- (1) semi-infinite (no rear surface effects)
- (2) thick (very small rear surface effects)
- (3) intermediate (rear surface effects have a direct effect on performance)
- (4) thin (no stress or strain gradients occur through the thickness of the target plate)

Several types of failure modes occur in impacted armor. Historically these have been categorized as:

- (1) brittle fracture
- (2) ductile hole growth
- (3) radial fracture
- (4) plugging
- (5) fragmentation
- (6) petaling

The historical emphasis on monolithic metallic armors is clear by this list of failure modes. These failure modes may occur independently or in combination. Differentiation between failure modes and failure mechanisms is important. Some of these categories of failure modes might also be considered to be failure mechanisms, while other failure modes are simply different physical responses embodying the same failure mechanisms. That is, the number of failure mechanisms might usefully be limited to some smaller number of failure mechanisms than the six failure modes outlined above. Some researchers have suggested that ductile spherical void growth, adiabatic shear banding, and brittle penny shaped crack growth are a sufficient number of basic mechanisms to adequately cover the failure response of metallic armor materials. Mechanisms involved in ceramic failure are less clear.

#### Analysis Methods

The methods of predicting if a penetrator will defeat a target by the process of penetration generally include:

- (1) empirical models
- (2) analytical models
- (3) hydrocodes

### Empirical models

Empirical models are often used to establish the size of an armor system based on knowledge of potential impactor size and velocity. Empirical models are also widely used by the vulnerability assessment community to accurately evaluate the performance capabilities of specific weapon systems against specific targets, as long as the penetrators and targets fall within the range of available data that exists for that purpose. The difficulty with purely empirical models is the availability of a data base that is directly applicable. Frequently extrapolation of these data bases leads to questionable performance predictions.

### Analytical models

Analytical penetration models perform an important role in both armor and penetrator design processes, since these models offer a simplified and easily managed approach to the problem by using greatly simplified treatments of many of the important physical processes involved. These models are primarily one-dimensional and occasionally two-dimensional. The models are generally of the type that rely on streamlined flow assumptions for both the armor and penetrator materials, leading to relatively accurate predictions of penetration against semi-infinite armors. Often strength properties of both the penetrator and armor are considered by adjustments to the models using a material constant referred to as the dynamic yield strength of the

materials involved. In these models, however, the dynamic yield strength required to obtain agreement with experiments is seldom consistent with directly measured dynamic yield strength. In essence, geometric aspects of the problem are also often embedded in these material constants, placing a burden on the user of the models to know how to select these values without simple, direct laboratory measurements of the material properties. An example of this class of model developed for ballistic penetration of ceramic armor is the model presented by Ravid, Bodner, and Holzman [16]. Their model assumes a rigid body penetrator and breaks the penetration process into five stages as shown in Figure 4.

#### Hydrocodes

The term hydrocode encompasses both Lagrangian (fixed in material) and Eulerian (fixed in space) continuum mechanics codes capable of treating highly dynamic processes such as impact, penetration, and explosions. These codes accurately treat wave propagation through materials, based on first principles of conservation of mass, momentum, and energy subject to material equations of state and constitutive models. The term hydrocode is in fact a misnomer at present, because virtually all codes of this class embody strength of material capabilities and hence are no longer limited to only hydrodynamic material response.

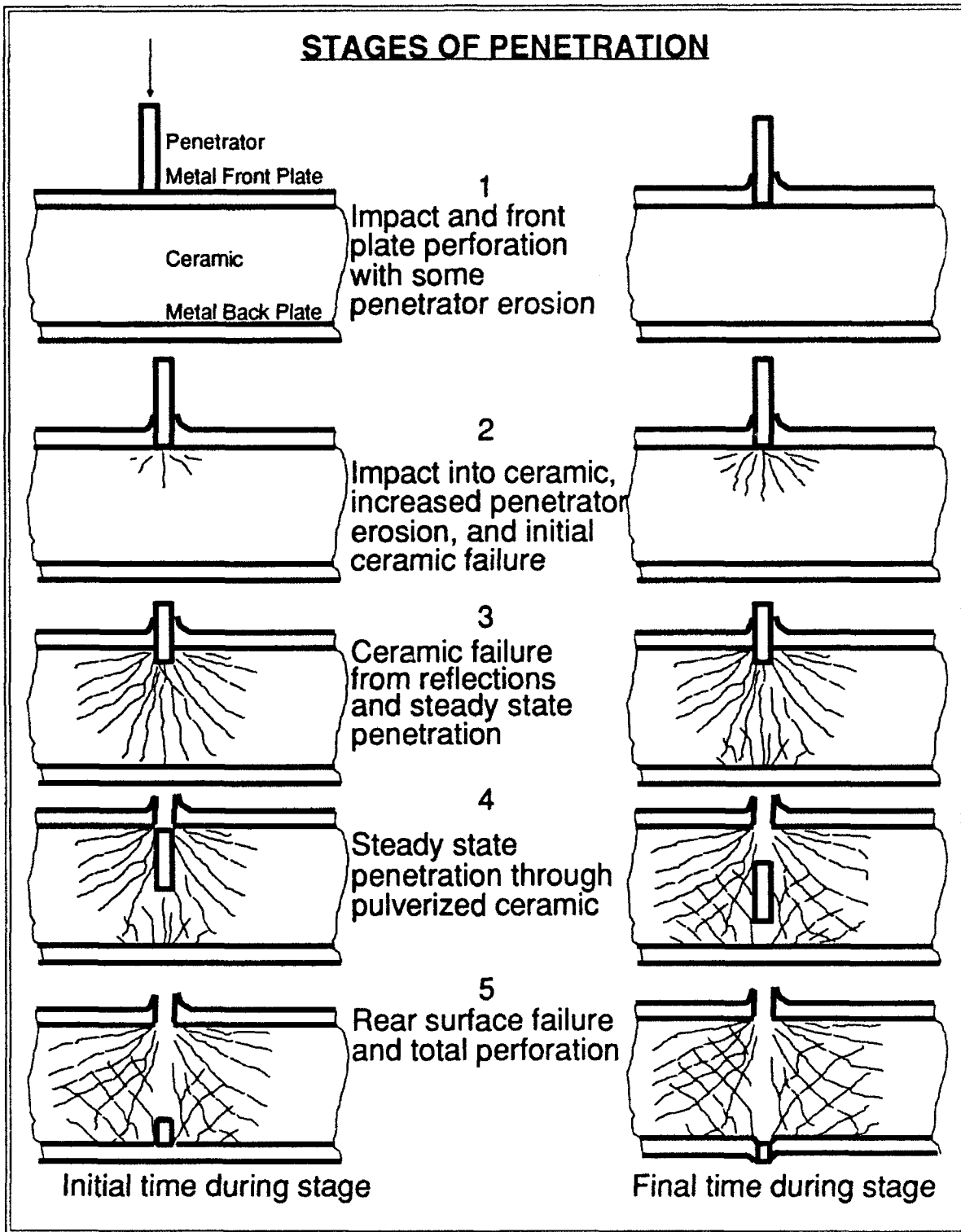


Figure 4. Five Stages of Ceramic Penetration

Two-dimensional hydrocodes have performed an increasingly useful role in evaluating penetration processes as material modeling capabilities have improved and costs of computing have become competitive with testing. These continuum mechanics codes allow treatment of axisymmetric penetration processes through very complex armors with first principles treatment of the process, subject to the quality of the material models and the numerical methods involved.

Three-dimensional hydrocodes have been of limited utility until the advent of class six and class seven supercomputers allowed the carefully selected applications of these immense calculations. Much work remains to be done in materials model development using two-dimensional codes before the routine use of three-dimensional codes is reasonable.

#### Processes for Penetration of Confined Ceramics

The processes for penetration of ceramic materials confined in a ductile metal surround are much more complex than penetration of monolithic metallic armors. This area of penetration mechanics is relatively new, with neither well documented techniques nor well characterized mechanical processes. Rapid erosion of the front plate directly loaded by the penetrator results in contact with the extremely hard ceramic material. This material has a significantly higher sound speed than the confining metal, so stress waves moving through the ceramic along the front plate interface load the front plate from behind. Damage occurs to the ceramic as

the compressive pulse moves through it, even before the penetrator has come in contact with the ceramic. High velocity impact results in axial compressive stresses even higher than the very high compressive strength of the ceramic, and further damage occurs as multidimensional geometry effects cause hoop and radial tensile regions ahead of and around the penetrator, resulting in potential failure in tension. Treatment of different failure mechanisms in the compressive loading phase and the tensile phase may be critical to understanding and predicting the penetration process. Reflected tensile loading from the rear plate interface and the rear surface of the armor structure adds to the tensile failure processes. Bulking of the ceramic material as it fractures alters the loading on the penetrator and creates a "structural response" of the armor system. The penetrator moves through a particulated ceramic material with highly erosive characteristics because of its hardness. The ceramic varies in size from powder, to sand-like, and finally to a rubble at greater distances from the impact point. Bulging of both the front and the rear surfaces is pronounced because of the bulking of the ceramic. A critical feature is the size of the ceramic particles during the penetration process.

#### Failure and Penetration

From the discussion above, it is clear that the failure process in the ceramic is the earliest phase of confined

ceramic penetration that is not well understood. Also, the accurate treatment of the failure process is essential to the later stages of penetration. The background discussed in Chapter 1 suggested several shortcomings in the prediction of penetration response of confined ceramics, but the first weakness is the failure process in the ceramic. Failure predictions in ceramic were therefore central to this research, and are discussed in the next chapter.

CHAPTER 3  
FRACTURE MODELS

General Fracture Models

The fundamentals for understanding the fracture processes in all materials are found in the pioneering research done by Griffith [17]. Based on the concept that a crack will grow when the energy required to increase the crack surface area is exceeded by the strain energy in a body, Griffith's work led to the field of linear elastic fracture mechanics (LEFM). Griffith established the LEFM concepts for brittle failures, but it later became apparent that the concepts are appropriate for elastic fracture of ductile materials as well. The extension of this work to include the plastic zone at the crack tip leads to the currently highly active area of elastic plastic fracture mechanics (EPFM). Crack branching and multiple crack interactions also are highly active research areas. The extremely large number of cracks formed nearly simultaneously during impact events make this approach impractical for analyzing distributed failure due to impulsive loads.

Plasticity Based Models

A large body of knowledge has been developed around elastic-plastic models and their applications in continuum

mechanics. Chen and Saleeb [18] summarize these models with emphasis on applications to concrete, rock, and soils. Chen [19] provides further emphasis on plasticity based models for concrete. These references are particularly interesting because ceramics can be regarded in many respects as an artificial rock.

One of the earliest models of this class that is potentially applicable to ceramics is the Mohr-Coulomb model. This model states that the shear stress  $\tau$  at yield (or failure) is related to the normal stress  $\sigma$  by the relationship:

$$|\tau| = c - \sigma \tan(\phi) \quad (3-1)$$

where  $c$  is the cohesion and  $\phi$  the internal friction angle of the material. Equation 3-1 is the pair of straight lines that bound the circles from uniaxial tension and compression tests in a Mohr's circle construction as shown in Figure 5. The plane that these stresses act on is any plane whose normal lies in the plane of  $\sigma_1$  and  $\sigma_2$ . For any such plane, when  $\sigma$  and  $\tau$  satisfy equation 3-1, slip (or cleavage) will occur on that plane. The model may be represented as:

$$\frac{\sigma_1}{f'_t} - \frac{\sigma_3}{f'_c} = 1 \quad (3-2a)$$

where

$$f'_c = \frac{2c \cos \phi}{1 - \sin \phi} \quad (3-2b)$$

$$f'_t = \frac{2c \cos \phi}{1 + \sin \phi} \quad (3-2c)$$

The values  $f'_c$  and  $f'_t$  are the uniaxial compressive and tensile failure strengths, respectively.  $\sigma_1$  and  $\sigma_3$  are the maximum and minimum principal stresses, with the intermediate principal stress notably absent.

The Drucker-Prager criterion proposed in 1952 modifies the von Mises yield criterion from the form:

$$(J_2)^{1/2} = k \quad (3-3)$$

to the form:

$$(J_2)^{1/2} = k - \alpha I_1 \quad (3-4)$$

where  $J_2$  is the second invariant of the deviatoric stress tensor and  $I_1$  is the first invariant of the stress tensor. This is effectively a pressure dependent yield surface with a circular cross section in the  $\pi$  plane. Its similarity to the von Mises criterion, and lack of corners, makes it very easy to use in computational applications.

The Mohr-Coulomb model and the Drucker-Prager model are two-parameter models. Many more sophisticated models exist which take into account such factors as the effect of the

intermediate principal stress. Because of the limited data available for ceramic at high loading rates, only the simplest model forms are considered here.

Figure 5 illustrates the Mohr-Coulomb failure envelope for Coors AD85 alumina based on the manufacturer's static data. This plasticity model approach to the treatment of failure offers significant advantages in terms of computational simplicity.

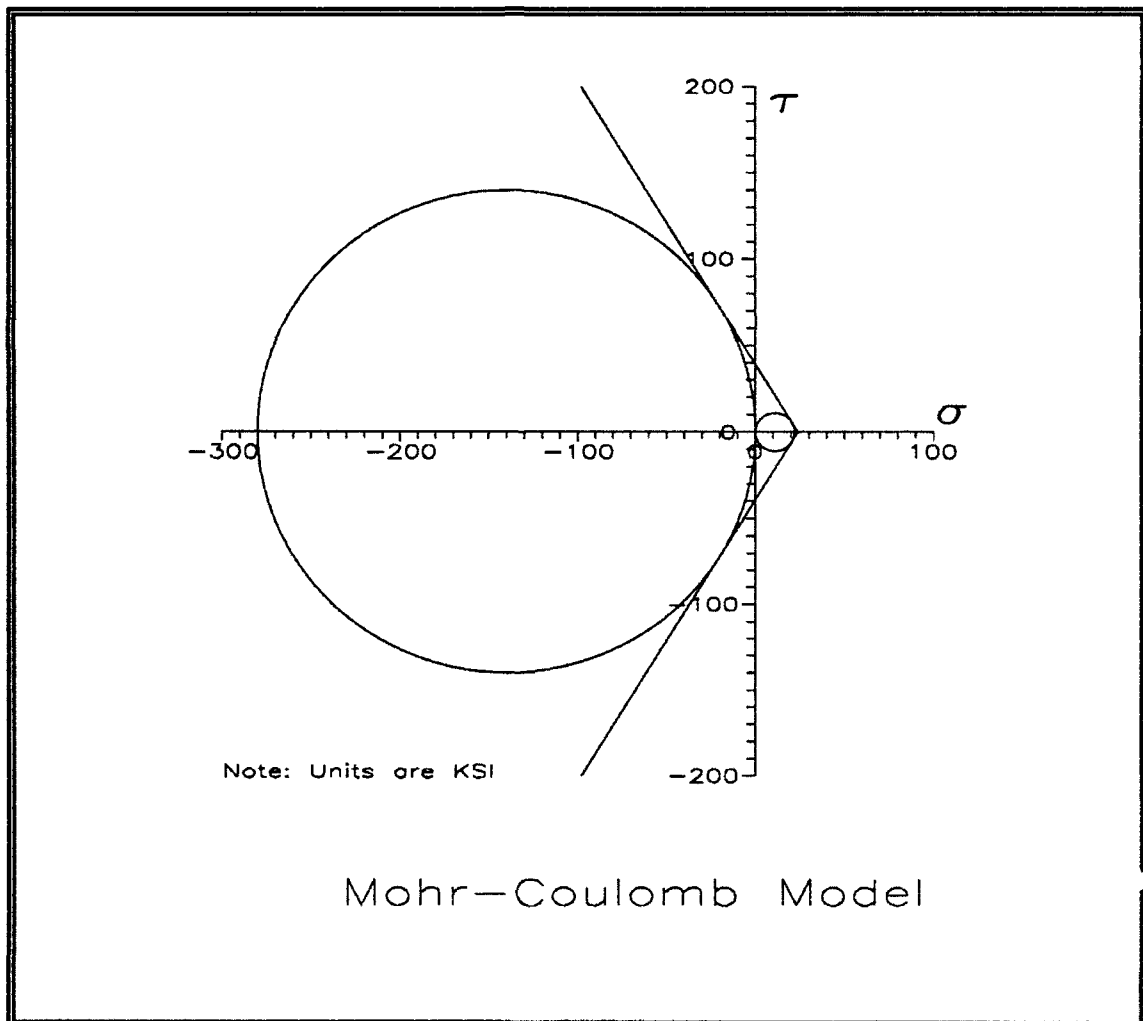


Figure 5. Mohr-Coulomb Model

### Nucleation and Growth Models

In contrast to methods that deal with individual cracks and follow those crack developments and growth (LEFM and EPFM), and in contrast to plasticity based models, an alternative approach is the cumulative damage class of failure model. Cumulative damage models are particularly well suited to problems where failure occurs by the simultaneous growth of several failure points. They are easily implemented in finite element models where damage may be expressed as an element variable, frequently providing a reduction in load-carrying capacity in the element, depending on the model. A prominent example is the Nucleation and Growth (NAG) model developed by Curran and associates at SRI, International.

Curran, Seaman, and Shockey [20] developed relatively complex NAG models that rely on an approach they describe as microstatistical fracture mechanics (MSFM). For ductile metals, they considered two primary failure mechanisms:

- (1) ductile hole growth in the form of spherical voids
- (2) adiabatic shear banding

For brittle materials, such as ceramics, they considered one failure mechanism:

- (1) brittle fracture in the form of penny shaped cracks (also considering compressive damage and "healing" before tensile failure)

An initial distribution of inherent flaws (inclusions, voids, crazed zones, pile-up of dislocations, etc) is taken as:

$$N_g(R) = N_0 \exp(-R/R_1) \quad (3-5)$$

where  $N_0$  is a material constant

$R_1$  is a material constant

$R$  is flaw size (radius)

$N_g$  is the number of flaws per unit volume with size greater than  $R$

One of the criticisms of the model is this assumed initial distribution of flaws. A much more desirable situation would provide for a more definitive description of the actual flaws in a given material based on directly observed mechanical measures. For example, for Coors AD85, this might consider the porosity of the material, a description of the pore sizes, and contaminant materials.

A localization threshold for inherent flaws is taken as:

$$F\left(\frac{\sigma_m}{\sigma_y}, \epsilon^p, \dot{\epsilon}^p, T, R\right) \geq 0 \quad (3-6)$$

where  $\sigma_m$  is mean stress

$\sigma_y$  is yield stress

$\epsilon^p$  is equivalent plastic strain

$\dot{\epsilon}^p$  is equivalent plastic strain rate

$T$  is temperature

$R$  is flaw size

A nucleation rate function is taken to be the sum of three terms, the first a thermal-rate-theory diffusion-driven nucleation term, the second a term due to mechanical debonding from plastic strain, and the third a term due to debonding of inclusions due to mean tensile stress.

Following nucleation, microscopic damage features such as voids or cracks grow under continued loading. Growth may occur due to several types of processes such as atomic diffusion, ductile plastic flow, brittle crack extension, or shear slipping and extension. Each may be expressed mathematically in very different forms. For ceramic, brittle crack growth would seem to be the most critical process, but SRI experiments indicated a viscous growth relation is more appropriate even for typically brittle ceramic materials. If the failure in alumina is due to flow of the glassy phase, which is one possible failure mode, this would seem to be particularly appropriate for alumina ceramic. Like the nucleation law, the growth law takes the form:

$$N_g(R) = N_0 \exp\left(\frac{R}{R_f}\right) \quad (3-7a)$$

where

$$R_f = R_i \exp\{T_1(\sigma - \sigma_{g0})\Delta t\} \quad (3-7b)$$

and  $N_g$  is the number of flaws per unit volume with size greater than  $R$

$N_0$  is a material constant

$R_f$  is the final flaw radius

$R_i$  is the initial flaw radius

$T_1$  is a material constant with units of inverse  
viscosity

$\sigma$  is stress

$\sigma_{g0}$  is a threshold stress for growth

$\Delta t$  is a time step

Figure 6 shows that the nucleation and growth processes combine to yield damage predictions as shown.

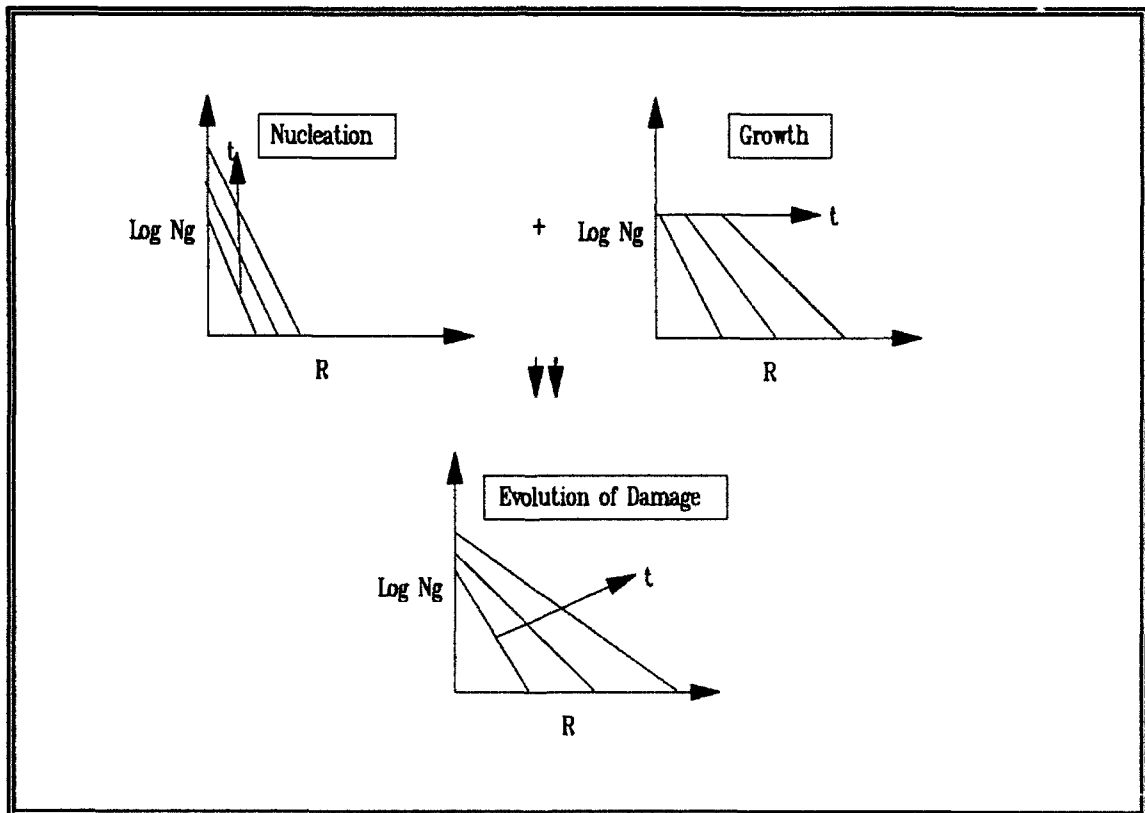


Figure 6. Crack Size vs. Load and Duration [21]

The final stage of this damage model treats the coalescence of cracks and voids, leading to a prediction of material separation and fragmentation. SRI assumed six to eight sided fragments, with a crack radius equal to the fragment radius and the number of fragments equal to one-third to one-fourth of the number of cracks. Their approach looks for numbers of fragments of a small number of discrete sizes, assuming largest fragments form first.

Improvements to the SRI NAG model seem desirable in the areas of describing the initial state of the material more appropriately and an improved treatment of the fragmentation process. For penetration of confined ceramic, it is important that both the compressive and tensile failure processes are included in nucleation, growth, and coalescence phases.

#### Fragmentation Models

The work of Grady [22,23,24] on the fragmentation of rocks has applicability to the final phase of breakup of ceramics. Grady performed high-strain-rate experiments on a number of different types of rocks and artificial rocks, observing that the number of fragments can be correlated to the rate of loading. He concluded that an equilibrium approach dealing with local energy and momentum balance can lead to the prediction of the fragment sizes in dynamic fracture.

This class of fragmentation model is principally directed

at the spall of brittle materials. In his original papers [22,23], Grady proposed balancing the kinetic energy of an expanding fluid material with the surface energy of fracture. By minimizing energy with respect to surface area, a predicted surface area per unit volume, and hence a fragment size, could be predicted. The key relationships and final result for a cubic fragment in a uniformly expanding field are given below.

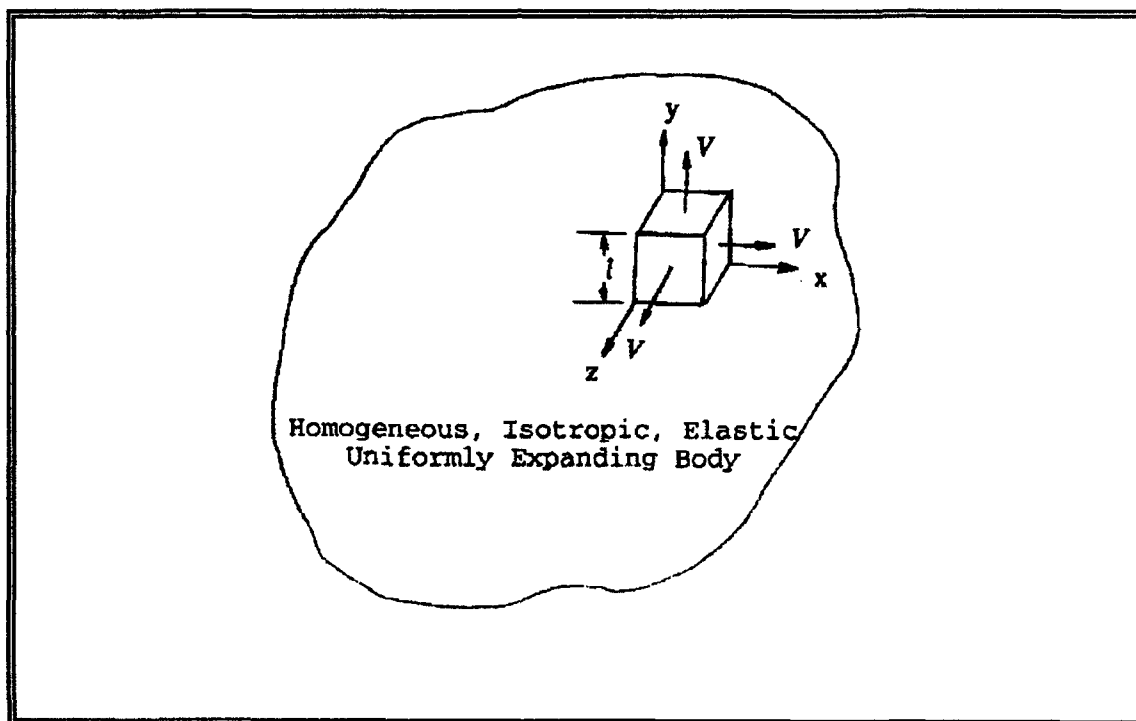


Figure 7. Fragmenting Body for Grady Fragmentation Model

As shown in Figure 7, within an expanding body a cube of length  $l$  on each side is considered with a local coordinate system aligned with the faces. A uniform density  $\rho$  is assumed within the cube. Positive and equal outward

velocities  $V = V_x = V_y = V_z$  are assumed for a uniformly expanding material (conceptually similar to inward velocities for a compressive field.) The kinetic energy is given as:

$$KE = 1/2 \int_V (\dot{x}^2 + \dot{y}^2 + \dot{z}^2) \rho dx dy dz \quad (3-8a)$$

where

$$\dot{x} = V_x \left( \frac{2x}{l} \right) \quad \text{for} \quad -\frac{l}{2} \leq x \leq \frac{l}{2} \quad (3-8b)$$

$$\dot{y} = V_y \left( \frac{2y}{l} \right) \quad \text{for} \quad -\frac{l}{2} \leq y \leq \frac{l}{2} \quad (3-8c)$$

$$\dot{z} = V_z \left( \frac{2z}{l} \right) \quad \text{for} \quad -\frac{l}{2} \leq z \leq \frac{l}{2} \quad (3-8d)$$

Performing the integration and considering symmetry gives

$$KE = \frac{\rho l^3 V^2}{2} \quad (3-9)$$

Conservation of mass requires that

$$\dot{\rho} + \rho \left( \frac{\partial V_x}{\partial x} + \frac{\partial V_y}{\partial y} + \frac{\partial V_z}{\partial z} \right) = 0 \quad (3-10)$$

so that

$$\dot{\rho} + \rho \left( \frac{2V}{l} + \frac{2V}{l} + \frac{2V}{l} \right) = 0 \quad (3-11)$$

or

$$V = -\frac{\dot{\rho}}{6\rho} l \quad (3-12)$$

Substituting for  $V$  in the kinetic energy expression above gives

$$KE = \frac{l^5 \dot{\rho}^2}{72\rho} \quad (3-13)$$

The ratio of surface area to volume for a cube is

$$A = \frac{6l^2}{l^3} = \frac{6}{l} \quad (3-14)$$

and expressing the kinetic energy density in terms of  $A$  gives

$$KE \text{ density} = \frac{\dot{\rho}^2}{2A^2\rho} \quad (3-15)$$

Surface energy density (surface energy of cracks per unit volume of material) for fracture is given as

$$\Gamma = \gamma A \quad (3-16)$$

where  $\gamma$  is the surface energy per unit area and  $A$  is the surface area per unit volume described in equation 3-14. This relation is valid where the determination of the surface energy per unit area is obtained by considering the areas of both surfaces in a forming crack which is twice the area of the crack length times the crack width. This gives total energy density as a function of the ratio of surface area to volume as:

$$E(A) = \frac{\dot{\rho}^2}{2A^2\rho} + \gamma A \quad (3-17)$$

which can be minimized with respect to  $A$  to give

$$A = \left( \frac{\dot{p}}{\gamma p} \right)^{\frac{1}{3}} \quad (3-18)$$

The relation between surface energy of fracture and the static fracture toughness,  $K_{Ic}$ , for tensile failure, is

$$\gamma = \frac{K_{Ic}^2}{2\rho c_0^2} \quad (3-19)$$

where  $c_0$  is the sound speed. Combining equation 3-18, the relation between  $A$  and  $l$  given in equation 3-14, and equation 3-19 yields the edge length of a predicted cubic fragment:

$$l = \left( \frac{\sqrt{108} K_{Ic}}{\dot{p} c_0} \right)^{\frac{2}{3}} \quad (3-20)$$

This is a form suitable for implementation in a computational submodel.

In a later paper [24], Grady notes the relative insignificance of kinetic energy when compared to the elastic energy of the fragmenting body, and he presents a similar derivation considering only elastic energy. The elastic energy density in a body,  $U$ , can be described by:

$$\text{Elastic Energy Density} = U = \frac{1}{2} \frac{P^2}{\rho c_0^2} \quad (3-21)$$

where  $c_0$  is the bulk wave speed,  $\rho c_0^2$  is the bulk modulus, and  $P$  is the mean pressure. The time,  $t$ , that a crack requires to grow the distance  $l$  is given by:

$$t \geq \frac{l}{2c_0} \quad (3-22)$$

by physical arguments based on the bulk wave speed as the maximum rate of crack growth and considering a crack growing from an initiation point in opposing directions such that the crack length  $l$  is

$$l \leq 2c_0 t \quad (3-23)$$

The time dependent mean pressure,  $P$ , can be described as:

$$P = \rho c_0^2 \dot{\epsilon} t \quad (3-24)$$

Combining the above with the definition of  $A$  given in equation 3-14 yields

$$U = \frac{36\rho\dot{\epsilon}^2}{8A^2}$$

Following a similar procedure to that used on kinetic energy, a fragment size is predicted as:

$$l = \left( \frac{\sqrt{12} K_{Ic}}{\rho \dot{\epsilon} c_0} \right)^{\frac{2}{3}} \quad (3-26)$$

This type of fragmentation model was developed for spall failure in tension where failure clearly results in loss of surface tractions and hence release of elastic energy as well as a loss of kinetic energy with respect to a fragment mass center. The extension to compressive failure requires assumptions about the extent of release of elastic energy, but otherwise is conceptually the same. The use of  $K_{Ic}$

involves a tensile fracture toughness applied to a compressive loading field, with its use justified by assuming that under macroscopically compressive loading, local tensile stresses around pores are responsible for fracture. This concept is discussed below.

#### Compressive Fracture Mechanisms

Figure 8 illustrates the observed crack evolution in brittle materials. A net compressive stress field causes the largest material irregularities to begin to form crack extensions at the points of largest stress concentration. These cracks turn to align with the axis of application of the compressive load. As loading increased, smaller irregularities begin initiating crack growth. Under dynamic loading, multiple cracks grow and interact to finally result in a fragmented material.

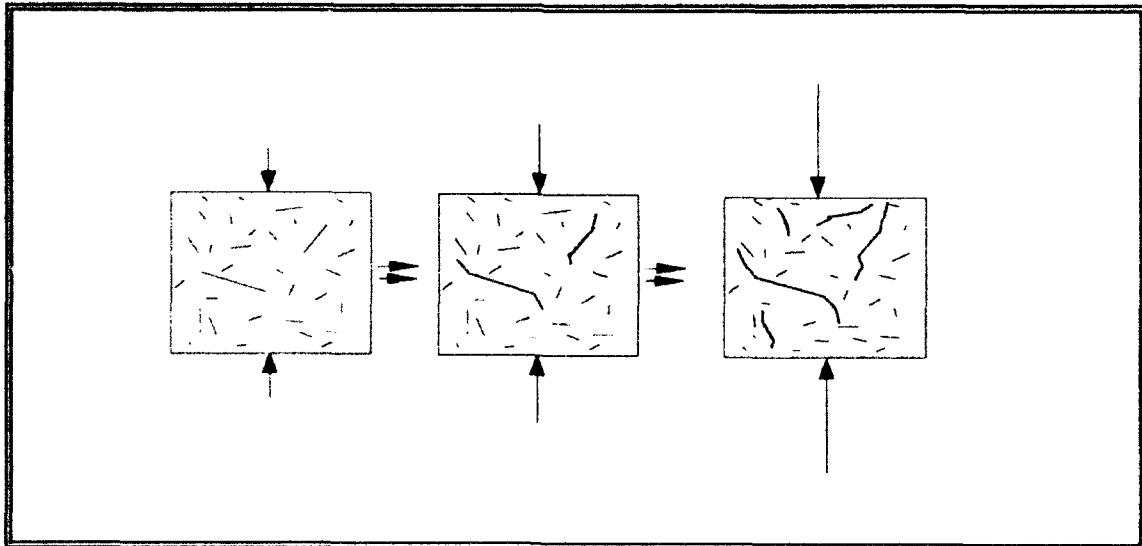


Figure 8. Development of Cracks Under Compressive Loading

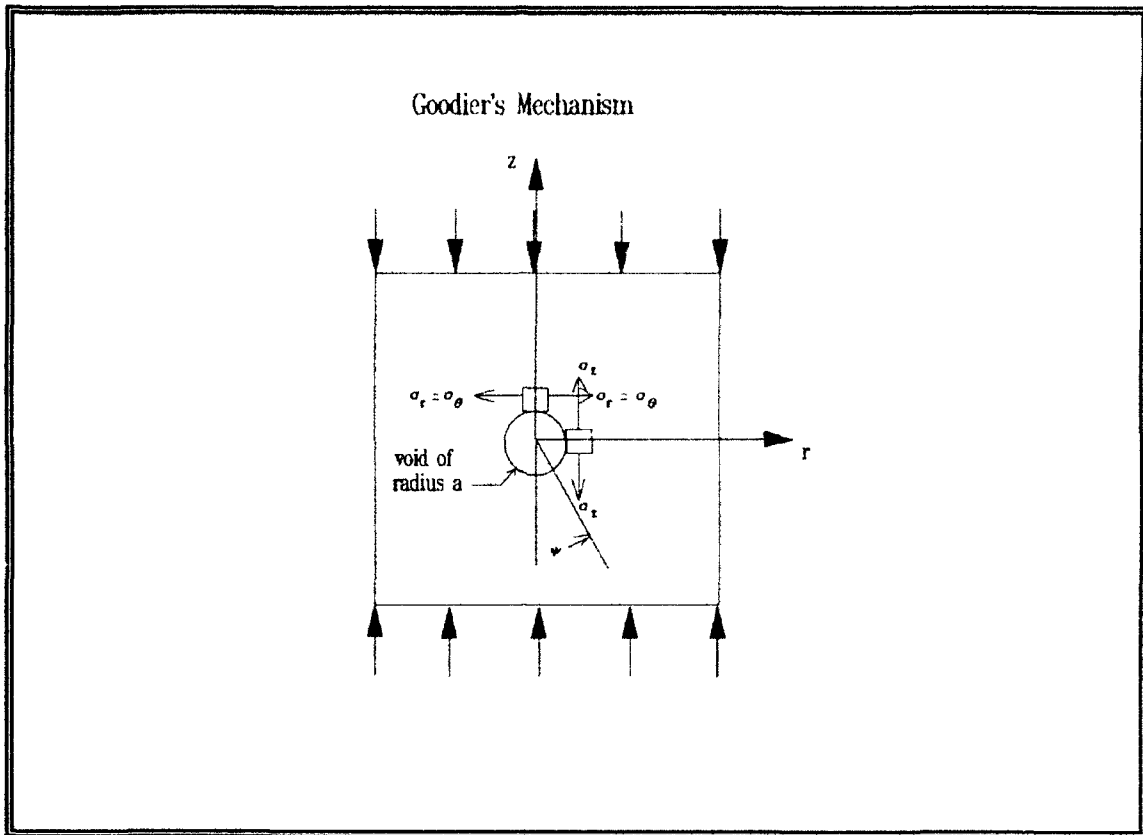


Figure 9. Goodier's Mechanism

Figure 9 is provided to describe how Goodier's mechanism offers one possible explanation of how a macroscopic compressive field can result in tensile failure at points of stress concentration. Details on Goodier's elastic solution around a spherical void are provided by Timoshenko and Goodier [25]. Their solution is,

for  $\psi = \pi/2$ ,

$$\sigma_z = \left( 1 + \frac{4-5\nu}{2(7-5\nu)} \left( \frac{a^3}{r^3} \right) + \frac{9}{2(7-5\nu)} \left( \frac{a^5}{r^5} \right) \right) \sigma \quad (3-27)$$

and, for  $\psi=0$  or  $\psi=\pi$ ,

$$\sigma_{\theta} = \sigma_r = -\left(\frac{3+15\nu}{2(7-5\nu)}\right)\sigma \quad (3-28)$$

Based on the equations above, for a ceramic with a Poisson's ratio of  $\nu=0.22$ , a peak compressive stress of approximately twice the applied stress occurs at a radius  $r=a$ , in the direction of the applied load, where  $\psi=\pi/2$ . Also at a radius  $r=a$ , but for  $\psi=0$ , a tensile stress 0.53 times the applied compressive stress  $\sigma$  occurs at the top of the spherical void, transverse to the applied stress. For an alumina with a static tensile strength of 22,000 psi versus a compressive strength of 280,000 psi, any net compressive field would cause localized tensile stresses that would exceed the tensile capacity of the material before the compressive limits were reached, resulting in a crack opening along the axis of loading. This is in good agreement with the observed behavior of most brittle materials with a high ratio of compressive to tensile strengths.

Nemat-Nasser and Horii [26,27,28] differentiate between the shear failure (faulting) and the axial splitting that occurs in brittle material under compression. They observe and derive mathematical relationships that explain how as confining pressure increases, the development of unstable

crack growth from pre-existing flaws decreases, faulting decreases, and consequently the contribution of deformation due to microcracking decreases and plastic flow increases. With lateral compression, crack growth initiates at pre-existing flaws, but remains stable and stops at a finite crack length. Without lateral compression, crack growth is unstable as tension cracks initiate at pre-existing flaws and grow along the axis of compression. Their conclusions are supported by elaborate solutions to the elastic boundary value problem around a single pre-existing flaw under far field compressive stress loading.

Other mechanisms have been proposed based on grain boundary failures due, for example, to localized thermal instabilities in the glass phase silica bonding aluminum oxide grains. Lankford [29] identified thermally activated processes as operative below strain rates of 100 inches per inch per second and inertial processes predominating at higher strain rates. He reported deformation twinning as a critical mechanism to compressive failure [30]. These other proposed mechanisms are suggested specifically for applications where dynamic loading occurs. The mechanisms proposed by Goodier and Nemat-Nasser are based on static elastic solutions, and therefore do not consider inertial effects of dynamic loading and the effects of adiabatic heating and thermal instabilities. Work continues on detailing the mechanisms of fracture damage in ceramics,

with emphasis on extending the understanding to dynamic conditions. For example, Vekinis, Ashby, and Beaumont [31] have examined model materials representing ceramics using static and dynamic in-situ SEM observations of the fracture process. They conclude that, "the collapse of a pore in a brittle material occurs by microfracturing on or near the pore surface and proceeds by the generation of fragments in the immediate vicinity of the pore" [11, p. 77].

#### Ceramic Impact and Fracture

Certain ceramics, such as Coors AD85 alumina, are well characterized in terms of material strength and failure properties under static loading conditions. Table 2 provides manufacturers data [32] on the properties of AD85.

Table 2. AD85 Material Properties

Material Property for AD85	Value	Units
Density	0.123	lbm/in <sup>3</sup>
Tensile Strength	22	ksi
Compressive Strength	280	ksi
Shear Modulus	14,000	ksi
Modulus of Elasticity	32,000	ksi
Longitudinal Sound Speed	27,000	ft/sec
Poisson Ratio	0.22	
Crystal Size Range	79-473	microinch
Average Crystal Size	236	microinch

These data, along with extensive other information for steady state load response of ceramics, allow accurate analysis of ceramic materials undergoing relatively stable loading.

In contrast, the response of a ceramic material to a penetrating body can be quite complex depending on the ceramic material properties, penetrator material properties, target geometry and complexity (thickness to penetrator diameter ratio and target laminations), and penetrator geometry (length to diameter ratio and nose shape).

Much notable progress has been made in understanding the failure of ceramics during the last ten years, and even more rapid advancements are likely due to extensive current interest.

Anderson and Bodner [33] have recently presented a review paper that extends beyond the treatment of simple metallic targets and discusses the dynamic response of ceramics noting its current importance to ballistic modeling. They point out the need for constitutive and fracture model development and implementation in hydrocodes and suggest using a Mohr-Coulomb modeling approach.

The dynamic behavior of certain armor types of ceramics has been investigated in both the as-manufactured state of the ceramic, and as post-fractured, granular ceramic material. Plate impact tests have been used by a number of researchers including Gust and Royce [34], Munson and Lawrence [35], and Rosenberg [36]. This experimental method has been used to develop equation of state and constitutive model data as well as to evaluate dynamic deformation mechanisms and fracture processes. Rosenberg observed an

effect under certain moderate to high loading rate conditions that he attributed to dilatancy in alumina. The validity of this explanation and its importance to the penetration process require further investigation. Arrowood and Lankford [37] investigated the dynamic response of particulated alumina and beryllium oxide using compressive pressurized servohydraulic tests and compressive split Hopkinson bar techniques. They established some of the information necessary for the development of constitutive models for a single particle size of post fractured ceramic.

Lawn [38] published an article describing the current status of linear continuum fracture mechanics as applied to ceramics. His viewpoint is representative of the majority of work currently underway in the materials science research community, emphasizing the importance of understanding of the micromechanisms of failure in order to permit the development of tougher ceramic materials, rather than to permit the development of computational models.

Evans [39] performed extensive research on the fracture mechanisms of ceramics under a broad range of loading conditions. Most of his work is at lower rates of loading than are of interest here, with emphasis on classical LEFM and EPFM approaches.

Yaziv [40] studied the one-dimensional fracture of ceramics in plate impact tests, providing insight into the nature of fracture and providing useful new experimental

techniques . He developed double flier plate impact tests utilizing recovery methods capable of successfully catching spall specimens made of ceramics. His work specifically addresses the time required to fail the ceramic as suggested by previous work by Wilkens [41, 42].

Brandon [43], whose recent research has emphasized ceramic failure, provides a very complete review of those aspects of fracture pertinent to impact loading. He discusses three main damage regimes based on the ratio of the projectile kinetic energy density to the failure strength of the target. This method of categorizing penetration is similar to the three velocity ranges discussed earlier, but embodies penetrator mass characteristics and target strength characteristics as well. At low velocities, he suggests that fracture occurring by crack propagation can be described by linear elastic fracture mechanics. For dynamic problems, however, the treatment of crack branching is essential and the problem becomes very complex. At higher velocities, as the projectile velocity exceeds the sonic velocity of the materials, wave propagation effects predominate and rapidly varying loading conditions in each volume element seriously complicate the processes. Strain rate effects and inertial effects play prominent roles. Finally, at hypervelocities, inertial effects dominate along with extremely high temperature and high pressure phase changes. Brandon has

performed plate impact experiments with alumina that suggest that spalling is a cumulative damage process affected by the alumina phase and its grain size, the minor glassy phase and its volume fraction, and the distribution of pores and the pore sizes. The dominant fracture mode observed by Brandon was shear and viscous flow of the glassy phase rather than cleavage of the alumina grains, based on post mortem evaluation of fracture surfaces [44].

Both Yaziv and Brandon discuss three mechanisms for damage introduced into ceramics during high velocity impact:

- (1) Microcracking at grain boundaries or by cleavage
- (2) Dislocation multiplication and glide
- (3) Localized adiabatic heating

Each of these mechanisms has been observed and reported.

Sternberg [45] has determined that a relationship exists between penetration resistance and fracture toughness. He studied the relationship between hardness measurements and ballistic tests measuring residual penetration, observing that the ratio of measured target strength to hardness increases with fracture toughness.

Yaziv et al. [46] considered various target thicknesses in flyer plate experiments. They concluded that a pressure dependence of yield strength exists in the form

$$Y = 280,000 + 0.54P \quad (3-29)$$

where  $Y$  is yield strength,  $P$  is mean pressure, and units are  $\text{lb}/\text{in}^2$ .

Yeshurun et al. [47] observed microcracks in recovered alumina flyer plate experiments at stress levels below the Hugoniot Elastic Limit (HEL.)

Cagnoux and Longy [48,49] used flyer plate experiments to investigate microcracking in alumina and strain rate effects. They report no microcracking at up to twice the HEL. They also conclude that strain rate effects reported in Hopkinson Bar experiments are a result of the loading conditions, and find no strain rate dependence in plate impact tests, observing that the high confining pressures cause grain plasticity which determines yielding.

Bless [50] provided a summary paper discussing the properties of ceramics that relate to impact behavior, experimental techniques, and the ambiguities that still exist in the data. He concluded that the shear strength of alumina exceeds the static compressive strength at high confining pressures, strength increases observed in plate impact tests are probably due to pressure effects, some strain rate effect is indicated at ultra high strain rates, and the roles of grain plasticity versus microfracture are unclear.

#### Ceramic Fracture Models

Rajendran and Cook [51] conducted a comprehensive review of ceramic fracture models and found that the number of models that had been applied to ceramics was quite small. These models were adapted primarily from geotechnical

material failure models. The number of models developed and applied to ceramic fracture under impulsive loading was even smaller.

Rajendran, Kroupa, Dietsberger, and Grove [52,53,54] explored ceramic failure models employing relatively detailed micromechanical modeling. Their models employ constants with physical meaning that are determined through computational comparisons with plate impact experiments. They demonstrated that their models accurately describe the failure signatures obtained in plate impact experiments. Their recent modeling has emphasized the improved treatment of the compressive failure process, and is an extension of the model described in the following paragraph.

Furlong and Alme [55] implemented an early version of the model proposed by Rajendran et al. They used a tensile failure model based on an extension to the Grady-Kipp fragmentation model [56] as proposed by Taylor, Chen, and Kuszmaul [57]. For compressive damage, they used a plasticity approach assuming a compressive time rate of damage proportional to the rate of inelastic work. After experiencing some early difficulties with solution stability, they reported, "the model to produce the desired compressive effect without any compromise of the tensile model or any numerical instabilities" [55,p. 17].

Johnson and Addessio [58] developed a comprehensive brittle-ductile failure model that is applicable to

materials ranging from ceramics to metals. They employed a micromechanical approach similar to those discussed above, but place greater emphasis on the widest possible range of applicability.

Soon-Kil Chung [59] addressed the fracture characteristics of ceramic armor materials, noting the importance of kinked crack growth and its relation to toughness of a ceramic armor as observed in penetration experiments. He proposed defining local compressive fracture toughness,  $K_c^c$  to be

$$K_c^c = 2K_{Ic} / (\sqrt{1 + \mu^2} - \mu) \quad (3-30)$$

where

$K_{Ic}$  is mode 1 fracture toughness

$\mu$  is the friction coefficient between crack faces

This analysis is helpful in describing a mechanism for local compressive microfracture, and explains the reason that some ceramics exhibit tougher behavior than otherwise would be expected. The model is most useful in evaluating the relative merits of prospective armor materials as opposed to application in computational models which was not addressed by the author.

Louro [60] studied the compressive failure of alumina and demonstrated that crack surface per unit volume can be related to compressive stress pulse magnitude and duration, supporting a nucleation and growth approach. He presented a

fracture-mechanics-based nucleation and growth model for compressive loading conditions of impact loaded alumina ceramic.

Johnson and Holmquist [61] presented a computational constitutive/failure model for brittle materials subjected to large strains, high strain rates, and high pressures. The model was developed specifically for application in hydrocodes, and is analogous to the Johnson-Cook models for metals [62,63] employing empirical fits in a damage-evolution model. The simplicity and compatibility with the computational framework of continuum mechanics codes are noted as essential elements of the model [64]. The model's implementation is computationally consistent with typical treatment of material strength and failure in these codes, based on a Von Mises equivalent stress criterion and a Prandtl-Reuss flow rule. The model is essentially a Drucker-Prager failure surface with a unique treatment of energy transition during fracture. The released elastic energy density is used in an additional equation of state term to provide a pressure increase in a confined, failing ceramic. This provides a direct dilatational response that can be quantified by energy conservation. A second Drucker-Prager surface that does not allow strength for net tensile pressures defines yield for the post fractured material.

Steinberg [65] proposed a model that avoids

micromechanical complexities and represents the behavior of ceramic in a manner similar to his past treatment of dynamic metals constitutive modeling. He describes stress as a function of strain, strain rate, pressure, and temperature, treating compressive fracture in these macroscopic variables. He demonstrated good agreement with spall recovery signals in plate impact tests using a one-dimensional hydrocode.

As the review above indicates, a number of ceramic fracture model researchers are approaching the problem of the impulsive loading and failure of ceramics in different ways. All of the models continue to be in development. Only the Johnson-Holmquist model is currently in a production hydrocode.

CHAPTER 4  
MATERIAL DATA

Mechanical Properties of Alumina

Coors AD85 alumina is a hot sintered composite material composed of approximately 85 percent by weight aluminum oxide grains bonded together in a silica glass matrix. The range of grain sizes is from 79 to 473 microinches with an average size of 236 microinches. The material is approximately 85% of theoretical density for aluminum oxide, with a density of 0.123 pounds mass per cubic inch. Porosity is approximately 11%, consisting of irregular shaped pores ranging mostly from 2 to 30 microns in diameter. Trace impurities from several other elements are present. Table 2 in Chapter 3 summarized the manufacturer's material data, and this chapter discusses measurements made on the ceramics used in this research. In general, the availability of material data for applications in ceramic fracture models is summarized in Table 3. Tests are described in Chapter 5 that were designed to clarify strain rate effects, dynamic strength, microcracking versus loading history, and macrocracking versus loading history. Chapter 6 provides more details on the observed properties of AD-85 after testing.

Table 3. Availability of Material Data

Available Data		
Pressure Effects	Very Limited	
Strain Rate Effects	Conflicting	*
Temperature Effects	Extensive	
Static Strength	Extensive	
Dynamic Strength	Limited	*
Microcracking vs Loading History	Nonexistent	*
Macrocracking vs Loading History	Limited	*

\* Data sought in test program

#### Micrographic Study of Undamaged Ceramic

Figures 10, 11, and 12 show typical voids in the untested specimens after machining from the stock plate. These photomicrographs are provided for visual comparison to similar photomicrographs taken after various loading conditions were applied as described in the Chapter 5. In all cases, specimens were prepared by careful sectioning with a diamond wafer saw, rough grinding with wet aluminum oxide polishing disks, rough polishing with 30 micron diamond paste, and final polishing with 1 micron diamond paste. It should be noted that prior to testing, a small degree of damage was observed in the material as a result of either manufacturing processes or the specimen preparation. For example, the twinning and dislocations shown in the Transmission Electron Microscope (TEM) photographs at

magnifications of 77,000 times in Figure 11 demonstrate the sort of imperfections that were pre-existing in the test specimens. Figure 10 shows a typical pore structure at a magnification of 5,000 times on a Scanning Electron Microscope (SEM), illustrating an example of pore size relative to grain size, and a typical pore geometry and interior surface structure. Imperfections were not observed with an optical microscope or the SEM as shown in Figure 12. Magnifications in Figure 12 are 20 times and 120 times for the first two photographs from an optical microscope, and 1000 times and 2500 times for the second two photographs, which were taken with the SEM.

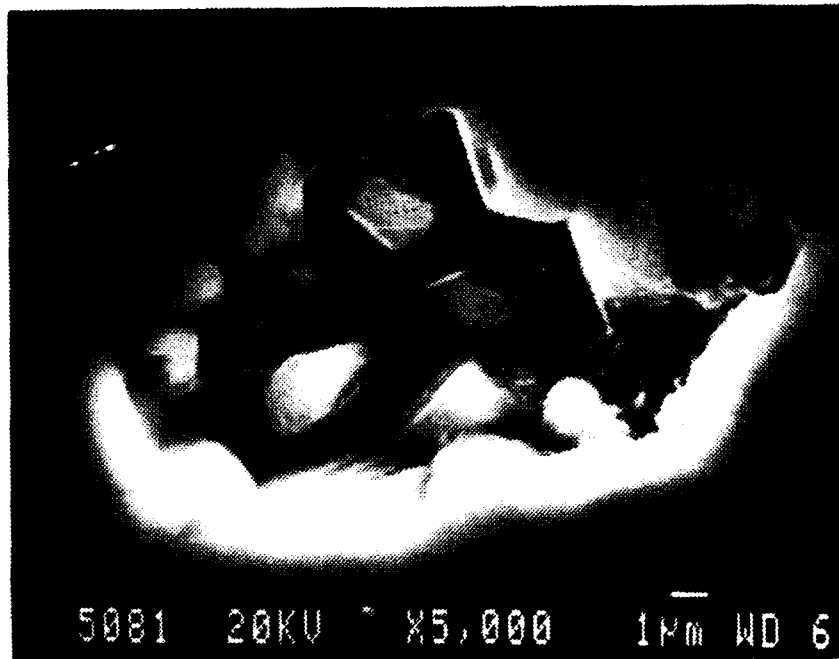
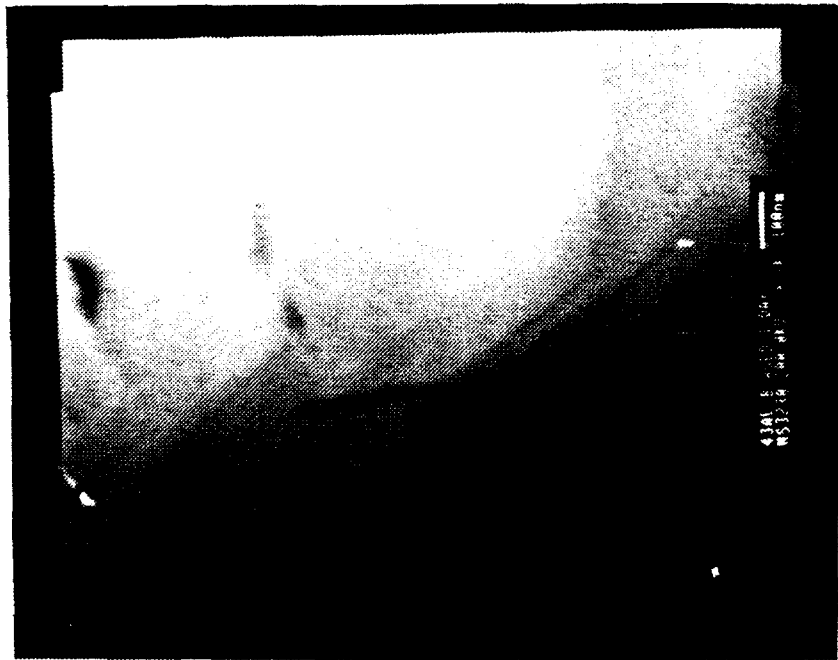


Figure 10. SEM Photomicrograph of Typical Void Structure



(a)



(b)

Figure 11. TEM Photomicrographs of Baseline Materials  
(a) Twinning in alumina grains  
(b) Dislocation in alumina grains

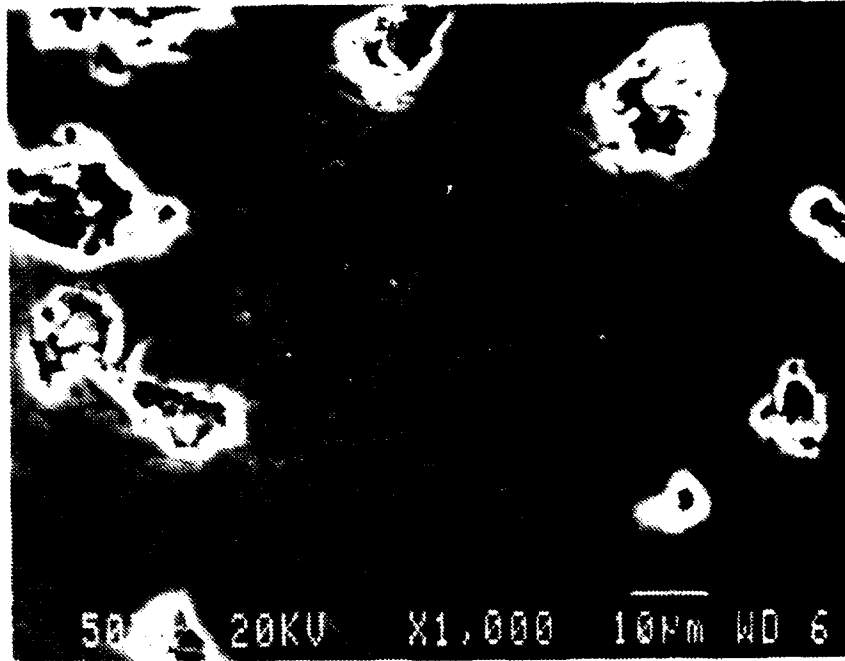


20X

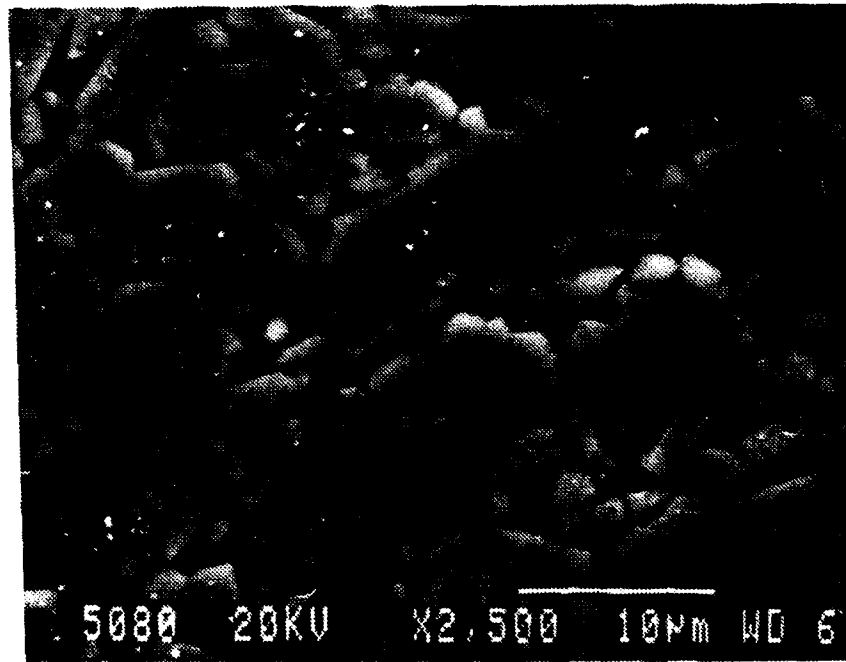


120X

Figure 12. Optical and SEM Photomicrographs  
Baseline Material (20X and 120X)



1,000X



2,500X

Figure 12. SEM Photomicrographs Baseline Material (1000X and 2500X) (Concluded)

## CHAPTER 5 EXPERIMENTS

### Experimental Program

This chapter documents the experimental program, which consisted of 13 compressive servohydraulic tests, 20 compressive Hopkinson bar tests, 13 plate impact tests, 22 rod-on-rod tests, and 9 penetration experiments. The first four types of tests provided a basis for the development of a ceramic fracture model, and the penetration experiments were used for model validation. This chapter deals primarily with the test configurations and provides some discussion of the results. The analysis of the results with respect to micrographic studies of the recovered material is discussed in Chapter 6.

### Instron Tests

Table 4 summarizes the results of 13 servohydraulic compressive tests performed to determine the failure stress of AD85 at two low strain rates. These tests also were stopped in some cases just below the expected failure stress to recover specimens and look for microscopic damage.

Table 4. Servohydraulic Compressive Tests

Test No	Strain Rate (1/sec)	Failure Stress (KSI)	Peak Stress (KSI)	Objectives
1	.0009	305		Failure Stress
2	.0009	309		Failure Stress
3	.0009	338		Failure Stress
4	.0009	307		Failure Stress
5	0.9	343		Failure Stress
6	0.9	336		Failure Stress
7	.0009		334	Damage
8	.0009	276		Failure Stress
9	.0009	311		Failure Stress
10	.0009		290	Damage
11	.0009		283	Damage
12	.0009		304	Damage
13	.0009	255		Failure Stress

#### Hopkinson Bar Tests

Figure 13 illustrates the Wright Laboratory Armament Directorate Hopkinson bar and Figure 14 illustrates the miniature compressive specimens that were used in this research [66]. The miniature compressive specimens were 1/8 inch in diameter and 3/16 inches long, and were surrounded by a piece of shrink fit Teflon tubing typically used for electrical insulation. The Teflon tubing allowed for recovery of the pulverized ceramic.

The specimens were placed in a collar that allowed approximately 8 percent strain in the specimen before absorbing the load and protecting the fragmented specimen from further damage. Figure 15 shows a sketch of the

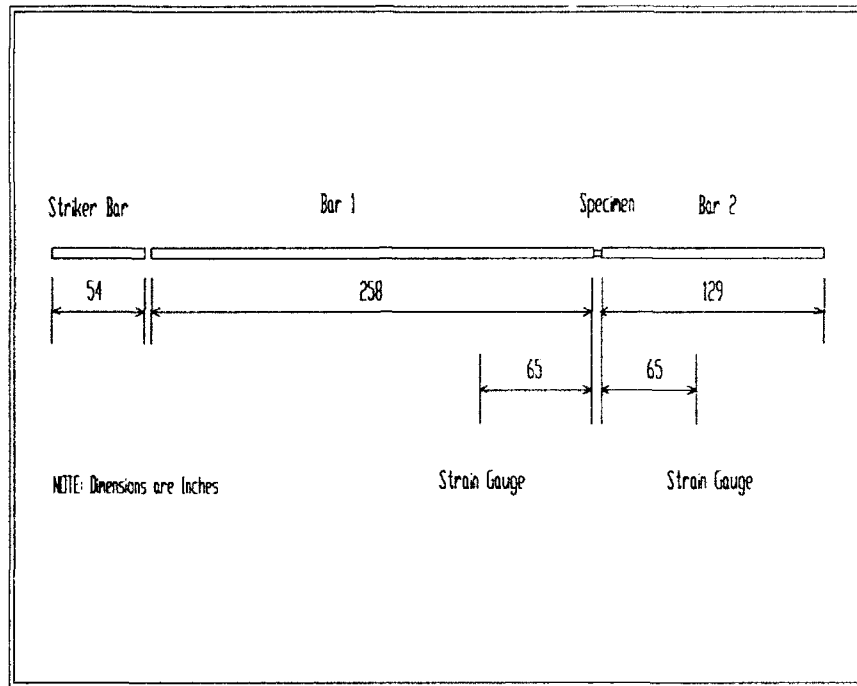


Figure 13. Split Hopkinson Pressure Bar Apparatus

collar and the protective alumina disks. The ratio of the bar diameter to the specimen diameter was 5:1, providing a stress multiplication of 25:1 from the bars to the specimen. Coors AD99 disks (alumina at 99% theoretical density with strength greater than AD85) were used to protect the ends of the bars from indentation by the AD85 specimens. The velocity of the striker bar was varied to achieve the highest strain rate possible in the system, a high strain rate at stresses near and below the failure strength, and to well beyond failure strength.

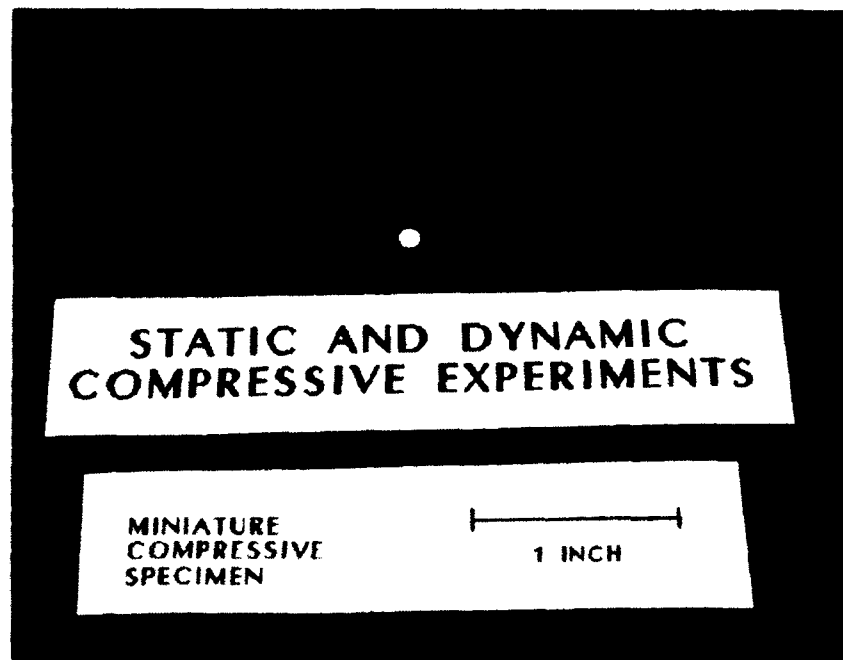


Figure 14. Miniature Compressive Test Specimen

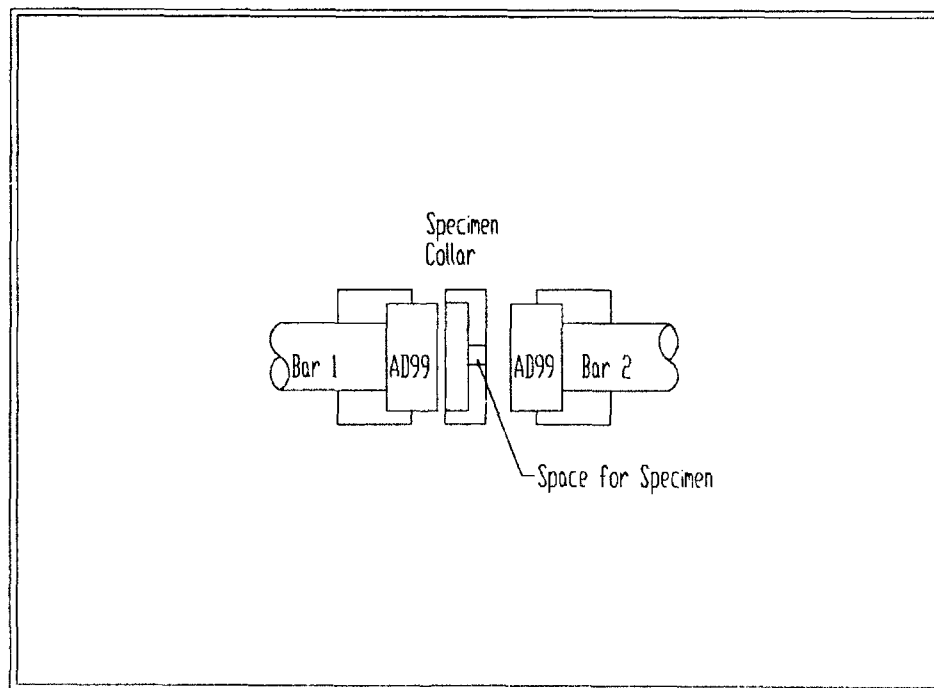


Figure 15. Fixture for Hopkinson Bar

Table 5 summarizes the results of 20 tests performed with the Hopkinson bar to obtain the compressive failure strength of AD85 at high strain rates. Failure strengths averaged 461,000 psi and 414,000 psi at 800 in/in/sec and 600 in/in/sec respectively.

Typical measurements from the Hopkinson Bar reduced to show stress levels as a function of time in both the input (incident) bar and the output (transmitter) bar are shown in Figures 16 and 17 respectively. The results shown are for Hopkinson Bar test number 19, where failure of the alumina was achieved. Of particular note is the immediate loss of ability to support load on failure, followed by a period of a lower level of supported stress, and finally a period where the load is supported by the metallic collar of the system. A more detailed look at the transmitted stress is shown in Figure 18. Figure 19 provides a similar look at the transmitted stress in test 18, where failure was achieved but in this case the ceramic appeared to support initially the full stress pulse applied in the system, followed by an apparent burst of load (from either the system or the process of failing in the ceramic.) A stage of reduced load support then follows, similar to that in Figure 18, before the collar supports the load during the final phase of the load pulse.

Table 5. Hopkinson Bar Compressive Tests

Test No	Drawback (inches)	Strain Rate (1/sec)	Failure Stress (KSI)	Peak Stress (KSI)	Objectives
1	5	800	422		Failure Stress
2	5	800	439		Failure Stress
3	5	800	431		Failure Stress
4	5	800	530		Failure Stress
5	5	800	483		Failure Stress
6	4	600	415		Failure Stress
7	4	600	409		Failure Stress
8	4	600	415		Failure Stress
9	4	600	418		Failure Stress
10	3.25			350	Damage
11	2.75			290	Damage
12	2.75			290	Damage
13	2.75			290	Damage
14	3.00			317	Damage
15	3.25			351	Damage
16	3.50			384	Damage
17	3.12			343	Damage
18	3.25			360	Damage
19	3.25			361	Damage
20	3.12			343	Damage

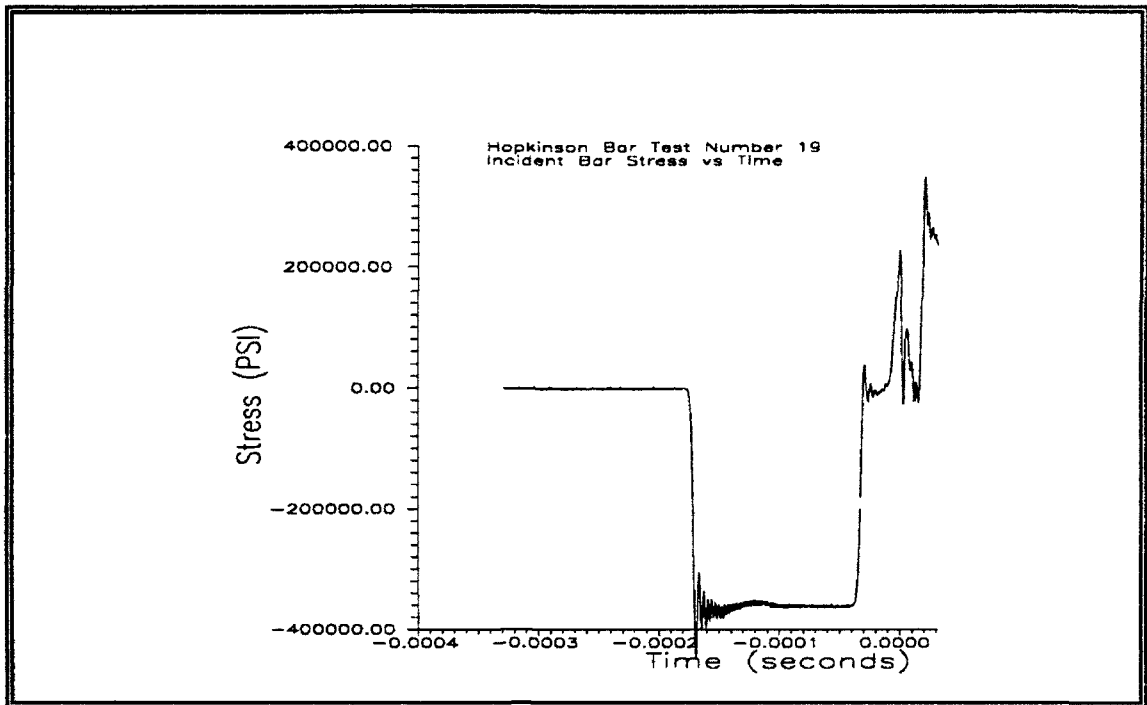


Figure 16. Hopkinson Bar Test 19 Incident Stress

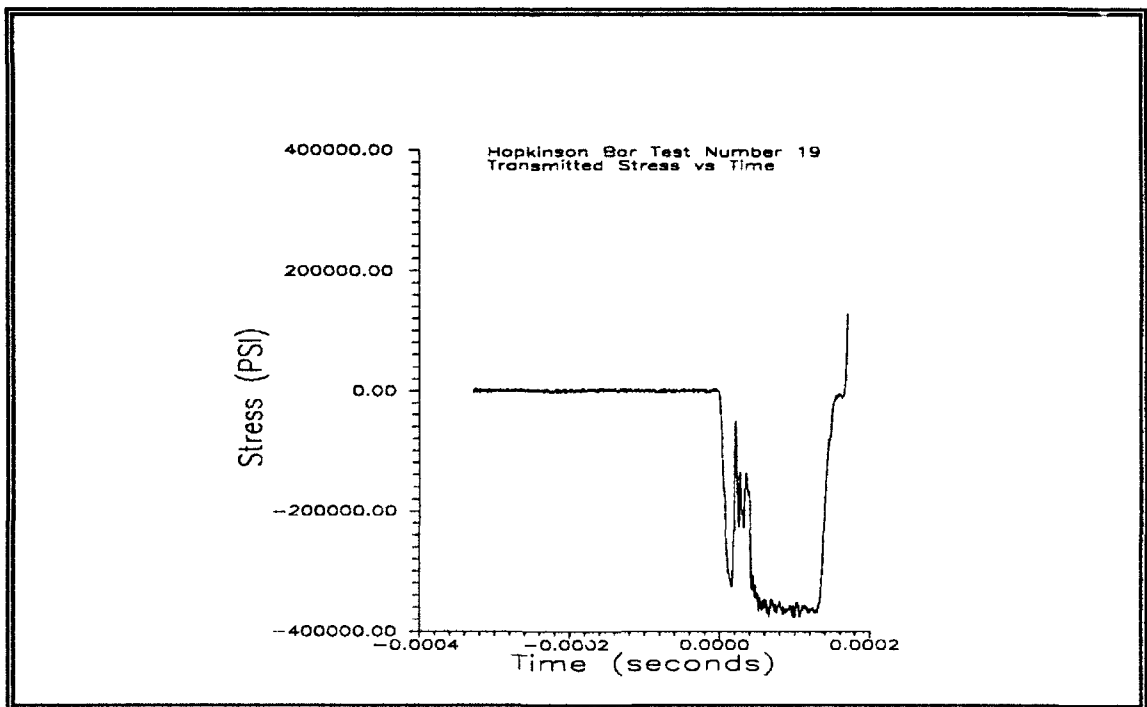


Figure 17. Hopkinson Bar Test 19 Transmitted Stress

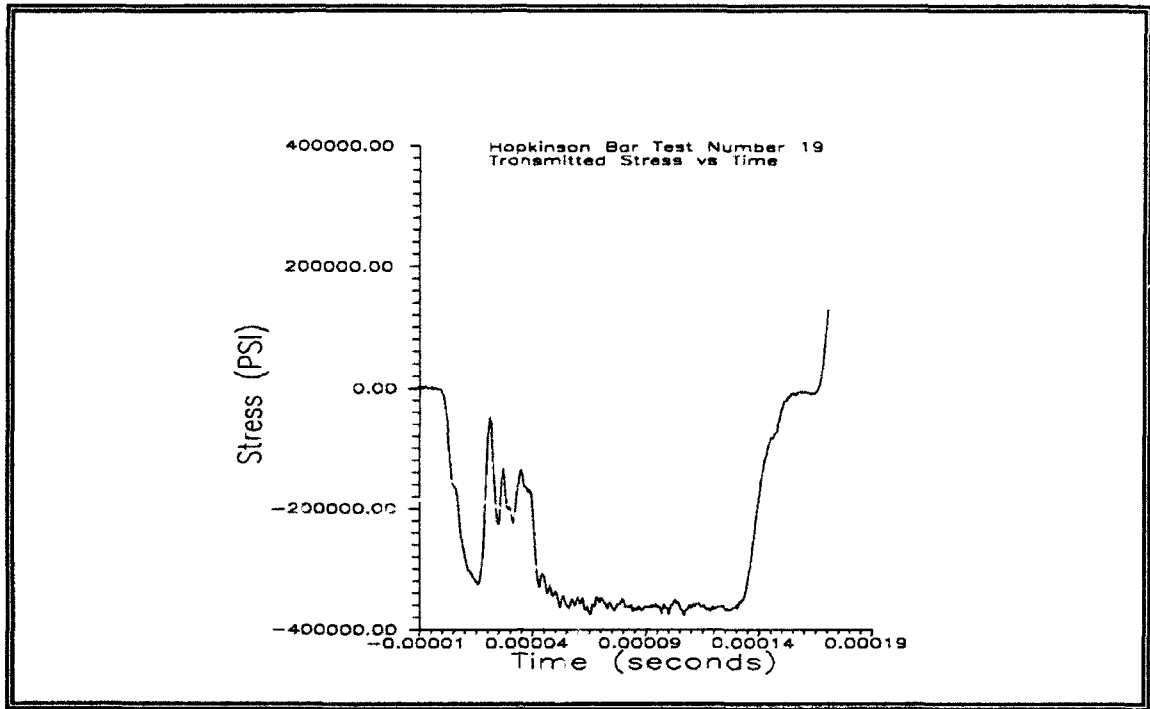


Figure 18. Hopkinson Bar Test 19 Detailed Stress

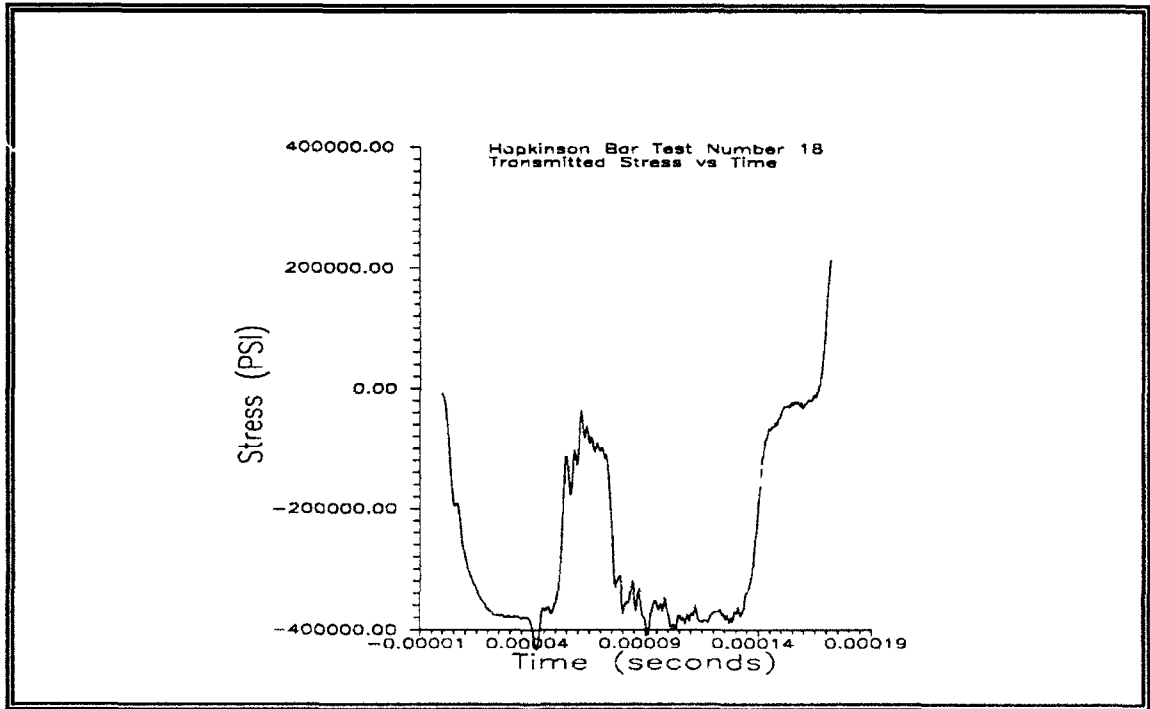


Figure 19. Hopkinson Bar Test 18 Detailed Stress

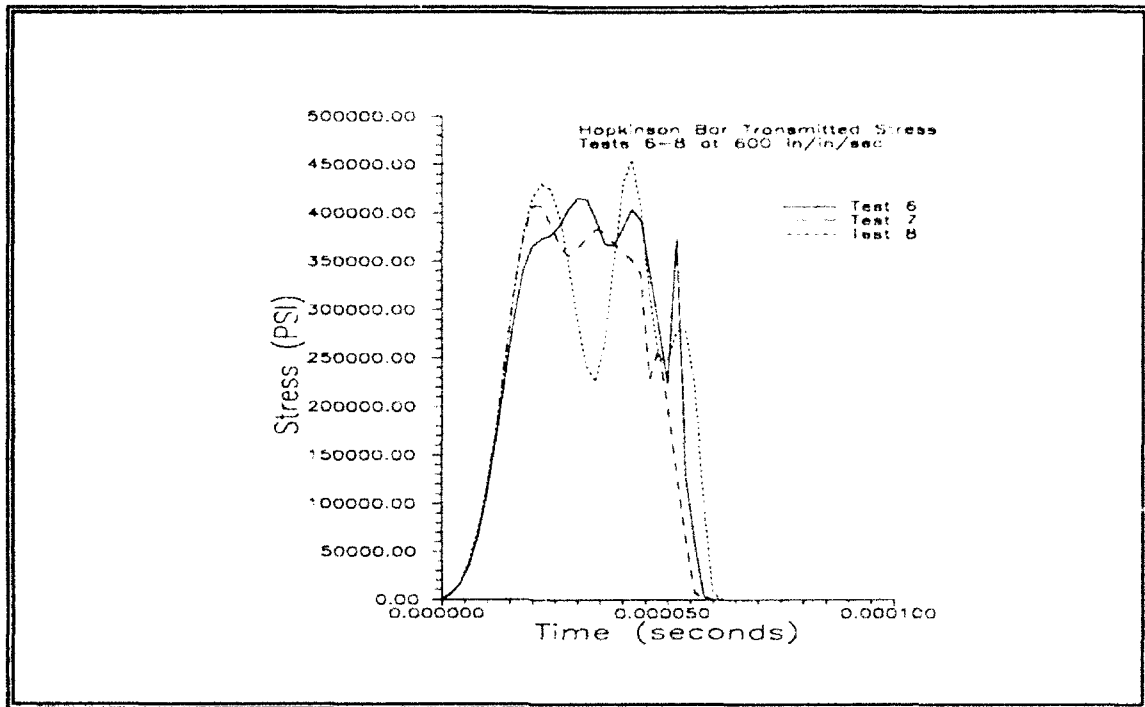


Figure 20. Transmitted Stresses in Tests 6-8

Figure 20 shows the transmitted stress data for tests 6-8. These tests were conducted at an average strain rate of approximately 600 in/in/sec as can be observed by assuming an elastic response of the alumina to the stress indicated over the rise time shown. This method of determining the strain rate in the specimen was elected rather than the more conventional use of the reflected wave in the incident bar because of concern over complex wave interactions in the protective 99 percent alumina disk. The average strain rate observed by conventional data reduction from the reflected wave in the incident bar was approximately three times the strain rate determined from

the transmitted wave. Of particular importance here is the period of steady stress and the non-instantaneous unloading. This suggests a period of plastic-like flow followed by a finite time for cracking and subsequent strength loss.

Figure 21 shows an apparent strength dependence on strain rate for alumina based on the data presented above. The data were fitted based on a strain rate normalized to the quasi-static strain rate of .001 in/in/sec. As discussed above, the strain rates shown in this figure for the Hopkinson bar were determined assuming elastic response of the specimen in its early, linear response stage, and were based on the transmitted stress pulse. The dynamic strength  $\sigma_d$  was determined to be related to the quasi-static strength  $\sigma_s$  by the relation:

$$\sigma_d = \sigma_s \left( \frac{\dot{\epsilon}}{0.001} \right)^{0.037} \quad (5-1)$$

The solid line in Figure 21 represents this fit. The value of the exponent would change from 0.037 to 0.030 if the strain rates for the Hopkinson bar tests were based on the conventional method of integrating the reflected pulse in the incident bar. Figure 22 shows the physical effects of different strain rates on the compressive specimen. These photographs are approximately four times actual size. Much smaller fragments were obtained at higher strain rates.

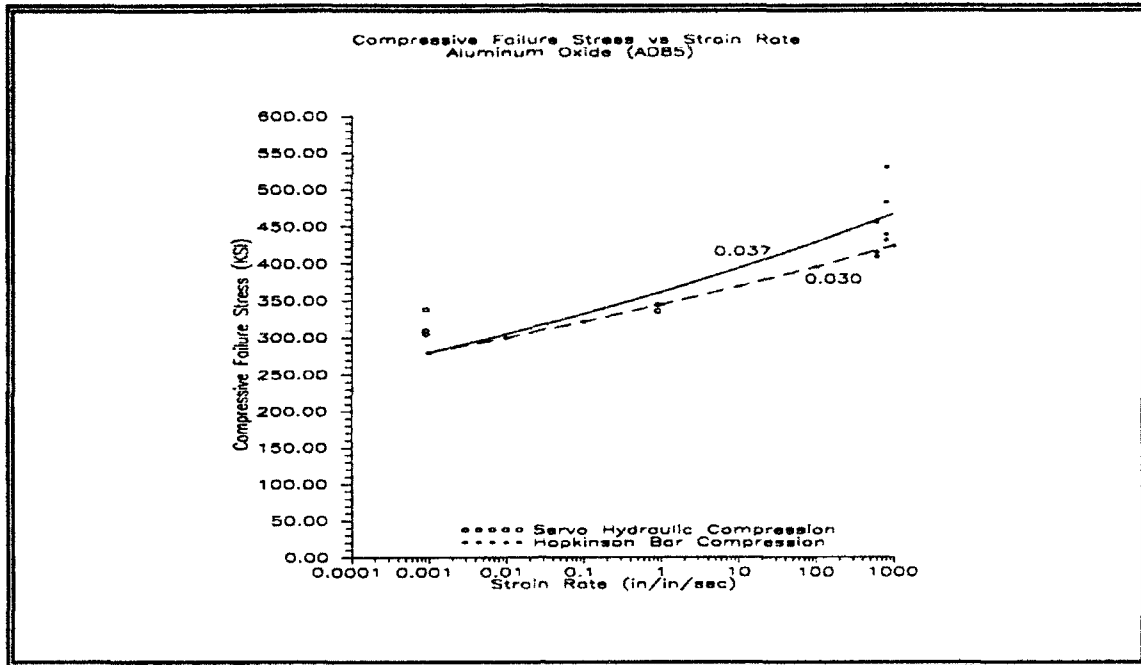
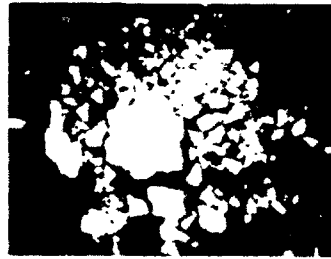


Figure 21. Compressive Stress vs. Strain Rate

## COMPRESSIVE TESTS



QUASI-STATIC COMPRESSIVE TEST



HOPKINSON BAR COMPRESSIVE TEST

Figure 22. Low vs. High Strain Rate Failed Compressive Specimen (4X)

Table 6 presents a summary of the average pore size and standard deviation of pore size in AD85 for several different levels of compressive loading prior to examination. Pore sizes were measured using a Bausch and Lomb Omnicon 3000 Series image analysis system. The distribution of pore sizes in 15 sample areas were used to obtain an average pore size. The reported pore sizes were diameters of circles with areas equal to the observed irregular cross-sections of pores detected by image contrast. No changes in pore size were observed that could be directly related to compressive loading.

Table 6. Pore Size after Compressive Loading

Peak Compressive Stress Pulse (KSI)	Average Pore Size (microns)	Standard Deviation of Pore Size
Virgin Material (0)	6.20	1.47
Virgin Material (0)	9.00	2.39
Quasi Static Load (290)	7.20	1.42
Hopkinson Bar (290)	8.13	1.81
Hopkinson Bar (317)	7.13	1.88
Hopkinson Bar (343)	8.07	0.96
Hopkinson Bar (360)	10.93	1.16

#### Plate Impact Tests

The plate impact test setup is shown in Figure 23, with details of the catch chamber and sabot illustrated in Figure 24. Figure 25 is a photograph of the first actual sabot, flier plate, and target. This hardware evolved considerably during the testing. The two inch diameter of the light gas gun was insufficient for use of the star-shaped flier plates

originally planned and shown in Figure 25. The star shape was preferred since edge reflections from the star tips have been demonstrated to interact, minimizing tensile reflections to the center of the target plate. Most tests were performed with round flier plates, which provided a larger area for the catch chamber to stop the plate and sabot after impact.

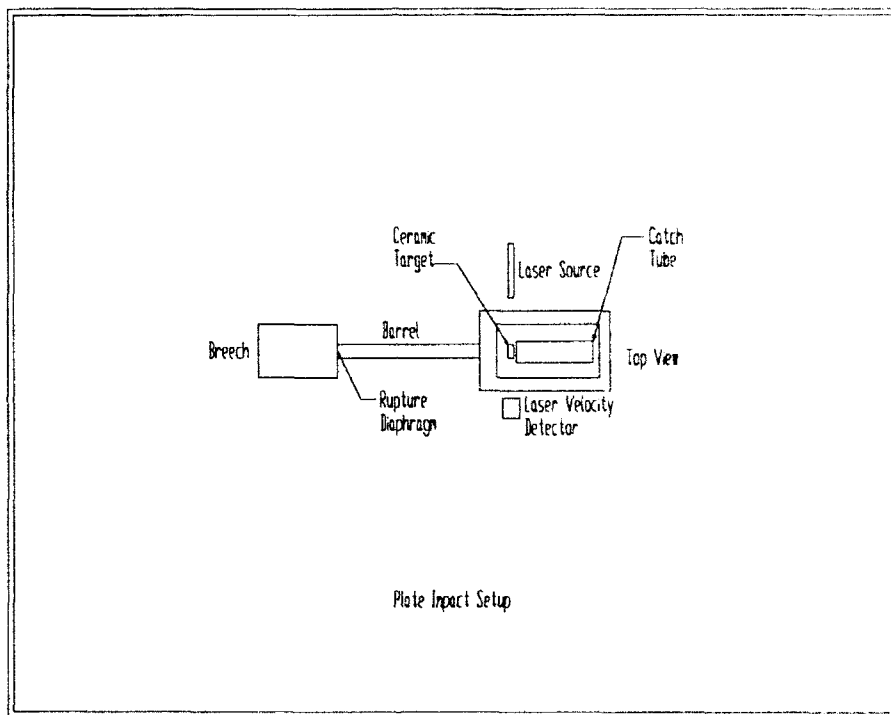


Figure 23. Plate Impact Setup

The detailed drawing of the plate impact test hardware shows how the ceramic plate was mounted in a metallic confining ring for these tests. The confined ceramic plate was then mounted in a slip fit ring with a diameter slightly smaller than the diameter of the flier plate mounted on a

polypropolux sabot. The confined ceramic plate was allowed to protrude slightly in front of the sliding ring, so that a complete loading from impact occurred before the catch stand stopped the flier plate and the sabot, assuring that no secondary impacts occurred to cause additional ceramic damage. The catch chamber was designed with a slight interference fit on the sliding front support to absorb some of the sabot's energy, and the entire chamber was caught by a thin sheet of plywood that absorbed most of the launch energy. The impacted ceramic was soft-caught in rags in the catch chamber.

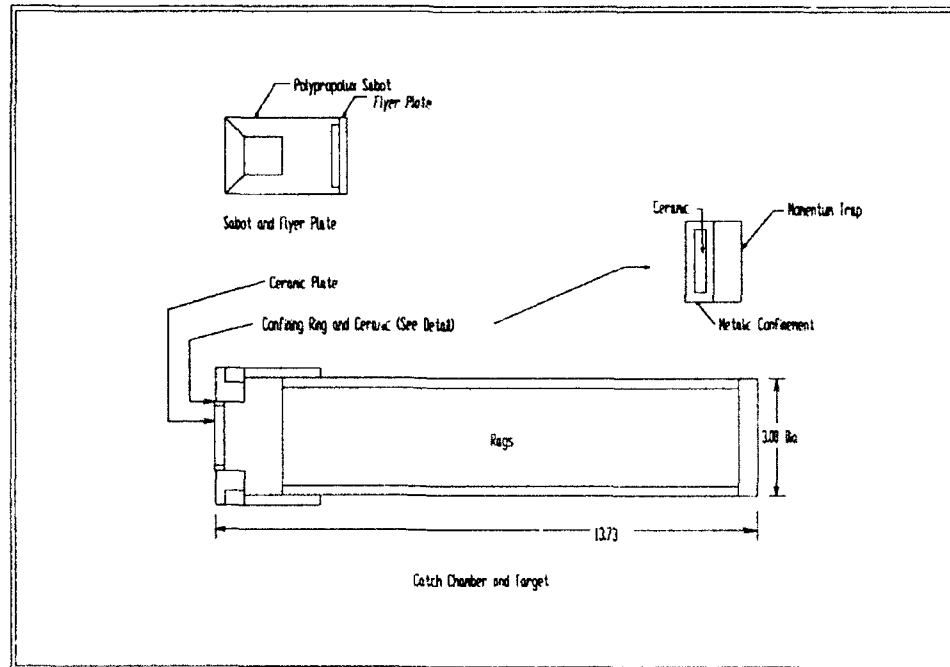


Figure 24. Plate Impact Test Hardware

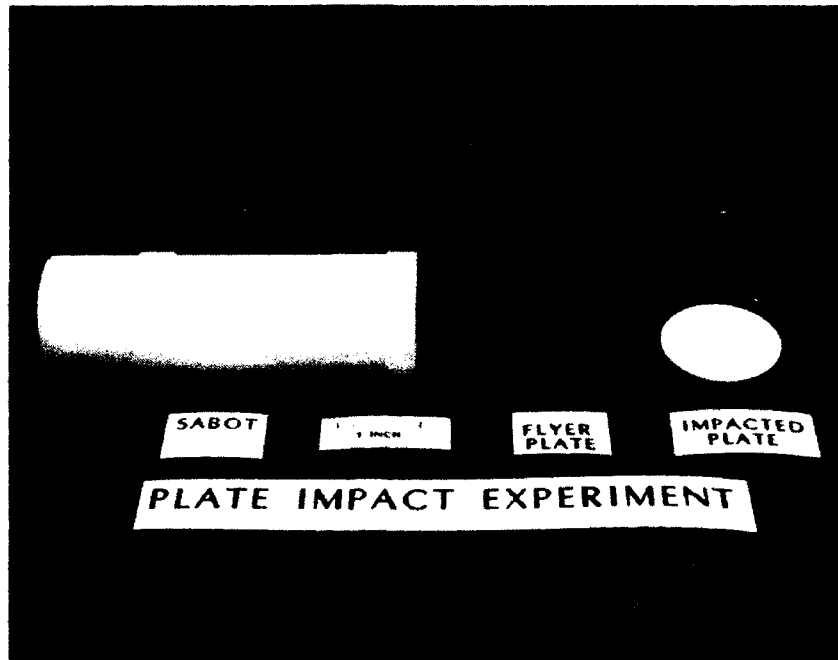


Figure 25. Original Plate Impact Test Hardware

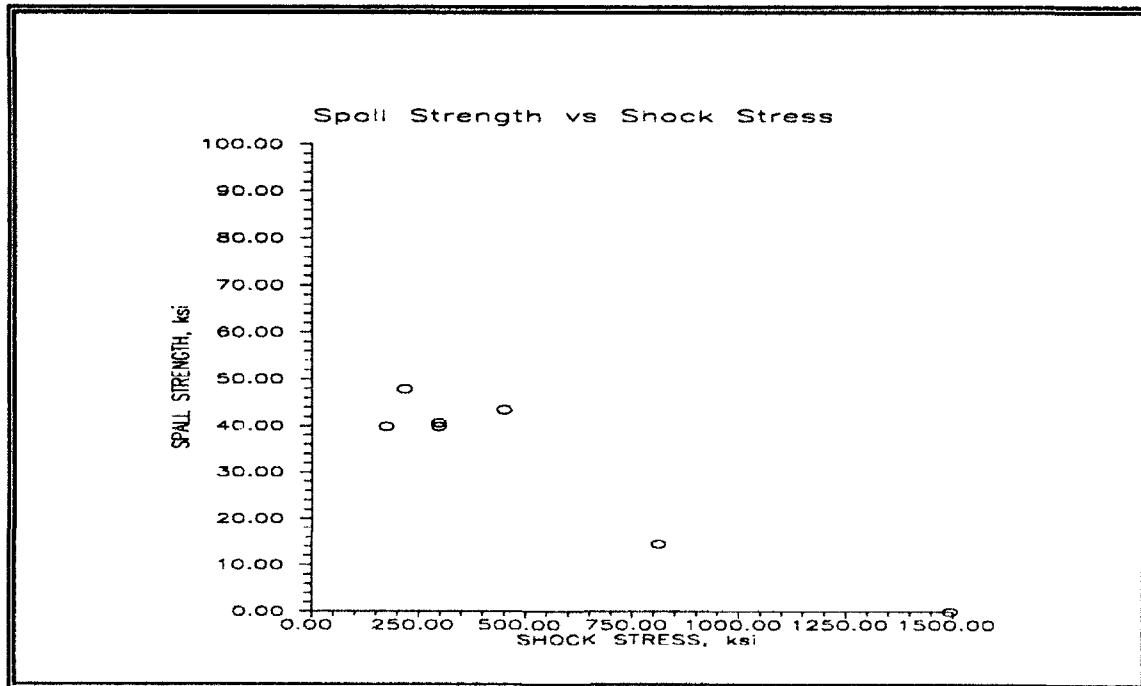


Figure 26. Spall Strength vs. Shock Stress

Non-recovery plate impact tests by other researchers demonstrated degradation in spall strength in plate impact tests as a function of the applied shock stress. Figure 26 shows this effect based on data from Yaziv [39]. The decrease in the tensile spall strength has been attributed to damage in the impacted plate that occurs from the high compressive stresses that occur during the passage of the shock wave prior to rear surface reflection leading to the spall. The tests performed here did not result in any recovered specimens with SEM observable damage not associated with complete cracks. As described in Chapter 3, the presence of microcracking is still being debated.

Clifton et al. [67] used carefully controlled plate impact tests with a pre-set gap between the rear of the target and a momentum trap. Using this technique, they recovered specimens damaged from impact velocities up to 351 ft/sec with loading durations of 25 microseconds. They report observing microcracks and describe modeling necessary to match the experiments to include rate dependence associated with time for initiation and propagation of microcracks.

Figures 27 and 28 demonstrate the basis for determining the stresses obtained in the targets of the plate impact experiments. These figures are based upon the relationship easily derived from the conservation equations and jump conditions requiring

$$S = \frac{U\rho_1c_1\rho_2c_2}{\rho_1c_1 + \rho_2c_2} \quad (5-2)$$

where  $S$  is compressive stress,  $\rho$  is density, and  $c$  is wave speed. Subscript 1 represents the impacting material and subscript 2 the impacted material. The material properties used for these predictions are given in Table 7. Computed stresses based on measured velocities, material properties in Table 7, and the above equation were used after preliminary tests with Manganin gages mounted on the back of unrecovered ceramic plates confirmed this technique.

Table 8 summarizes 13 plate impact tests performed. Impact velocities were varied to obtain different stress pulse levels; impactor thicknesses were varied to obtain different stress pulse duration; and impactor materials were varied to obtain different stress pulse levels and different impedance matches with the steel confinement on the target ceramic.

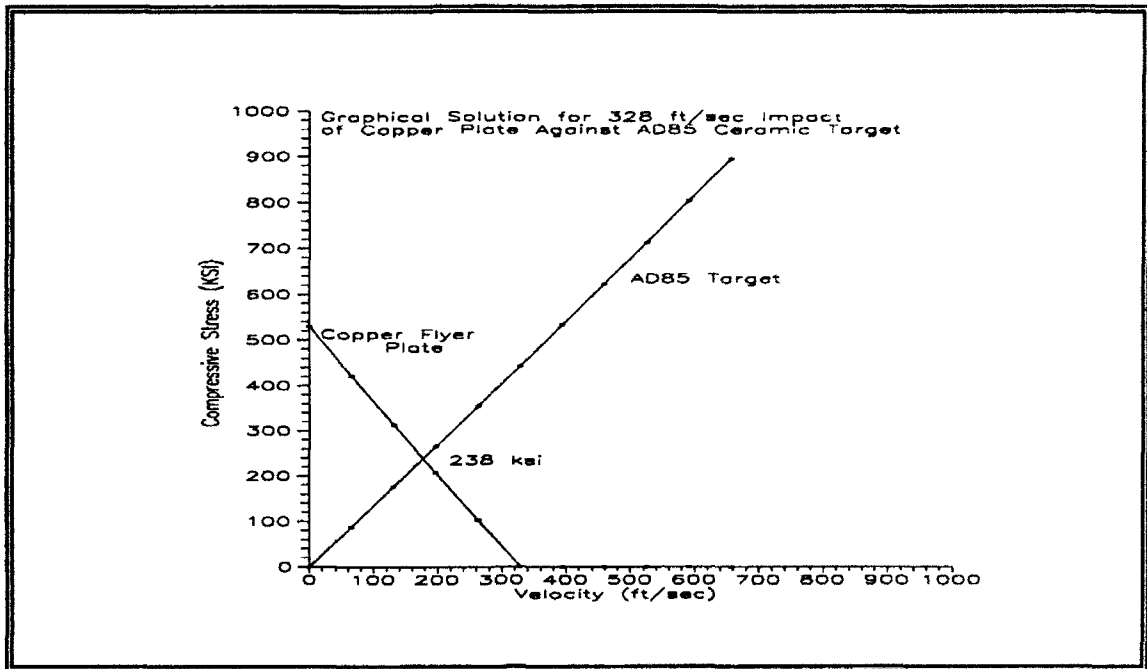


Figure 27. Compressive Stress Achieved Based on Hugoniots

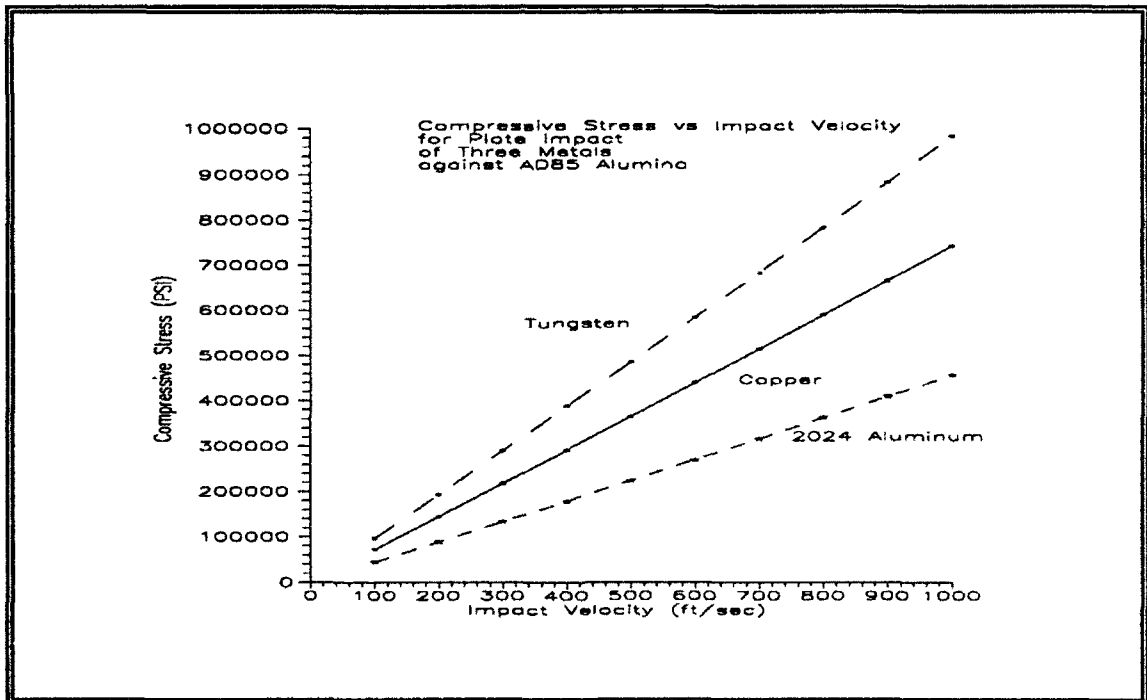


Figure 28. Compressive Stress as a Function of Impact Velocity

Table 7. Material Properties for Stress Predictions

Material	Density (lbm/ft <sup>3</sup> )	Wave Speed (ft/sec)	Impedance (lbm/ft <sup>2</sup> -sec)
Stainless Steel	492.50	14,990	7,382,575
Copper	556.98	12,926	7,199,523
Aluminum	173.70	17,480	3,036,276
Tungsten	1199.00	13,220	15,850,780
Alumina	213.31	29,000	6,185,990

Table 8. Plate Impact Tests

Test Number	Impact Velocity (ft/sec)	Impactor Material	Impactor Thickness (in)	Ceramic Thickness (in)
1	695	Copper	0.052	0.125
2	963	Copper	0.052	0.125
3	1377	Copper	0.052	0.125
4	911	Copper	0.102	0.125
5	873	Copper	0.150	0
6	978	Copper	0.052	0.187
7	947	Copper	0.052	0.250
8	998	Aluminum	0.052	0.125
9	891	Tungsten	0.100	0.125
10	834	Copper	0.052	0.125
11	920	Copper	0.052	0.125
12	1132	Copper	0.052	0.125
13	1126	Copper	0.052	0.125

#### Rod-on-rod Impact Tests

Rod-on-rod impact tests represent a type of experiment that provides higher strain rates than the Hopkinson bar with the added complexity of a stress state varying from uniaxial strain at the impact point to uniaxial stress several diameters away from the impact point. In the region

of most interest, from zero to two diameters from the impact point, the stress state is dramatically affected by release waves from the rod's outer diameter, so data reduction requires complex analysis, such as the use of a hydrocode.

A schematic of the rod-on-rod test configuration is shown in Figure 29, and a photograph of the test specimen is shown in Figure 30. Table 9 summarizes the 22 rod-on-rod impact tests performed.

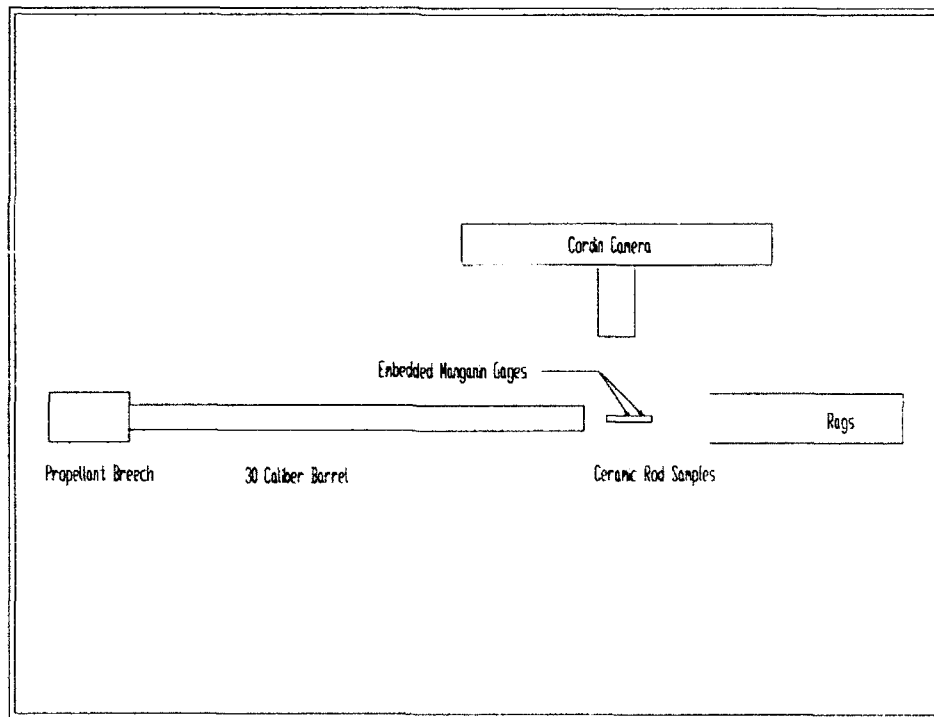


Figure 29. Rod-on-rod Test Apparatus

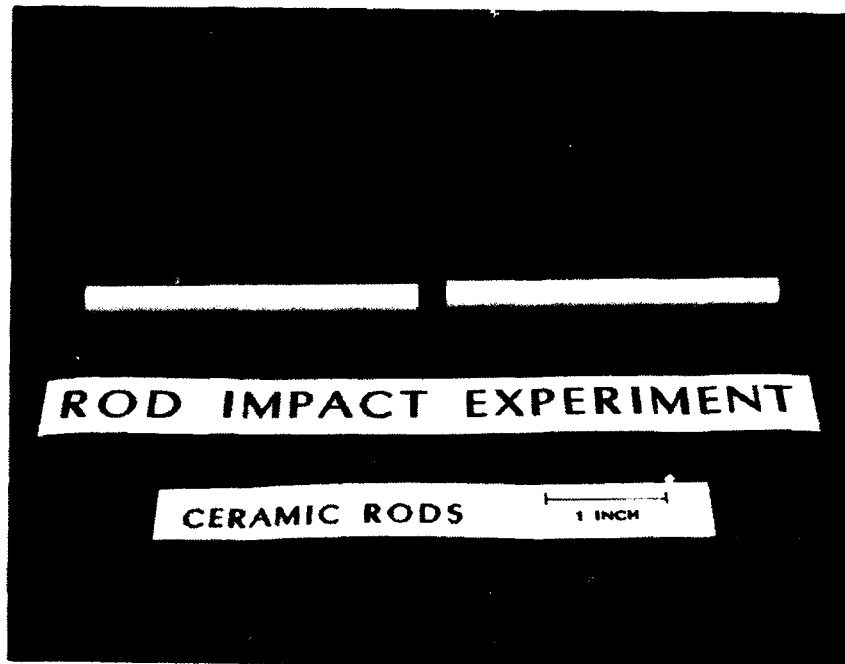


Figure 30. Rod-on-rod Impact Test Specimen

Table 9. Rod-on-rod Impact Tests

Test No	Test Configuration (all dimensions inches)	Velocity (Ft/Sec)	Peak Stress (KSI)	Peak Stress (KSI)	Peak Stress (KSI)	Peak Fracture Velocity (Ft/Sec)
1	0.5" 5"->5" MG 1.65"	584	355			
2	0.5" 5"->5" MG 1.65"	778	293			
3	0.5" 5"->0.5" MG 0.5" MG 1" MG 1.65"	452	362	305	276	
4	0.3" 3"->FG 3"	486				
5	0.3" 3"->0.33" MG 0.33" MG 0.66" MG 1.66"	412	247	196	247	
6	0.3" 3"->0.33" MG 0.33" MG 0.66" MG 1.66"	344	239			
7	0.3" 3"->3"	551				5170
8	0.3" 3"->0.33" MG 0.33" MG 0.66" MG 1.66"	416	319	232	305	
9	0.3" 3"->FG 3" MG 1"	493				
10	0.3" 3"->FG 3" MG 1"	605		392		
11	0.3" 3"->FG 3" MG 1"	705				6460
12	0.3" 2"->2" SG 1" MG 1" MG 1.5" SG 1"	238	247	232		
13	0.3" 2"->2" SG 1" MG 1" MG 1.5" SG 1"	642	450			7160
14	0.3" 2"->2" SG 1" MG 1" SG 1.5"	852	421	392		7720
15	0.3" 3"->0.33" MG 0.33" MG 0.66" MG 1.66"	661	370			
16	0.3" 3"->0.33" MG 0.33" MG 0.66" MG 1.66"	700	464	457	450	
17	0.3" 3"->0.5" MG 0.5" MG 1" MG 1"	465	421	392	363	
18	0.3" 3"->0.5" MG 0.5" MG 1" MG 1"	559	450	450	421	
19	0.3" 3"->0.5" MG 0.5" MG 1" MG 1"	548	276	319	290	
20	0.3" 1"->0.5" MG 0.5" MG 1" MG 1" - 2" T Recovery	741	493	471	471	
21	0.3" 1"->0.5" MG 0.5" MG 1" MG 1" - 2" T Recovery	747	609	529	457	
22	0.3" 1"->0.5" MG 0.5" MG 1" MG 1" - 2" T Recovery	779	522	486	442	

Notes: MG=Manganin Gage SG=Strain Gage  
T=Momentum Trap

Results of rod-on-rod impact tests at four different velocities are shown in Figure 31. These photographs were taken at 500,000 frames per second using a Cordin model 330A high speed turbine driven camera in framing mode. The light source was a single pulsed Xenon tube from a system also manufactured by Cordin. The light source was triggered using laser detectors in the flight path of the projectile to fire in synchronization with the impact event, based on a time delay assuming planned launch velocities. Kodak ASA 3200 black and white film designated T-Max 3200 provided the best photographic quality. The ceramic was painted with a very thin coat of flat black spray paint, and cracks were observed when the white ceramic was illuminated by the Xenon flash. For tests 13 and 14, the white material appearing behind the right rod is a polypropolux disk that was used as a protective pusher and barrel seal. In each test, the black object on the left, under the rod, is the support block for this stationary rod. The rod was supported on two sets of crossed pieces of thin wire to minimize effects on the impacted rod. Photo coverage was continuous at 2 microsecond intervals from before the impact to the last time shown. Photographs of the progression of fracture from 14 microseconds to the last times are not included because they provided little additional information for the space that they require.

Of particular interest is the transition from longitudinal cracking at the impact interface, to cross-sectional cracking near the rear surface of the impacted rod. At the lower impact velocities, these cracks are only observed at the last time shown for the impact sequence. At the highest velocity shown (852 ft/sec), the transverse crack near the rear surface is seen after 6 microseconds. This was caused by tensile fracture from waves reflected from the rear surface with the distance from the rear determined by the rarefaction wave from the outer diameter at the point of impact and its effect on the transmitted wave profile. Also notable was the strong symmetry across the impact plane. Based on arrival times of the elastic wave at the stress gages, an average longitudinal wave velocity of 27,300 ft/sec was measured with a standard deviation of 980 ft/sec. This confirmed the manufacturer's value of 27,000 ft/sec. Average observed crack zone speeds were observed over the first 14 microseconds of impact and found to be 5175 ft/sec for the 551 ft/sec impact, 6463 ft/sec for the 605 ft/sec impact, 7165 ft/sec for the 642 ft/sec impact, and 7721 ft/sec for the 852 ft/sec impact. Thus, the speed of propagation of the cracked region was observed to be approximately 19 percent to 28 percent of the longitudinal wave speed.

<----- Velocity = 551 Ft/Sec

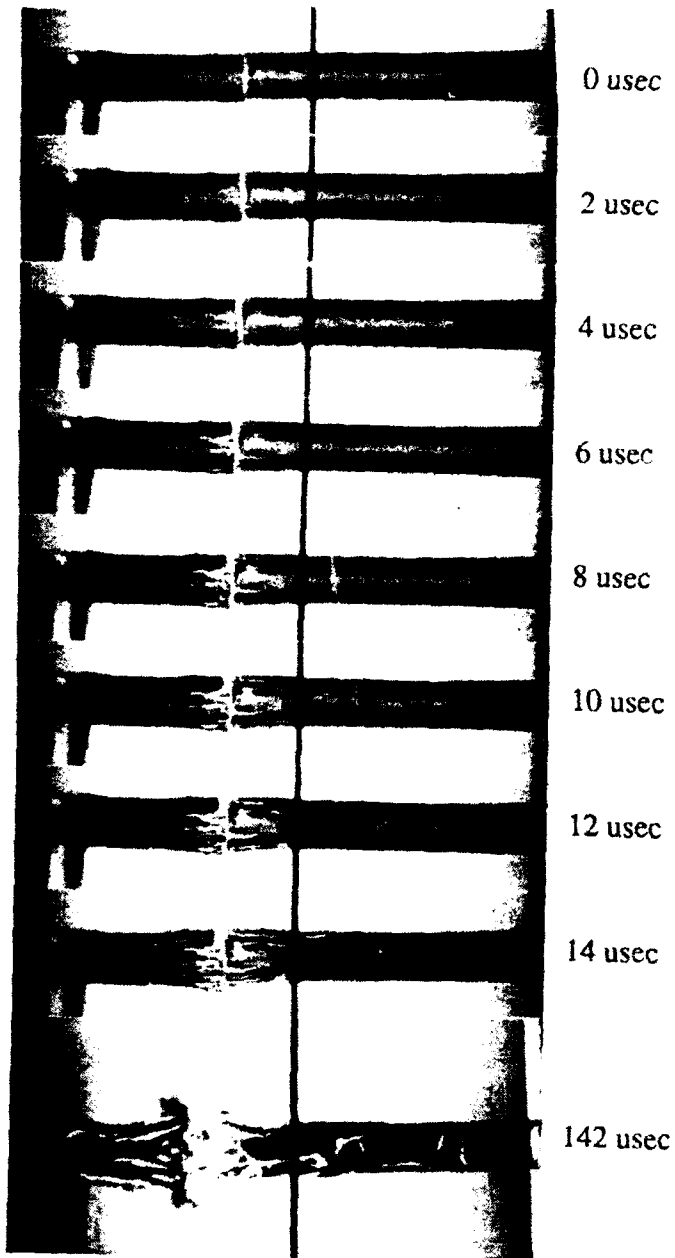


Figure 31. Rod-on-rod Impact at 500,000 Frames/Sec  
(Test 7)

<----- Velocity =605 Ft/Sec

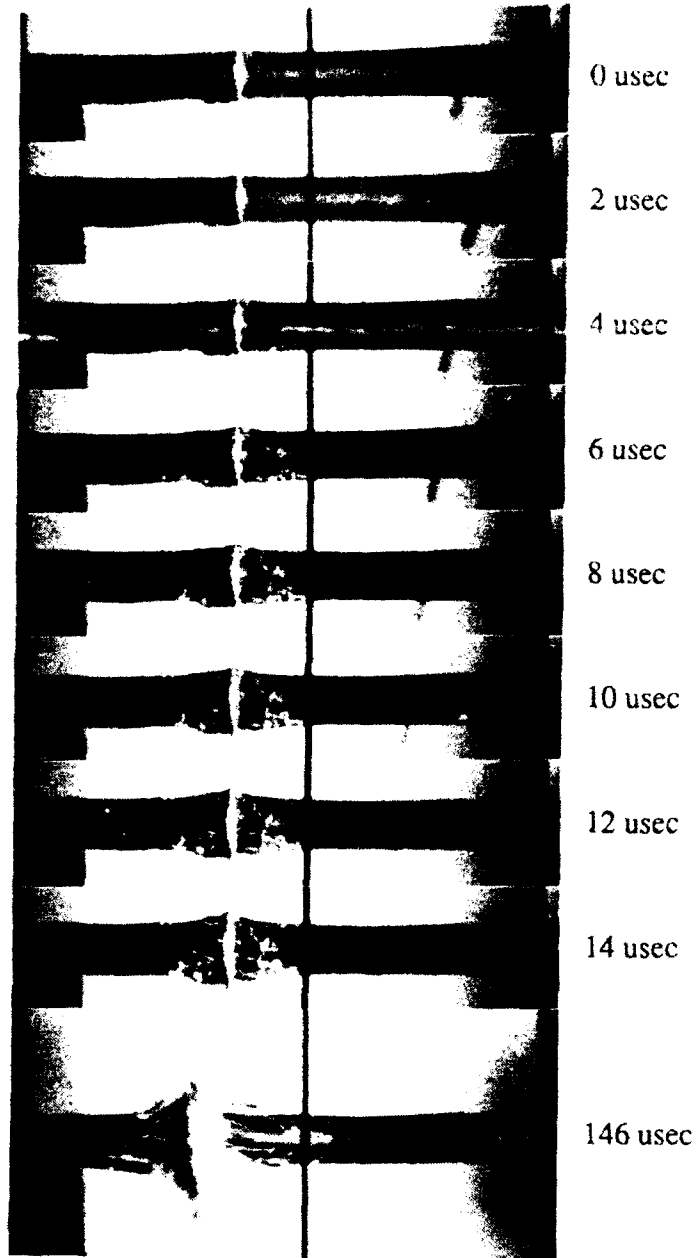


Figure 31(cont). Rod-on-rod Impact at 500,000 Frames/Sec (Test 10)

<----- Velocity = 642 Ft/Sec

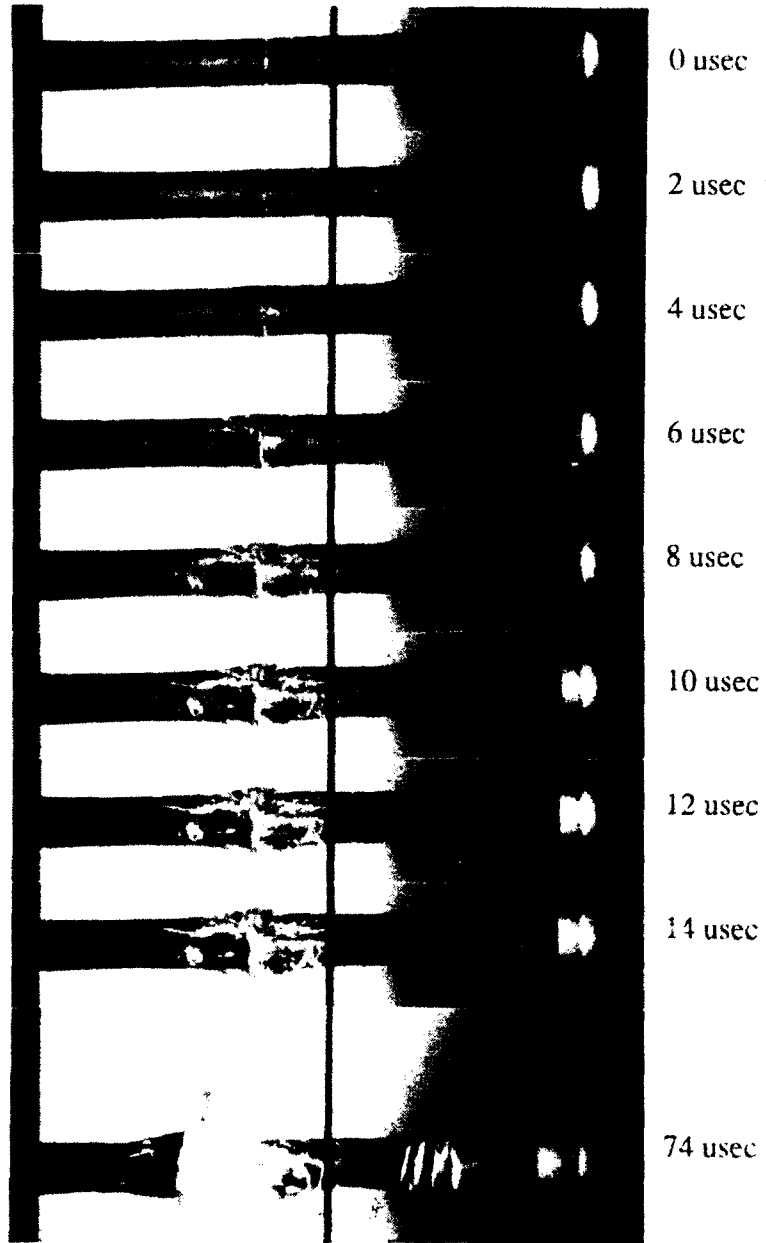


Figure 31(cont). Rod-on-rod Impact at 500,000 Frames/Sec (Test 13)

<----- Velocity = 852 Ft/Sec

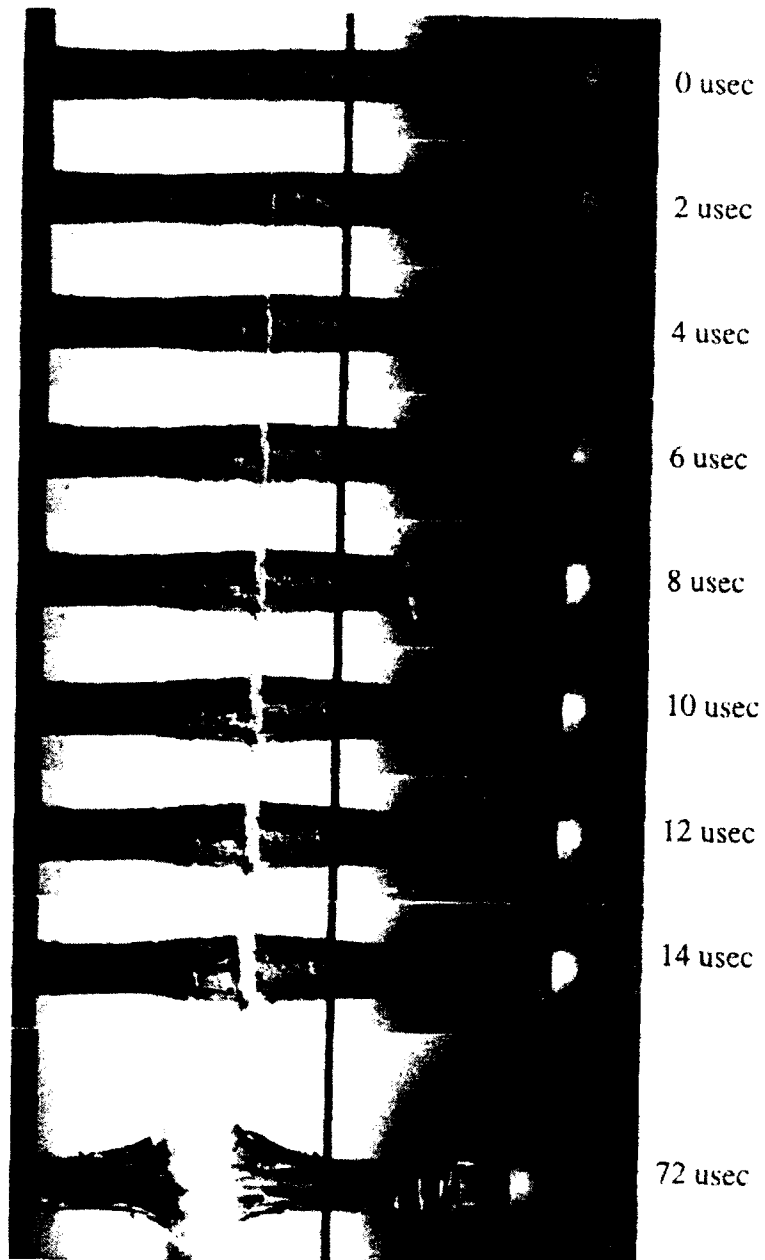


Figure 31. Rod-on-rod Impact at 500,000 Frames/Sec  
(Test 14) (Concluded)

Figures 32 and 33 show stress vs time histories measured at Manganin gage locations in the target rods for rod-on-rod experiments 6 and 22 at impact velocities of 344 and 779 ft/sec, respectively. Characteristics similar in both tests are the decrease in peak stress observed at distances further from the impact point as wave dispersion occurs and the stress state becomes uniaxial stress instead of uniaxial strain. Differences in the two tests are the magnitude of the pulse, the level of the residual pulse following the peak, and the duration of the peak pulse. The curves shown terminate due to failure of the gage or the loss of a meaningful signal because of electronically generated noise from the failure of another gage. Termination of the curve does not represent a zero signal level. Evidently failure is relatively rapid at the higher velocities, but it is not instantaneous, or stress pulses of the magnitude shown would not be transmitted down the rod to the second and third gages. Failure in the low velocity impacts either occurs after the failure of the stress gages, or the impact results in a fractured material with very nearly the same load carrying capacity as the unfractured material for the time of survival of the gages.

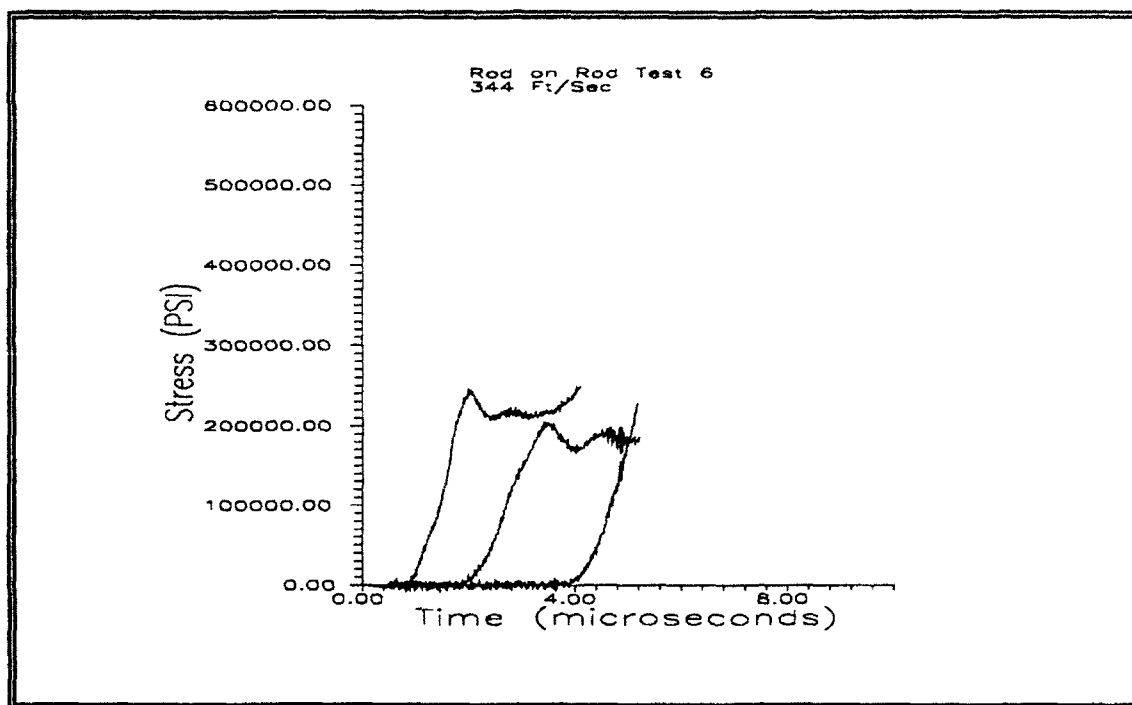


Figure 32. Stress vs. Time in Target Rod for Test 6

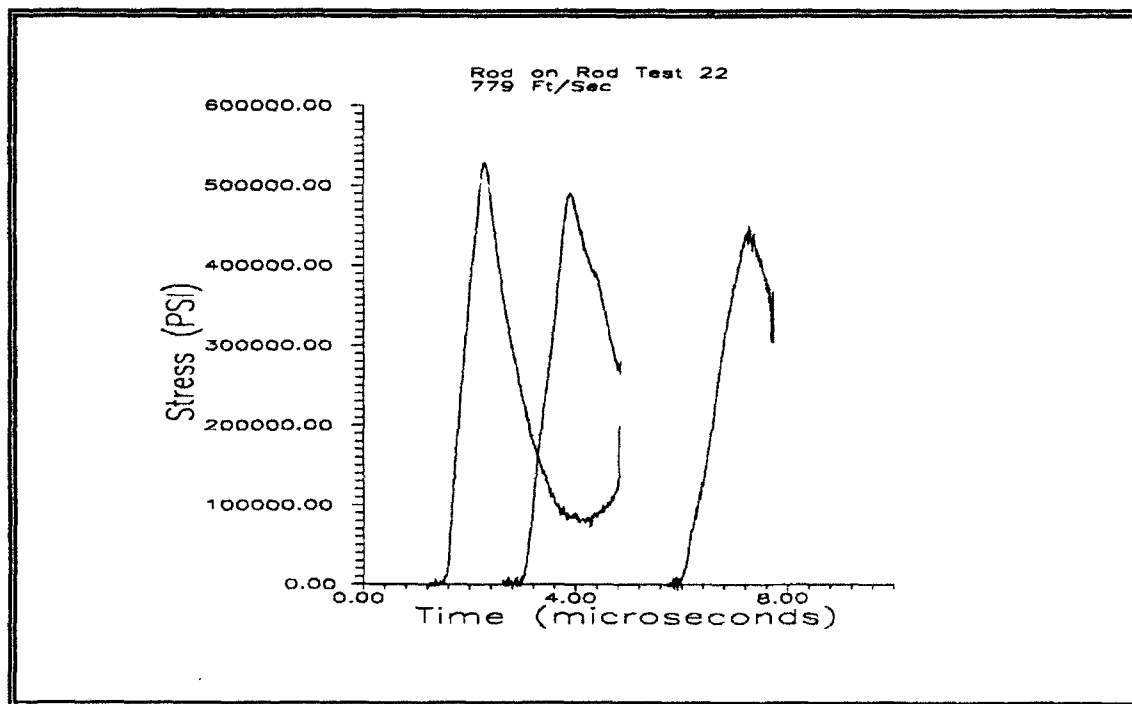


Figure 33. Stress vs. Time in Target Rod for Test 22

Figure 34 shows a complete summary of the stress gage measurements from Manganin gages placed in all of the target rods of the rod-on-rod impact experiments. The solid line represents the maximum expected stress based on uniaxial strain impact conditions, which should only be applicable very close to the impact point in the rods. Apparently some overshoot occurred in the instrumentation used to measure the peak stresses, since in several cases stresses above theoretically predicted stresses occurred. In general, however, peak stresses near the impact point were near the predicted theoretical stress, and stresses dropped at locations further down the rod.

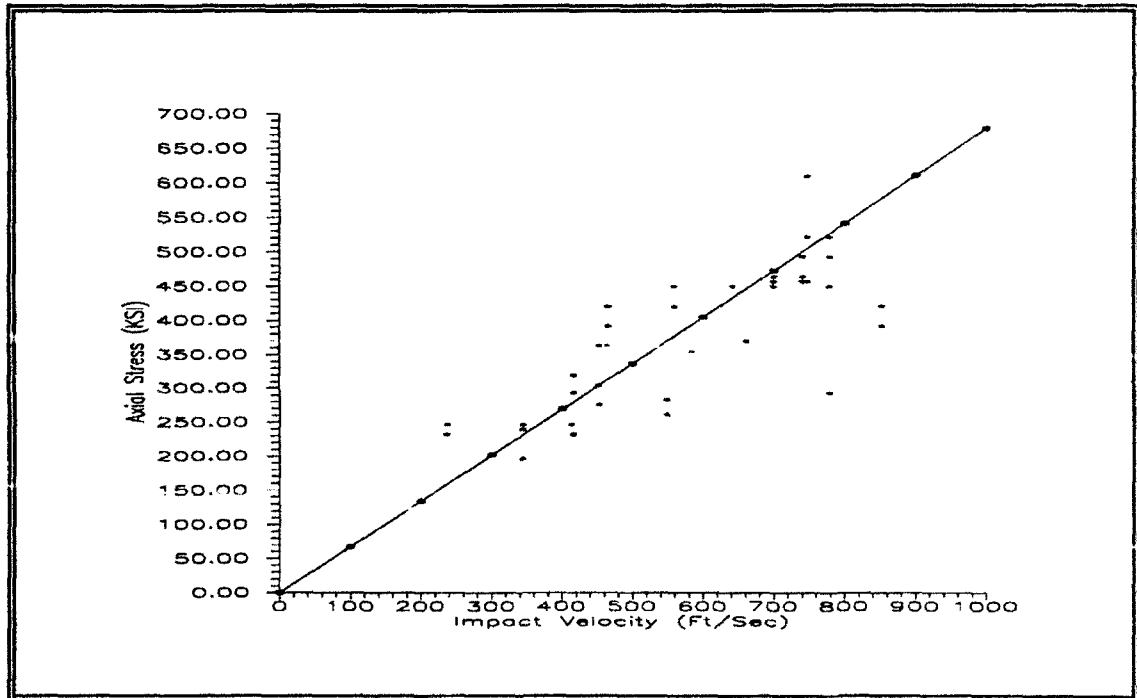


Figure 34. Measured Stresses in Rod-on-rod Impact Experiments

Penetration Experiments

Table 10 summarizes the 9 confined ceramic penetration experiments performed. A sketch of the test setup is shown in Figure 35. No instrumentation or camera coverage was used on these tests. The confining aluminum plate was preperforated at the impact point to eliminate the effects of the cover plate on the failure process of the ceramic. The opening in the cover plate was just sufficient for entry of the impacting projectile. Where possible, the recovered targets were sectioned and examined. Photographs of sectioned, recovered targets for tests 1 and 3 were presented in Chapter 1, Figures 2 and 3 respectively.

Table 10. Confined Ceramic Penetration Experiments

Test No	Velocity (Ft/sec)	Gun	Penetrator	Target	Notes
1	617	Air	Tantalum	Baseline	No Fracture
2	685	Air	Tantalum	Baseline	No Fracture
3	1320	Powder	Tantalum	Baseline	Tensile Cracks
4	1490	Powder	Tantalum	Baseline	Tensile Cracks
5	1536	Powder	Tantalum	Confined	Bad Sectioning
6	1710	Powder	Tantalum	Confined	Small Comp Zone
7	2033	Powder	4340	Confined	Small Comp Zone
8	2525	Powder	4340	Confined	Med Comp Zone
9	3420	Powder	4340	Thick Front	Med Comp Zone/ Recovered Cone

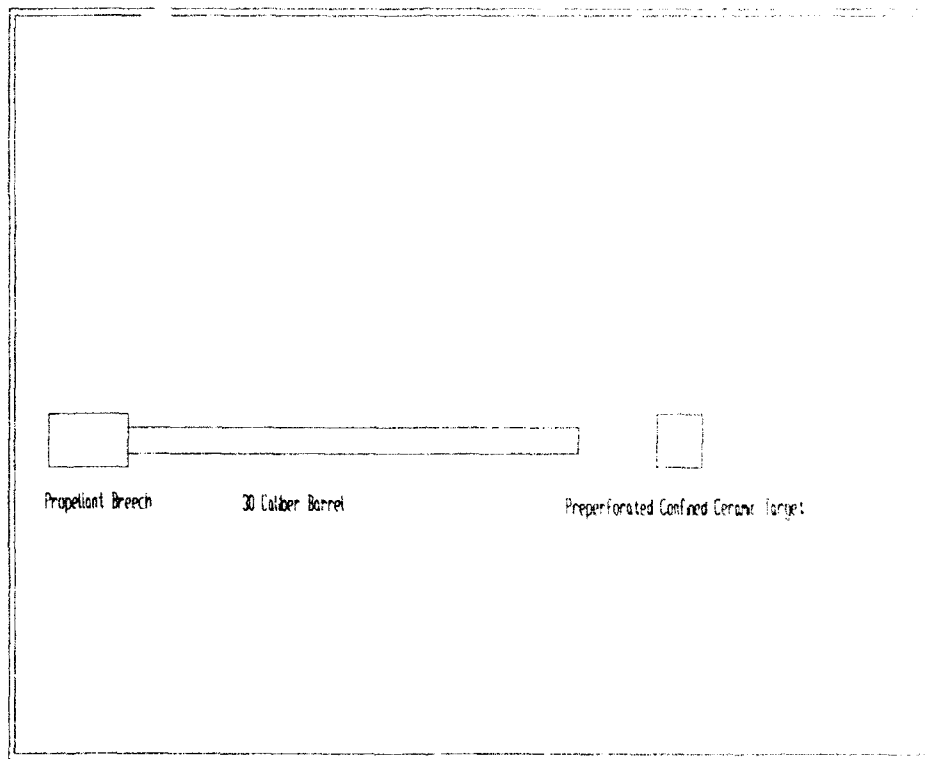


Figure 35. Penetration Experimental Setup

CHAPTER 6  
ANALYSIS OF EXPERIMENTS

Micrographic Study of Damaged Ceramic

As part of the evaluation of the Hopkinson Bar tests, the recovered specimens were sectioned, polished, and examined for evidence of arrested damage.

Crack sizes and distribution

Using the energy based model proposed by Grady (as discussed in Chapter 3), characteristic crack dimensions were calculated from Grady's equation:

$$l = \left( \frac{\sqrt{12} K_{Ic}}{\rho \dot{\epsilon} c_0} \right)^{\frac{2}{3}} \quad (6-1)$$

where  $l$  is crack length

$c_0$  is sound speed

$K_{Ic}$  is static fracture toughness

$\rho$  is density

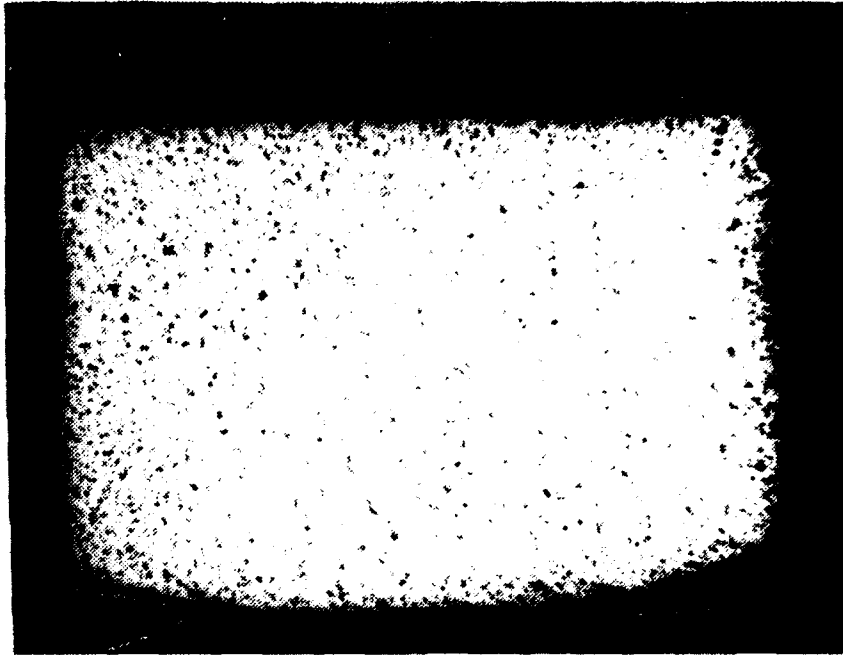
$\dot{\epsilon}$  is equivalent strain rate

For the compressive split Hopkinson bar experiments, if the following values were appropriate ( $c_0=348,000$  in/sec,  $\rho=0.123$  lbm/in<sup>3</sup>,  $K_{Ic}=2730$  lb-in<sup>1/2</sup>/in<sup>2</sup>, and  $\dot{\epsilon}=800$  in/in/sec) then a characteristic crack size would be established

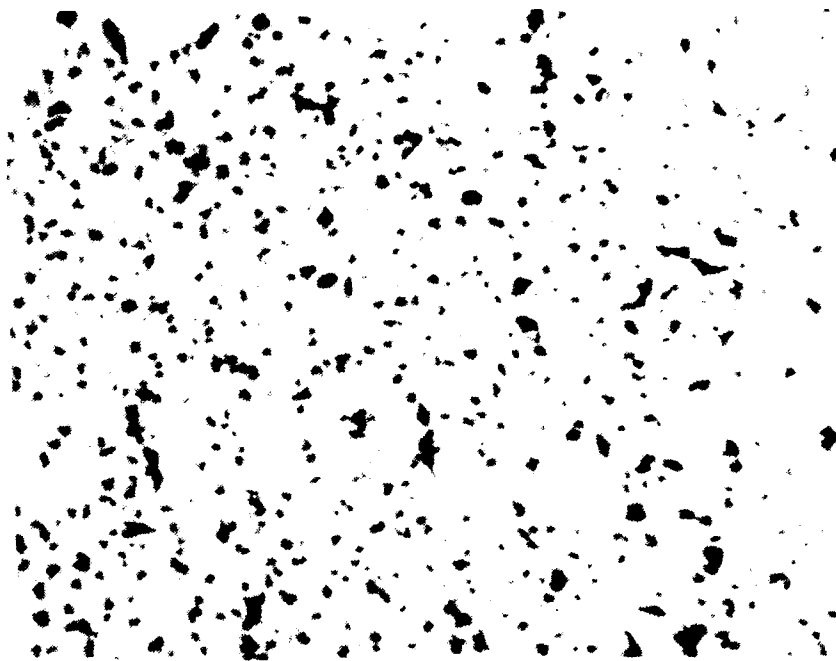
$$l = \left( \frac{\sqrt{12}(2730)(386.4)}{(0.123)(348,000)(800)} \right)^{\frac{2}{3}}$$

$$= 0.225 \text{ in}$$

This length corresponds to a fragment density of 88 fragments per cubic inch, and is longer than anything in the range of fragment sizes recovered. It is possible that the use of an average strain rate in the specimen for this calculation is not as meaningful as the use of local strain rates that could be much higher than the average, leading to the prediction of smaller fragments consistent with the experiments. Figures 36 and 37 show porosity and damage after controlled Hopkinson bar tests. Figure 36 is for compressive Hopkinson bar test 17, where a peak compressive stress of 343,000 PSI was achieved in the specimen, without causing fracture. Figure 37 is for test 19, where the peak compressive stress was 361,000 PSI, and fracture was achieved. These figures are offered for comparison to the photographs of untested material in Chapter 4, Figure 12. In both Figures 36 and 37, the first two photomicrographs are from an optical microscope at magnifications of 20 times and 120 times. The second two photomicrographs are from a Scanning Electron Microscope (SEM) at magnifications of 1000 times and 3000 times. The presence of microscopic damage was undetectable with the optical microscope and the Scanning Electron Microscope.

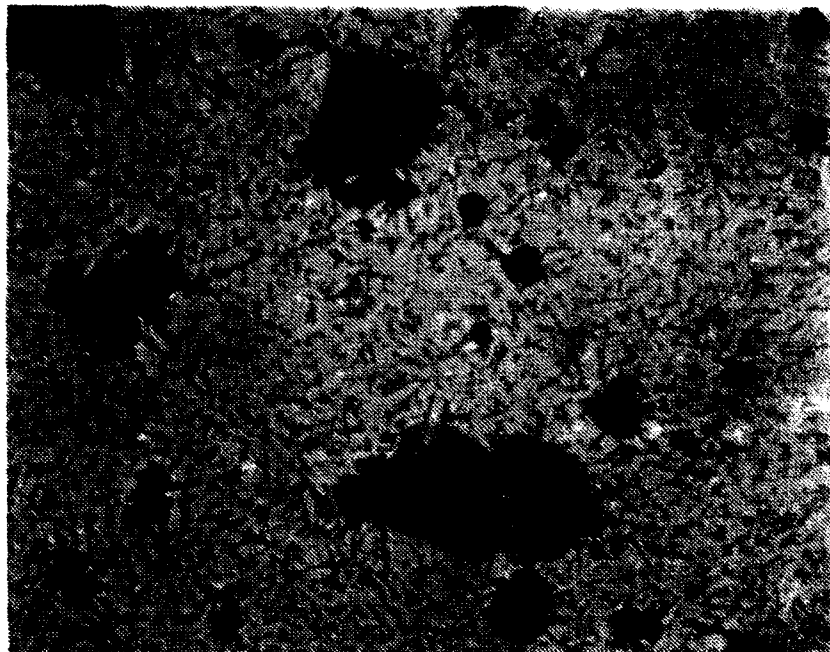


20X

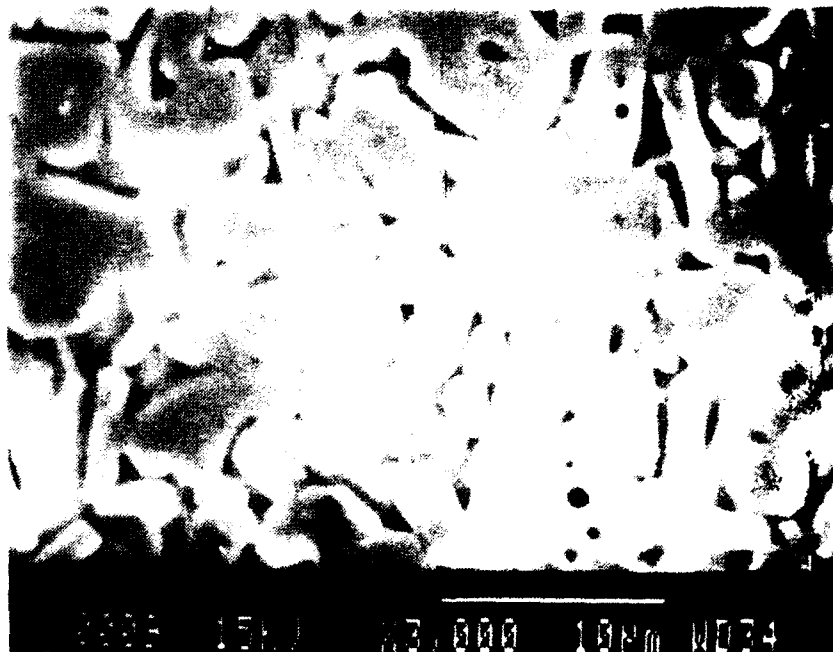


120X

Figure 36. Optical Photomicrographs  
343,000 psi (20X and 120X)



1,000X

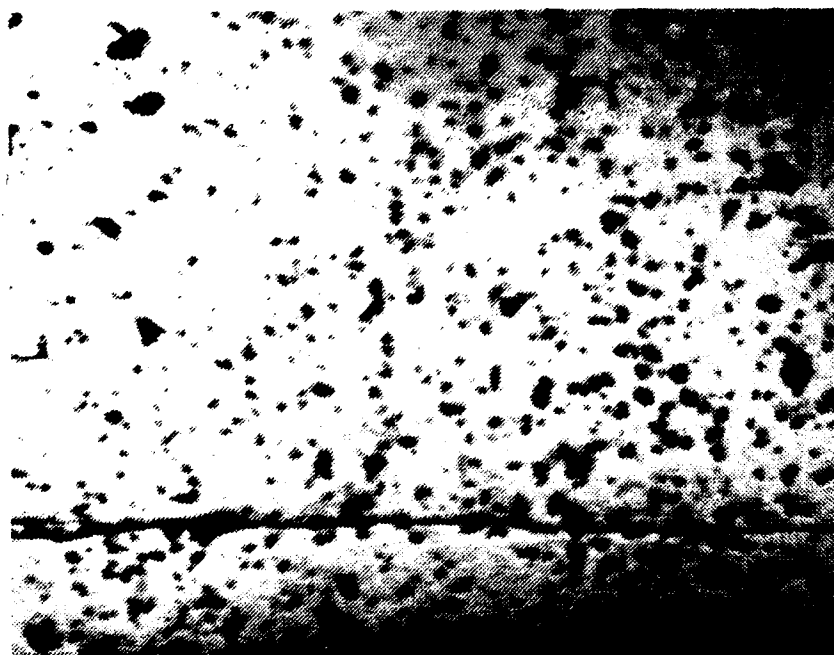


3,000X

Figure 36. SEM Photomicrographs 343,000 psi (1000X and 3000X) (Concluded)

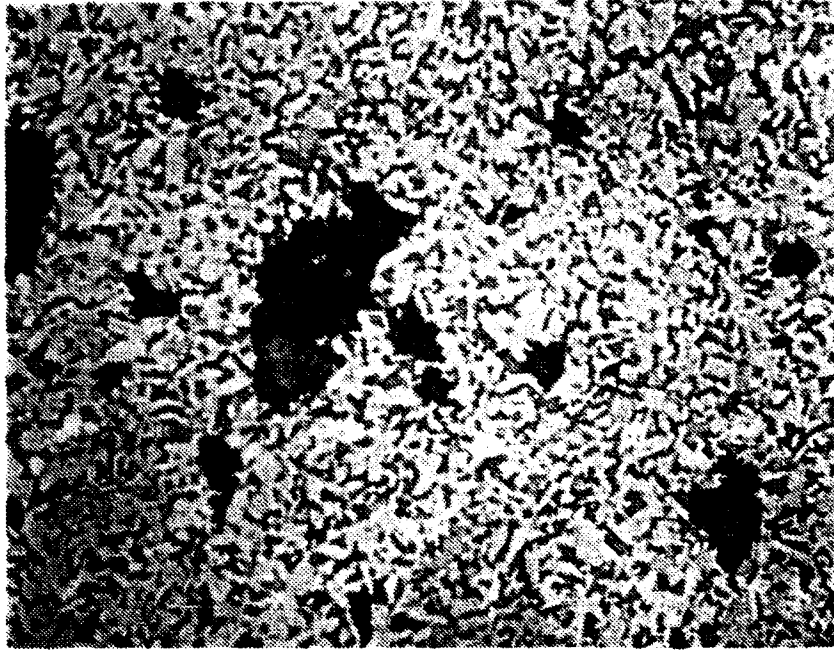


20X



120X

Figure 37. Optical Photomicrographs  
361,000 psi (20X and 120X)



1,000X



3,000X

Figure 37. SEM Photomicrographs 361,000 psi  
(1000X and 3000X) (Concluded)

## Failure surface analysis

### Damage as a Function of Loading

Figure 38 shows the effect of high strain rate compressive loading in the Hopkinson bar on the porosity. The porosity measurements were done on a Bausch and Lomb Omnicron Series 3000 image analysis system as described in Chapter 5. A pore count was obtained for 15 sample areas of each specimen, for pores of equivalent circular diameters from 2 to 30 microns in 2 micron bin sizes. The curves marked HPB 2.75, HPB 3.00, HPB 3.12, and HPB 3.25 refer to drawbacks in inches for the spring launched impact bar on the Hopkinson Bar apparatus, and correspond to maximum stresses in the specimen of 290, 317, 343, and 360 KSI respectively. The Instron test was performed to a stress of 290 KSI. Pore counts were not affected by the experiments.

Figure 39 shows damage in alumina caused by a typical plate impact test. Microscopic damage under an SEM was unremarkable except in association with the cracks observed here under the optical microscope. Figures 40, 41, and 42 all show the damage resulting from plate impact tests. An increase in crack density with loading is directly observable. Table 11 summarizes the observed results from the plate impact tests.

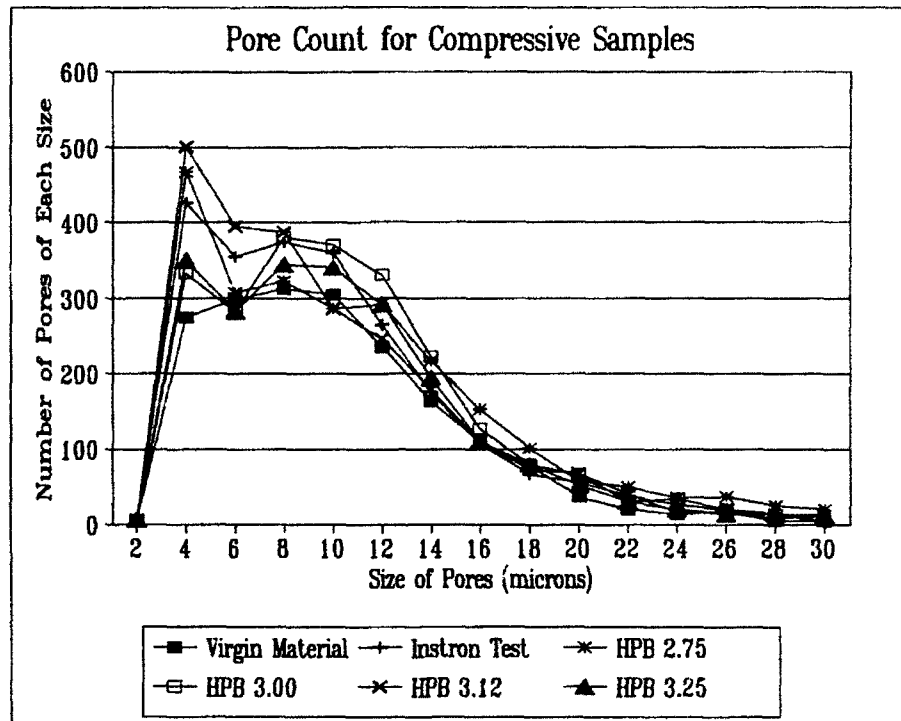
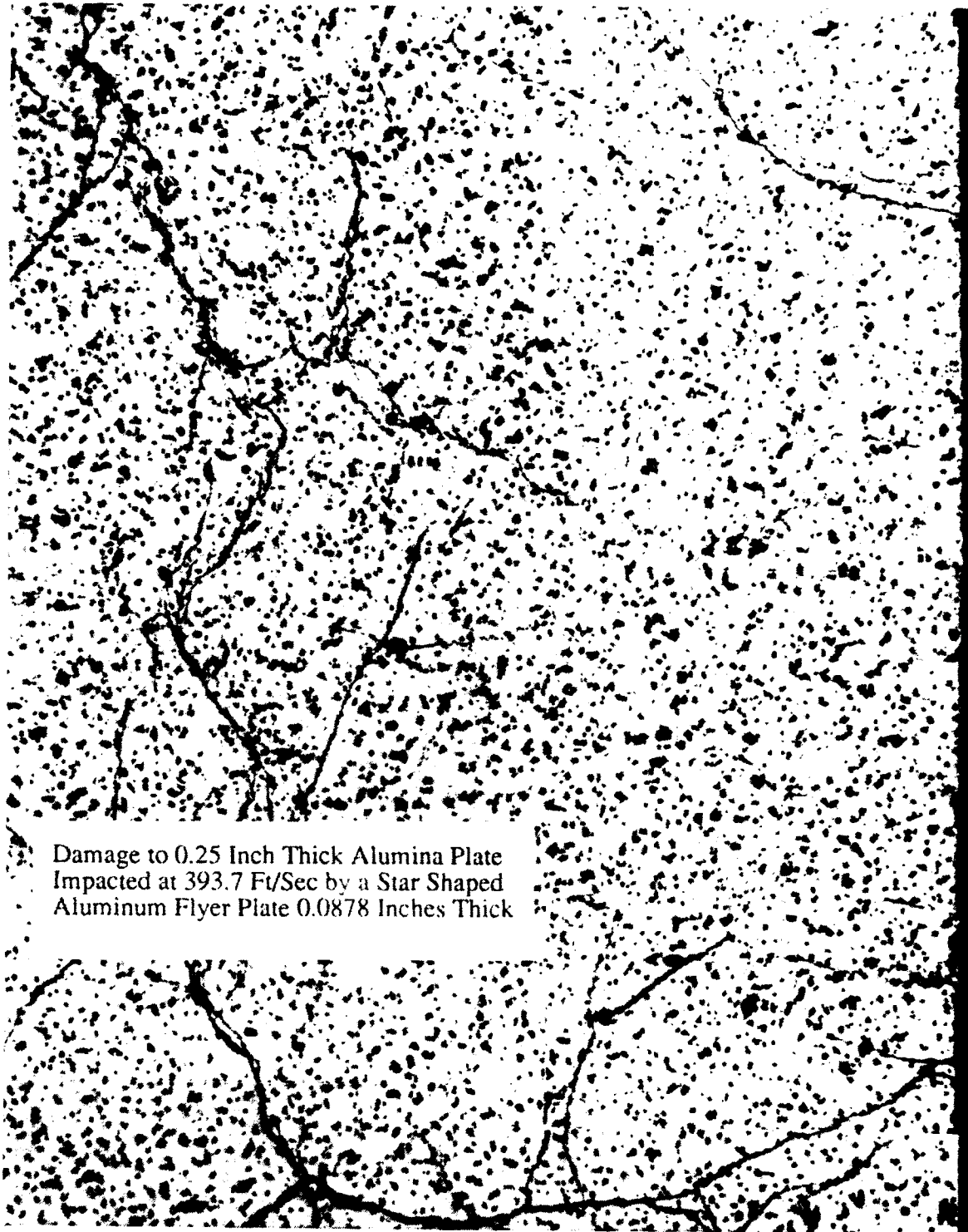


Figure 38. Post Test Porosity of Compressive Specimens



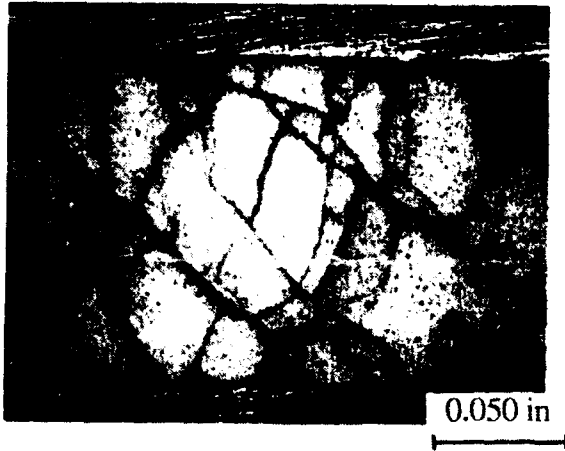
Damage to 0.25 Inch Thick Alumina Plate  
Impacted at 393.7 Ft/Sec by a Star Shaped  
Aluminum Flyer Plate 0.0878 Inches Thick

Figure 39. Typical Plate Impact Damage at 52.3X  
Magnification



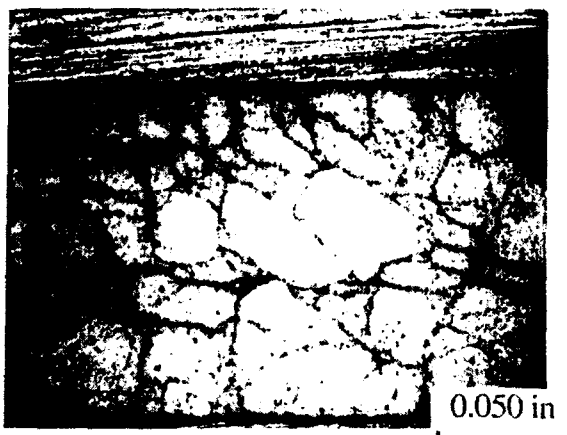
## Low Velocity

695 Ft/Sec  
Copper Flyer Plate  
0.052 Inches Thick



## Intermediate Velocity

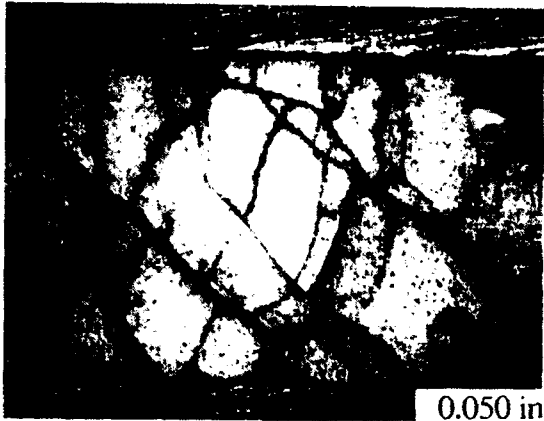
834 Ft/Sec  
Copper Flyer Plate  
0.052 Inches Thick



## High Velocity

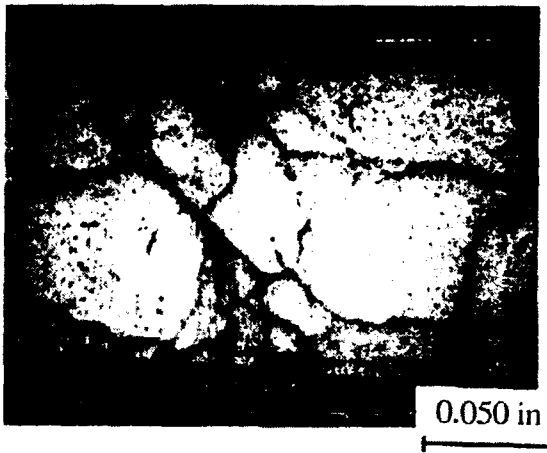
1126 Ft/Sec  
Copper Flyer Plate  
0.052 Inches Thick

Figure 40. Damage in Impacted Plate vs. Load Magnitude



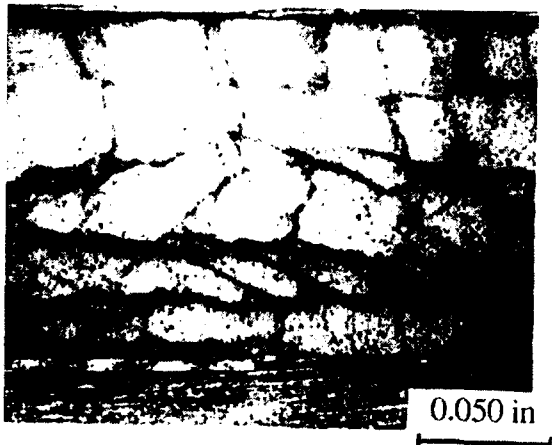
Short Pulse

0.052 Inches Thick  
Copper Flyer Plate  
834 Ft/Sec



Intermediate Velocity

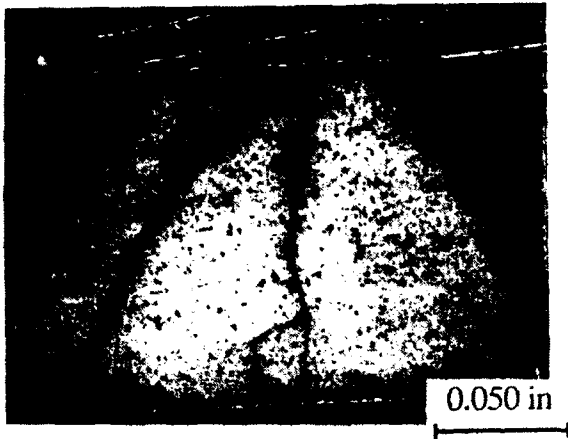
0.102 Inches Thick  
Copper Flyer Plate  
910 Ft/Sec



High Velocity

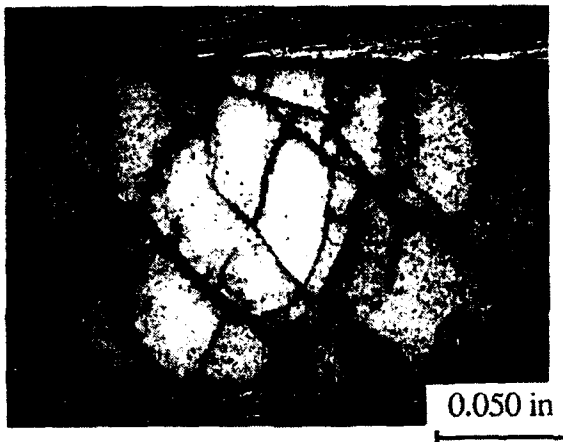
0.150 Inches Thick  
Copper Flyer Plate  
873 Ft/Sec

Figure 41. Damage in Impacted Plate vs, Load Duration



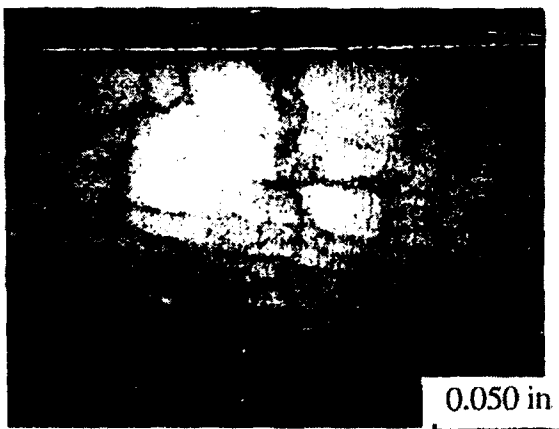
## Low Stress Pulse

Aluminum Flyer Plate  
0.052 Inches Thick  
998 Ft/Sec



## Intermediate Stress Pulse

Copper Flyer Plate  
0.052 Inches Thick  
834 Ft/Sec



## High Stress Pulse

Tungsten Flyer Plate  
0.100 Inches Thick  
891 Ft/Sec

Figure 42. Damage in Impacted Plate vs. Impactor Material

Table 11. Crack Surface Area and Fragment Data

Test No	Pulse Duration (Micro-seconds)	Compressive Stress (KSI)	Crack Surface Area per Unit Volume (In <sup>2</sup> /In <sup>3</sup> )	Cube Fragments per Cubic Inch
1	0.67	498	44.98	421
4	1.32	653	124.00	8827
5	1.93	626	200.00	37,037
7	0.67	680	234.00	59,320
8	0.50	438	48.89	541
9	1.26	855	274.00	95,235
10	0.67	598	165.24	20,888
13	0.67	808	270.00	91,125

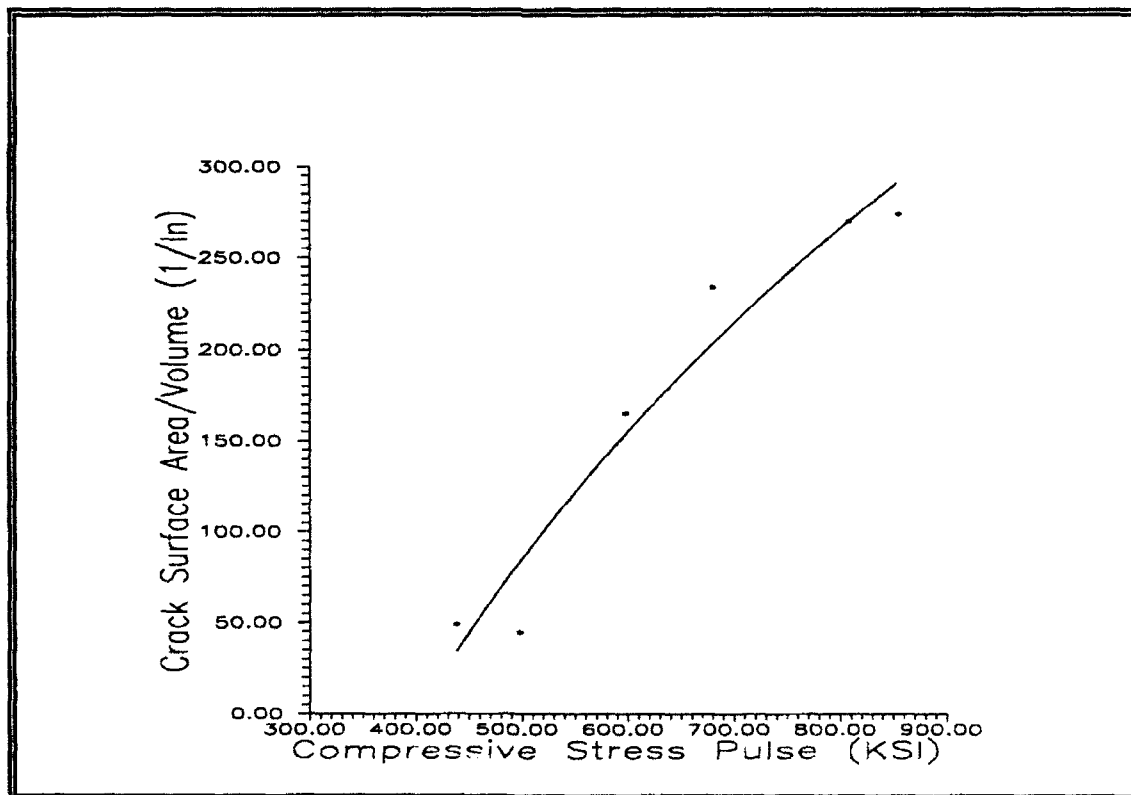


Figure 43. Crack Surface Area vs. Load Pulse Magnitude

Figure 43 summarizes damage in the ceramic as a function of load pulse magnitude while Figure 44 shows damage as a function of pulse duration. Load pulse magnitude was varied by varying velocity and varying impactor material. The test results indicated, based both on changes in velocity and changes in material, that damage increased with increasing load pulse magnitude. The relation between damage and duration of load was unclear with the limited data available. Damage was measured here as crack surface area per unit volume. The data were reduced using direct measurements of cracks with a planimeter, as well as by the method of intersections [68].

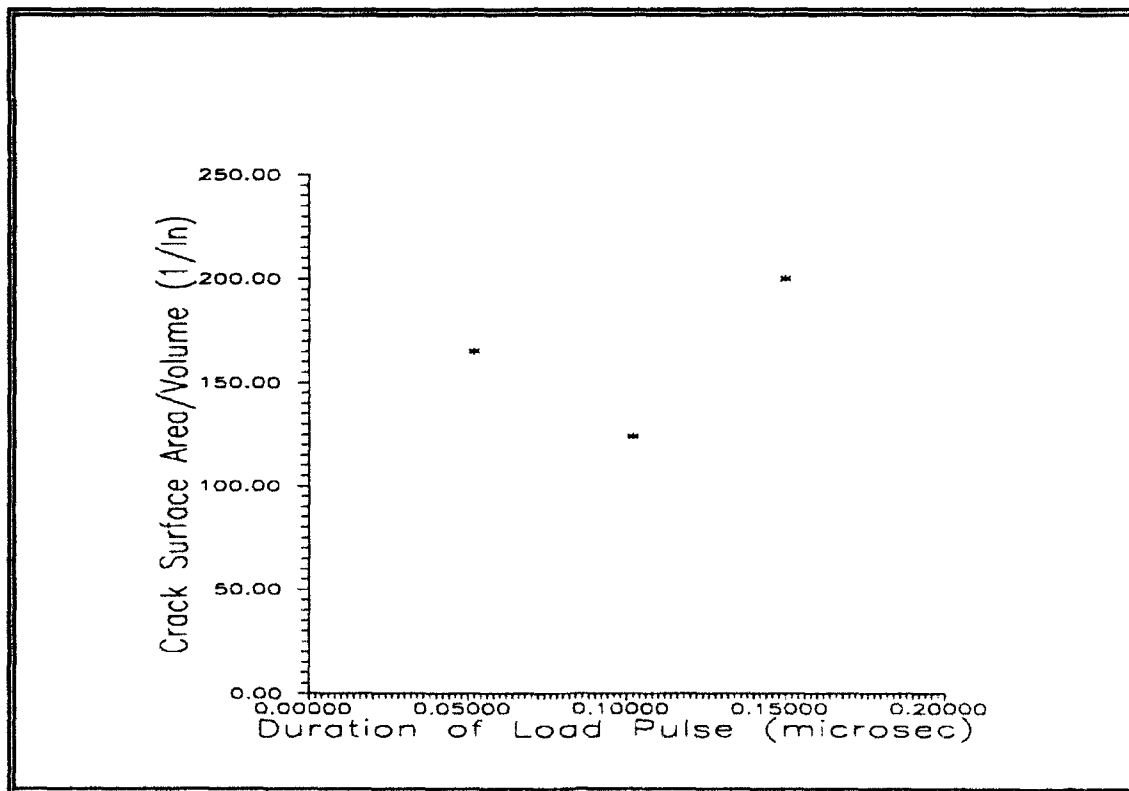


Figure 44. Crack Surface Area vs. Load Pulse Duration

CHAPTER 7  
PROPOSED FAILURE MODEL

Discussion

The objective of this research was to investigate the failure of alumina under impact loading and to develop a failure model, applicable in hydrocodes, to model penetration of confined ceramic. Originally, a microstatistically based failure model was planned. This was in anticipation of test results that were expected to demonstrate a pattern of damage in recovered ceramic specimens subjected to various loading conditions. The actual test results, as described in the previous chapter, did not provide a sufficient basis for a microstatistical model. In all cases where damage was observed, the damage progressed to complete failure or fragmentation, where failure is defined as the loss of load carrying capacity of the specimen, and fragmentation is particulation into a number of pieces. In no instance was the failure process stopped at successive levels of damage as would be necessary for the development of a Nucleation and Growth form of model.

The test results for the Hopkinson bar suggested that once failure is initiated, the failure process proceeded

rapidly to complete fracture. This is consistent with a model that relies on an instantaneous or nearly instantaneous criterion to initiate a fracture process which progresses to an outcome determined by the material state at the initiation of fracture. For the Hopkinson bar, the test results compared reasonably well with calculations using a Mohr-Coulomb surface as a failure criterion (equations 3-2a, 3-2b, and 3-2c.) Comparisons were even better when the Mohr-Coulomb failure surface was based on dynamic material properties (ie, the surface was adjusted based on a strain rate coefficient as developed in equation 5-1.)

Plate impact tests revealed post-test fragment distributions that correlated to applied stresses, and hence indirectly to strain rate. These results were consistent with a Grady-Kipp fragmentation model (equation 3-25.) The rod-on-rod impact tests provided a measure of the speed of propagation of the fracture process as discussed in Chapter 5. The rod-on-rod test results also showed that stresses had been achieved in recovered, apparently undamaged ceramic, which were far above those anticipated from an extrapolation of the dynamic strength capacity of the ceramic as measured in the Hopkinson bar. This would support the contention of Lankford [30], discussed in Chapter 3, that at high strain rates (here, above 1000 inches/inch/second) a change in fracture processes occurs. In the rod-on-rod tests, examination of the profile of the

deforming fragmented ceramic (as shown in Figure 31), also provided an indication of the post-fracture strength of the ceramic in the same way that the deformation profile of a metal rod impacting an anvil provides insight into the dynamic strength of metals in a classic Taylor rod impact test. Although complicated by the energy release associated with the fracture processes and the dynamic nature of the radial motion, a larger diameter was interpreted as an indication of a material with less post-fracture strength. The treatment of the post-fracture strength of the ceramic would appear to be one of the most important features of a ceramic model used for penetration modeling. The tests suggest that a yield surface similar to those used in soil mechanics would capture the mean-pressure-dependent strength characteristics of the fragmented ceramic.

#### Proposed Model

Based on the results observed in the Hopkinson bar and rod-on-rod impact tests, a fracture model is proposed that treats ceramic fracture differently at strain rates above and below a strain rate of 1000 inches/inch/second. The basic components of the model are outlined in Figure 45. Both above and below a strain rate of 1000 inches/inch/second, the material is treated as a linear-elastic material (utilizing von Mises equivalent stress and von Mises equivalent strain) until a strain rate dependent Mohr-Coulomb surface is reached. This criterion

is given by combining equations 3-2a, 3-2b, 3-2c, and 5-1 to give the strain rate adjusted Mohr-Coulomb criterion for the principal stresses  $\sigma_1$  and  $\sigma_3$  as:

$$\frac{\sigma_1}{\text{SIGMAT}\left(\frac{\dot{\epsilon}}{.001}\right)^{\text{EDOTCO}}} - \frac{\sigma_3}{\text{SIGMAC}\left(\frac{\dot{\epsilon}}{.001}\right)^{\text{EDOTCO}}} = 1 \quad (7-1)$$

where

*SIGMAT* = Uniaxial Tensile Strength

*SIGMAC* = Uniaxial Compressive Strength

*EDOTCO* = Strain Rate Coefficient

$\dot{\epsilon}$  = Equivalent Strain Rate (see equation 7-8)

For strain rates below 1000 inches/inch/second, fracture occurs immediately once this criterion is met. When fracturing occurs, the fragment density is predicted using the Grady-Kipp fragmentation model (based on elastic energy) derived in Chapter 3 and given in equation 3-26. This provides the predicted dimension,  $l$ , of a cubical fragment. Since the density of cubic fragments is then  $\frac{1}{l^3}$ , the fragment density, *FRAGCT*, is given by:

$$\text{FRAGCT} = \left( \frac{\rho \dot{\epsilon} c_0}{\sqrt{12} K_{1c}} \right)^2 \quad (7-2)$$

In the proposed model, once the ceramic fractures and a fragment density is determined, there are no provisions for further fragmentation. For the post-fractured material, the constitutive behavior of the pulverized ceramic is governed by a frictional material model, essentially a Drucker-Prager

model with the slope of the allowable stress boundary (as shown in the lower right of Figure 45) at a level between two limiting boundaries, each associated with a fragment size. For a given mean pressure, the maximum fragmented strength (*SIGMAX*) is described as:

$$SIGMAX = (PRESC2) P \quad (7-3)$$

and the minimum fragmented strength (*SIGMIN*) is described as:

$$SIGMIN = (PRESC1) P \quad (7-4)$$

where *P* is the pressure and *PRESC1* and *PRESC2* are model constants describing the slopes of the allowable stress boundaries for fragment densities *FGMIN* and *FGMAX*, respectively. This provides for less material strength in a finely pulverized ceramic than in a ceramic broken into large fragments.

The level of the flow stress between *SIGMIN* and *SIGMAX* is determined by the predicted fragment density, *FRAGCT*, based on a linear interpolation between a minimum fragment density, *FGMIN*, associated with ceramic rubble, and a maximum fragment density, *FGMAX*, associated with the fully pulverized ceramic strength. The flow stress,  $\sigma$ , is determined from the mean pressure through equations 7-3, 7-4, and the relations:

$$\sigma = \text{SIGMAX} \quad \text{for} \quad \text{FRAGCT} \leq \text{FGMIN} \quad (7-5a)$$

$$\sigma = \text{SIGMIN} \quad \text{for} \quad \text{FRAGCT} \geq \text{FGMAX} \quad (7-5b)$$

$$\sigma = \text{SIGMIN} + \left( \frac{\text{FRAGCT} - \text{FGMIN}}{\text{FGMAX} - \text{FGMIN}} \right) (\text{SIGMAX} - \text{SIGMIN}) \quad (7-5c)$$

$$\text{for} \quad \text{FGMIN} \leq \text{FRAGCT} \leq \text{FGMAX}$$

This is simply a linear interpolation of the flow stress from *SIGMAX* for fragment densities of *FGMIN* or smaller to *SIGMIN* for fragment densities of *FGMAX* or larger.

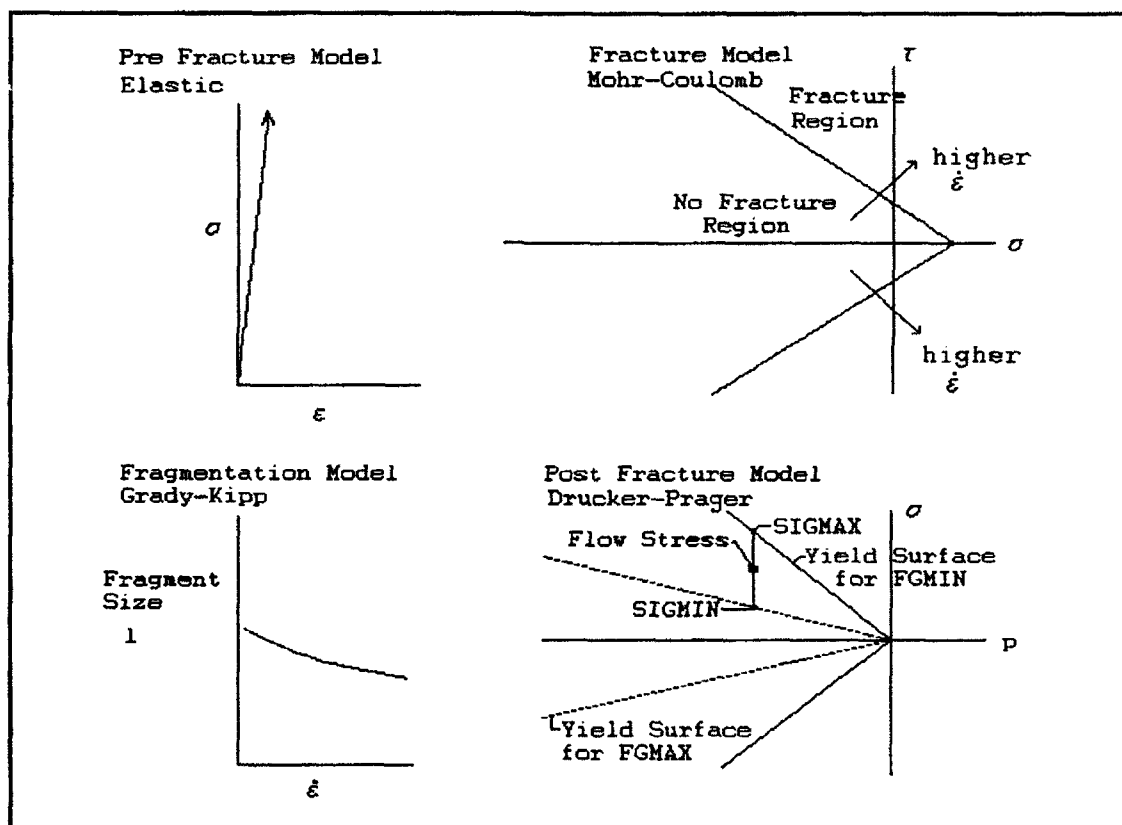


Figure 45. Proposed Failure Model

Figure 45 summarizes the model for strain rates less than 1000 inches/inch/second. Restating the description above

more briefly, the ceramic is elastic (upper left) until a strain rate dependent Mohr-Coulomb criterion is reached (upper right.) Based on the strain rate when the Mohr-Coulomb criterion is met, a fragment size is predicted using an elastic-energy-based Grady-Kipp fragmentation model (lower left.) The fragment density determines a maximum sustainable stress in a Drucker-Prager frictional material model (lower right.)

For strain rates above 1000 inches/inch/second, the model has essentially the same elements as described above, but the transformation to the post-fracture model is not immediate. For these ultra-high strain rates, when the Mohr-Coulomb criterion is reached, an internal damage phase is initiated, followed by an unstable macroscopic crack propagation (fracturing) phase. The presence of such phases was suggested by the rod-on-rod impact tests. The damage phase permits stresses that are higher than the Mohr-Coulomb criterion permits to be sustained in a macroscopically unfractured ceramic for short durations, under high pressures. The fracture phase provides a degradation of strength with crack growth rather than an immediate loss of strength, which was essential to match the measured stresses in the rod-on-rod tests.

Damage is measured as the sum of strain increments that occur while the strain rate dependent Mohr-Coulomb model indicates the ceramic should be fracturing. During the

damaging phase, the ceramic continues to load as an elastic material, without degradation of the elastic modulus. This assumed behavior would be consistent physically with microcracks requiring time to develop in the high pressure field associated with ultra-high strain rates. The amount of damage required before the fracturing phase begins is an accumulated equivalent strain increment (*FSTRN*) determined by:

$$FSTRN = \frac{P}{PSTRN} FAILE \quad \text{for } P < PSTRN \quad (7-6a)$$

$$FSTRN = 0 \quad \text{for } P < 0 \quad (7-6b)$$

$$FSTRN = FAILE \quad \text{for } P > PSTRN \quad (7-6c)$$

where *P* is the mean pressure and *PSTRN* is the mean pressure at which the failure strain increment *FAILE* is required. This is simply a linear interpolation of the required amount of damage from 0 at a pressure of 0 to a maximum of *FAILE* at pressures of *PSTRN* and above.

During the damage phase, an average equivalent strain rate is obtained. When the damage phase is complete, this average strain rate is used in equation 7-2 to provide a predicted fragment density. The predicted fragment density is used to provide a flow stress in the Drucker-Prager model in the same way described for lower strain rates. However, for strain rates above 1000 inches/inch/second (as determined by the strain rate when first reaching the

Mohr-Coulomb criterion, not the average strain rate during the damage phase), the flow stress is gradually decreased from the final stress in the damage phase to the flow stress of the Drucker-Prager model. The period of time over which the flow stress is adjusted is determined by a strain increment ( $FSTRN2$ ) associated with the macrocracking as opposed to the internal damage phase. (In the contour plots, the damage phase is not marked as failed, since during this phase the crack growth is assumed to be microscopic stable cracks. The plots show the material as failed during the fracturing phase, since the cracks are considered unstable at this point.) The strain increment required during the fracturing phase is expressed as:

$$FSTRN2 = \frac{P}{PSTRN} CRACKE \quad \text{for } P < PSTRN \quad (7-7a)$$

$$FSTRN2 = 0 \quad \text{for } P < 0 \quad (7-7b)$$

$$FSTRN2 = CRACKE \quad \text{for } P > PSTRN \quad (7-7c)$$

where  $CRACKE$  is the strain increment required for fracturing associated with a pressure  $PSTRN$ . This is simply a linear interpolation of the required amount of strain associated with the fracturing phase from 0 at a pressure of 0 to a maximum of  $CRACKE$  at pressures of  $PSTRN$  and above.

### Determination of Constants

The proposed model has eleven constants, including eight that needed to be determined from the test program. These constants were SIGMAT, SIGMAC, EDOTCO, PRESC1, PRESC2, FGMIN, FGMAX, FAILE, CRACKE, PSTRN, and K1C. The first two constants are the quasi-static tensile and compressive strengths of the ceramic, taken from the manufacturer's literature and validated for compression. EDOTCO was determined from the quasi-static compression tests and the Hopkinson bar tests as discussed in Chapter 5, equation 5-1. The remaining constants were determined through iterative calculations primarily of the rod-on-rod tests, and secondarily the Hopkinson bar tests and the plate impact tests. Details on the procedures for the iterative calculations are provided in the Appendix. In the case of constants PRESC1 and PRESC2, a range of reasonable values is presented because the experiments were not sensitive enough to distinguish within the range given. These two constants would be better determined through direct experiments measuring strength as a function of confining pressure for various fragment densities. For the values of FGMIN and FMAX, the same controlled tests would be helpful. The rod-on-rod tests have the advantage of providing the high strain rate loading conditions on as-fractured material, but the distinct disadvantage of minimal direct measurements and stress conditions not easily analyzed. FAILE and CRACKE are

related to PSTRN, and each of these constants was determined from calculational comparisons with the rod-on-rod tests. The value of PSTRN was determined by the maximum impact velocity used for the rod-on-rod test series. PSTRN essentially provides a cap on the amount of damage associated with the damage phase, and the amount of the strain increment associated with the fracture phase. Rod-on-rod experiments at higher velocities might raise the values of each of these constants. The value of K1C, the static fracture toughness, was taken from manufacturer's data.

Actual values for each constant are presented in Table 13 at the beginning of Chapter 8, along with constants required for all of the other models in the calculations.

#### Implementation

The proposed model was implemented in a version of the 1986 EPIC two-dimensional hydrocode. An additional FORTRAN subroutine of approximately 385 lines of coding was added and properly interfaced to the primary computational loop in EPIC. Except where specifically noted, the strain rate used throughout the ceramic failure model is an equivalent strain rate (based on a von Mises criterion) of the form:

$$\dot{\epsilon} = \sqrt{\frac{2}{9}((\dot{e}_x - \dot{e}_y)^2 + (\dot{e}_x - \dot{e}_z)^2 + (\dot{e}_y - \dot{e}_z)^2) + \frac{3}{2}(\dot{\gamma}_{xy}^2 + \dot{\gamma}_{xz}^2 + \dot{\gamma}_{yz}^2)} \quad (7-8)$$

where  $\dot{\epsilon}$  is a normal strain rate,  $\dot{\gamma}$  is a shear strain rate, and the subscripts refer to the axes of an orthogonal coordinate system.

#### Model Limitations

Table 12 provides a summary of the characteristics of the proposed model evaluated against a set of features that were viewed as potentially useful for the model. Several features important to the modeling of impact damage and fracture of ceramic were successfully included such as pressure effects, strain rate effects, fragment size prediction, strength degradation through a damage process, and suitability for use in hydrocodes.

The proposed model has a number of limitations. It is inherently empirical in nature. Dilatation of the ceramic on failure is only provided as a by-product of the assumption of a Prandtl-Reuss associated flow rule in the implementation of the model in the hydrocode, rather than the direct treatment of the material dilatancy. This flow rule is consistent with the von Mises criterion used as the basis for equivalent strain in equation 7-8 above, but inconsistent with the Drucker-Prager criterion. Fracture energy and fragmentation sizes are obtained by extending static fracture toughness values to dynamic conditions. Once fracture initiates in this model, the fragment size is

fixed and secondary fragmentation does not occur. The elastic modulus is not reduced in this model as micro-damage and fracture occur.

Although the model has limitations, it also offers certain advantages. It includes the pressure and strain rate dependencies of failure observed in the tests, and is easily implemented in hydrocodes. The primary features of the fracture process are believed to be present, and the structure of the model permits further refinement as specific knowledge of processes are obtained. For example, this model makes assumptions about the strength dependence on pressure for various ceramic particle sizes that require more development. The model represents a balanced level of assumptions in several areas, and should be useful as presented. Greater details in modeling accuracies are unlikely to benefit computational analysis specifically unless corresponding advances are made in treatments of material interfaces in hydrocodes. For example, during the development of this model, the desired level of analysis of several of the experiments was impossible because of noise generated in slide lines. Eulerian hydrocodes are often employed to eliminate the slide line problems, but they introduce problems with material diffusion. Advances in these areas need to parallel fracture model developments to allow hydrocodes to predict accurately the performance of ceramic materials used as thick, protective shields.

Table 12. Model Characteristics

Pressure Effects *	Treat Effects of Inclusions x
Time Dependence -	Surface Opening/Closure x
Strain Rate Effects *	Fragment Size Prediction *
Temperature Effects x	Strength Degradation *
Crack Direction x	Environmental Effects x
Crack Turning x	Track Damage *
Dilatancy -	Recognize Initial Material x
Physically Based -	State Through Readily Determined Material Properties
Extendible to Micromechanics -	Suitable for Implementation *
Crack Tip Plasticity x	in Continuum Mechanics Codes
Treat Pore Collapse x	Cell Size Independence -
* Proposed Model Treats	
- Proposed Model Treats only Partially	
x Not Considered in Proposed Model	

CHAPTER 8  
COMPUTATIONAL PROGRAM

Model Implementation in EPIC-2 Hydrocode

Several failure models were implemented in the EPIC-2 hydrocode as part of this research to observe their behavior under conditions such as the rod-on-rod impact experiments, plate impact experiments, and rod penetration of a confined ceramic armor plate. In all cases the ceramic was assumed to behave as a linear elastic material until the onset of failure. The following failure models were considered:

- (1) Maximum stress criterion
- (2) Mohr-Coulomb model
- (3) Mohr-Coulomb model with strain rate effect
- (4) Proposed Model (Mohr-Coulomb failure activation surface, a plastic strain damage criterion, a Grady type fragmentation model, and a pressure dependent yield surface for the fragmented ceramic determined by size of particulated ceramic)

For the first three failure surfaces, after failure occurred, the strength of the ceramic was assumed to be either perfectly plastic at the strength where failure occurred or it was assumed to be without strength. Both extremes were considered for each failure surface for each computational configuration. The assumption of total loss of strength capacity was inconsistent with the rod-on-rod impact test results and the residual strength assumption was

inconsistent with the Hopkinson Bar simulation. The Mohr-Coulomb model was consistently superior to the maximum stress criterion, and the strain rate dependent Mohr-Coulomb model compared more favorably with the experimental results than the simple Mohr-Coulomb model. The proposed model achieved slightly better results than the other Mohr-Coulomb-based models, and much better results than a maximum stress criterion. The material properties used by the models are described in Table 13. Strength data were as described in Chapter 3 from the manufacturer's data for static data, with dynamic data supplemented through this program. The data for the Mie-Gruneisen equation of state were determined from the known density ( $\rho_0$ ), bulk wave speed ( $c_0$ ), Gruneisen coefficient ( $\Gamma$ ), and shock Hugoniot ( $s$ ) from [38] using the relations given by a Sandia Laboratory equation of state reference [69]. The equation of state coefficients as used in EPIC are in the form:

$$P = K_1\mu + K_2\mu^2 + K_3\mu^3 \quad (8-1)$$

where the constants are determined from:

$$K_1 = \rho_0 c_0^2 \quad (8-2)$$

$$K_2 = K_1 \left( 1 + 2(s-1) - \frac{\Gamma}{2} \right) \quad (8-3)$$

$$K_3 = K_1 \left( (2-\Gamma)(s-1) + 3(s-1)^2 - \frac{\Gamma}{2} \right) \quad (8-4)$$

$$\mu = \left( \frac{\rho}{\rho_0} - 1 \right) \quad (8-5)$$

Table 13. Data Used in Computational Models

Property	EPIC name	Units	Value
Density		LBM/IN <sup>3</sup>	.000318
Specific Heat		IN-LBF/LBM*F	792222.4
Conductivity		LBF/SEC*F	0
Vol Coef Thermal Exp	ALPHA	1/*F	.000009
Initial Temp	TEMP1	*F	70
Room Temp	TROOM	*F	70
Melt Temp	TMELT	*F	9999
Shear Modulus		LBF/IN <sup>2</sup>	14000000
Coefficients for Johnson-Cook Constitutive Model	C1	LBF/IN <sup>2</sup>	99999999
	C2	LBF/IN <sup>2</sup>	0
	N	-	1
	C3	-	0
	M	-	0
	C4	-	0
	SMAX	LBF/IN <sup>2</sup>	0
Coefficients for Mie-Gruneisen Equation of State	K1	LBF/IN <sup>2</sup>	21670000
	K2	LBF/IN <sup>2</sup>	8235000
	K3	LBF/IN <sup>2</sup>	-10520000
	GAMMA	-	.76
Linear Artif Viscosity	CL	-	.2
Quad Artif Viscosity	CQ	-	.4
Max Hydrostatic Tension	PMIN	LBF/IN <sup>2</sup>	10000000
Hourglass Viscosity Coef	CH	-	.02
Coefficients for Johnson-Cook Fracture Model	D1	IN/IN	.0000125
	D2	IN/IN	0
	D3	-	0
	D4	-	0
	D5	-	0
Tensile Spall Stress	SPALL	LBF/IN <sup>2</sup>	22000
Min Fracture Strain	EFMIN	IN/IN	.0006875
Coefficients for the Mohr-Coulomb Model	SIGMAT	LBF/IN <sup>2</sup>	22000
	SIGMAC	LBF/IN <sup>2</sup>	280000
Additional Coefficients for the Proposed Ceramic Failure Model	EDOTCO		0.037
	PRESC1		0.5-1.0
	PRESC2		1.0-2.0
	FGMIN	1/IN <sup>3</sup>	10
	FGMAX	1/IN <sup>3</sup>	5000
	FAILE	IN/IN	0.011
	CRACKE	IN/IN	0.011
	PSTRN	LBF/IN <sup>2</sup>	140000
	K1C	LBF-IN <sup>1/2</sup> /IN <sup>2</sup>	2730

Summary of Calculations

The calculations and their related experiments are summarized in Table 14. The approach taken in developing and validating the ceramic fracture model in this work was unique to the extent that several different loading conditions were considered in a combined experimental and computational program. The model was not specifically adjusted to fit any single loading condition or particular geometry. As a result, the model developed did not display the same extent of comparability to experimental results that other models have shown. The best set of constants for one loading condition were frequently at odds with the best constants for another. For example, in order to achieve an accurate prediction of the stress levels observed in the rod-on-rod impact tests, a delay in the failure process was necessary in the model. This delay was consistent with the fracture pattern observed photographically in the experiments. In contrast, the best predictions of fracture in the Hopkinson bar experiments were obtained when no time delay was used. Also, the Hopkinson bar calculations compared best with experimental results when the post fractured material retained significant strength, but the comparisons to the photographic results for the rod on rod experiments were best with lower levels of post fractured material strength. As a result of these and other contradictory indicators, the model was employed with

Table 14. Summary of Calculations

Calculation	Description	Experiment Number	Figure for Calculation	Figure for Experiment
1	Hopkinson Bar, before Failure	HPB 18/19	50-51	16-19
2	Hopkinson Bar, Strain Rate Effect, $\dot{\epsilon}=600$	HPB 1-5	49	
3	Hopkinson Bar, Strain Rate Effect, $\dot{\epsilon}=800$	HPB 6-9	49	20
4	Hopkinson Bar, Proposed Model with Failure	HPB 1-5	49	
5	Rod-on-rod, Proposed Model, Modest Failure	Rod 6	66	32
6	Rod-on-rod, Proposed Model, as Photographed	Rod 14	62	31
7	Rod-on-rod, Proposed Model, Extensive Failure	Rod 22	64,65	33,62
8	Plate Impact, Proposed Model, Low Velocity	Plate 1		
9	Plate Impact, Proposed Model, Medium Velocity	Plate 10		
10	Plate Impact, Proposed Model, High Velocity	Plate 13		
11	Penetration, Mohr-Coulomb Model, Fine Zones	Pen 3	1	
12	Penetration, Proposed Model, Coarse Zones	Pen 3		
13	Penetration, Proposed Model, Fine Zones	Pen 3		

parameters fixed on the basis of the most direct measurements possible, without adjustments to fine tune the model to other tests.

The differences in the calculational predictions and the test results may represent the limitations of the phenomenological approach of the model, supporting the requirements suggested in Chapter 1 for more detailed micromechanical treatments to treat thoroughly a wide range of applications (loading conditions.) Nevertheless, even with the inadequacies of the proposed model, considering other computational limitations, it represents a useful treatment for prediction the response of ceramics to impact and penetration. Details of the calculations for each of the experimental configurations are discussed below.

#### Hopkinson Bar Analysis

##### Computational Model

Figure 46 shows the calculational model employed to study the response of AD85 under loading in a Hopkinson Bar. Because of the time and cost of running a complete simulation of the entire Hopkinson Bar, only a very small section was considered. A 10-inch section of the striker bar was modeled, with a one-inch-long incident bar, a Coors AD85 specimen and the Coors AD99 alumina disks used to protect the ends of the incident and transmitter bars, and a ten-inch transmitter bar. This differed significantly in length from the actual test apparatus for reasons of

computational efficiency. Initial velocity values based on measured striker bar velocities in tests were assigned to the incident bar. This two-dimensional model permits radial velocities to develop at interfaces, such as between the striker bar and the incident bar, but since slide lines were not used, it constrains each side of the interface to have equal radial velocities. Although this interface condition was acceptable between the striker bar and the incident bar, which were of the same material and diameters, it represented a compromise at the other interfaces. The locked interfaces were used because, for low velocity, elastic impacts, the slide line in EPIC-2 generated excessive noise. The setup used a total of 5831 nodes and 11220 elements without sliding surfaces between the incident bar, the input disk, the specimen, the output disk, and the transmitter bar.

Four calculations were performed for the Hopkinson bar analysis. The first calculation, corresponding to Hopkinson bar test 19, was performed to observe the stress field in the test specimen where failure was barely achieved, demonstrating the degree of uniformity achieved in the stress field of the specimen during the early stages of loading. As shown in Figure 47, the von Mises equivalent stress field rapidly reached a uniform configuration except in cones near the ends. The stress state in the center of the specimen was examined and determined to be uniaxial

stress. This calculation also validated the computational setup. Original computational configurations with slide lines at each end of the specimen were discarded due to computational noise from the slide lines. All calculations fixed the specimen to the loading disks, providing a degree of radial constraint that was not present in the testing. The effect of this total friction between the bar and the specimen was much less harmful than the slide line noise. The axial stresses were compared to the radial, circumferential, and shear stresses at each of the 10 stations shown in Figure 46 for the loading conditions of test 1. Stresses are plotted versus time for Stations A, B, C, and D in Figure 48. At stations D, E, F, and H the radial, circumferential, and shear stresses were under one percent of the axial stress. The stress-time histories at stations A and I, B and J, C and G, and D and H were generally symmetric. Stations A and I showed circumferential and radial stresses 22.5 percent of the axial stress and shear stresses 7.2 percent of the axial stress. At stations B and J, circumferential stresses were 16.1 percent, radial stresses were 5.5 percent, and shear stresses were 11.3 percent. At stations C and G, circumferential and radial stresses were 4.3 percent and shear stresses were 1.9 percent.

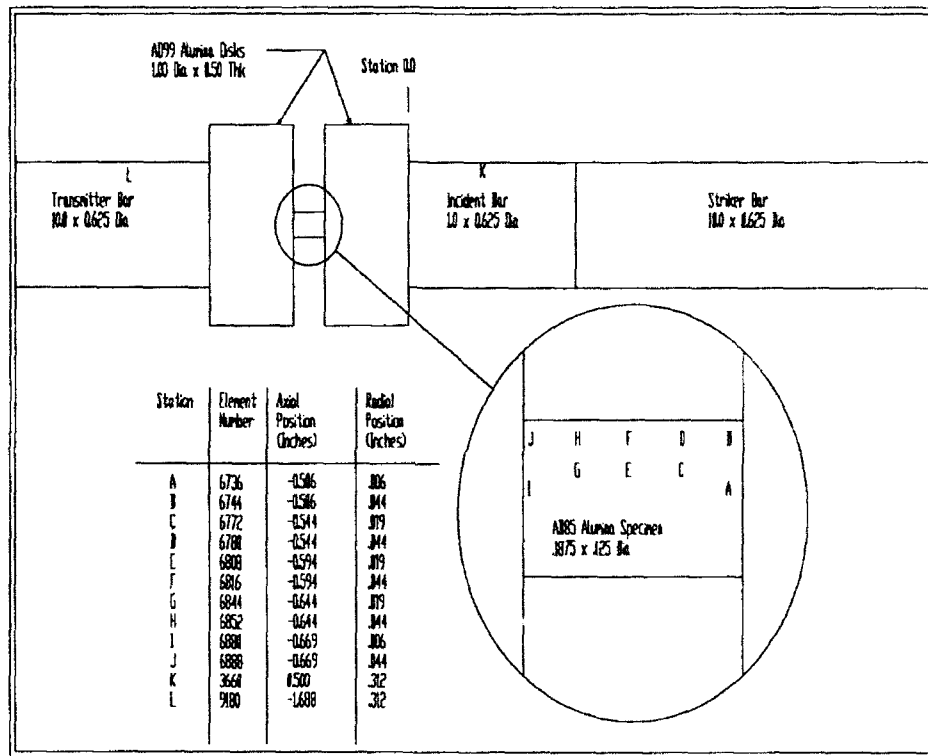


Figure 46. Hopkinson Bar Calculational Configuration

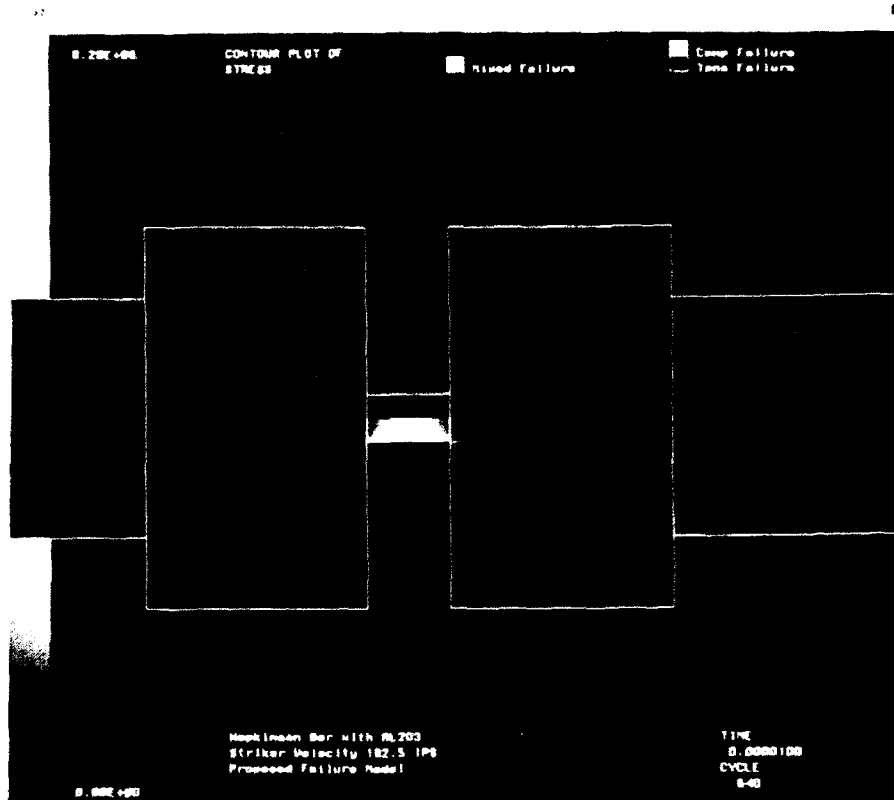


Figure 47. Stress Field in Specimen at 4 microseconds

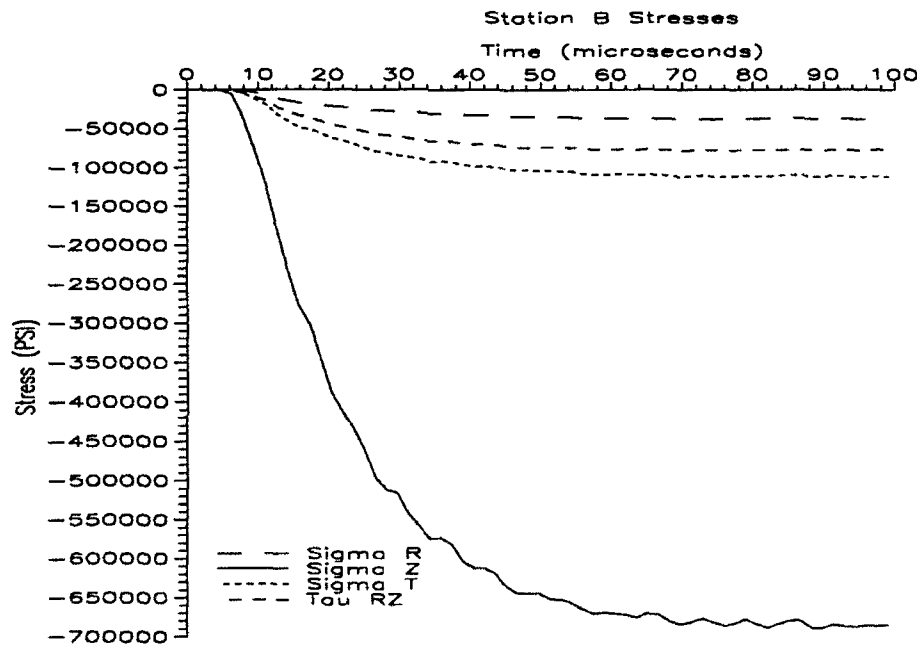
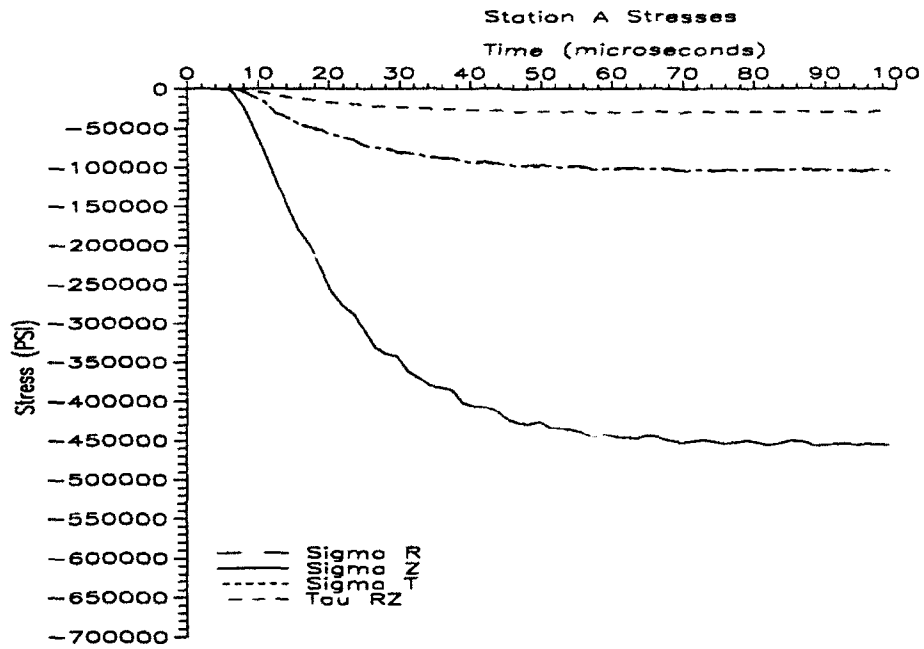


Figure 48. Stress versus Time at Stations A and B in Test 1



Two calculations were performed to examine the Hopkinson bar test under different strain rates. These are discussed in the next section.

#### Strain Rate Effect

Figure 49 presents the stress contours at the same time for calculations of Hopkinson Bar experiments performed at two different strain rates. In these calculations, presented in Figures 49-52, the ceramic was treated as an elastic material and the failure model was not used. The more rapid loading of the higher strain rate test is evident, and the stress field is uniform in both cases. Figures 50 and 51 show axial stress and strain rate histories respectively for Station E in the two calculations. Figure 52 shows the ratio of the magnitudes of the mean pressure to axial stress for the same element in the two different strain rate tests. In both cases, the stability of the ratios at  $1/3$  indicates that uniaxial stress conditions are consistently maintained. Similar results were obtained for elements C, F, and G. The conclusion reached from analyzing these and other plots from the Hopkinson bar calculations is that an approximately uniform uniaxial stress state is rapidly reached in the specimen except near the interfaces, and the increased strength at high strain rates is related to the strain rate, not to variations in the stress field.

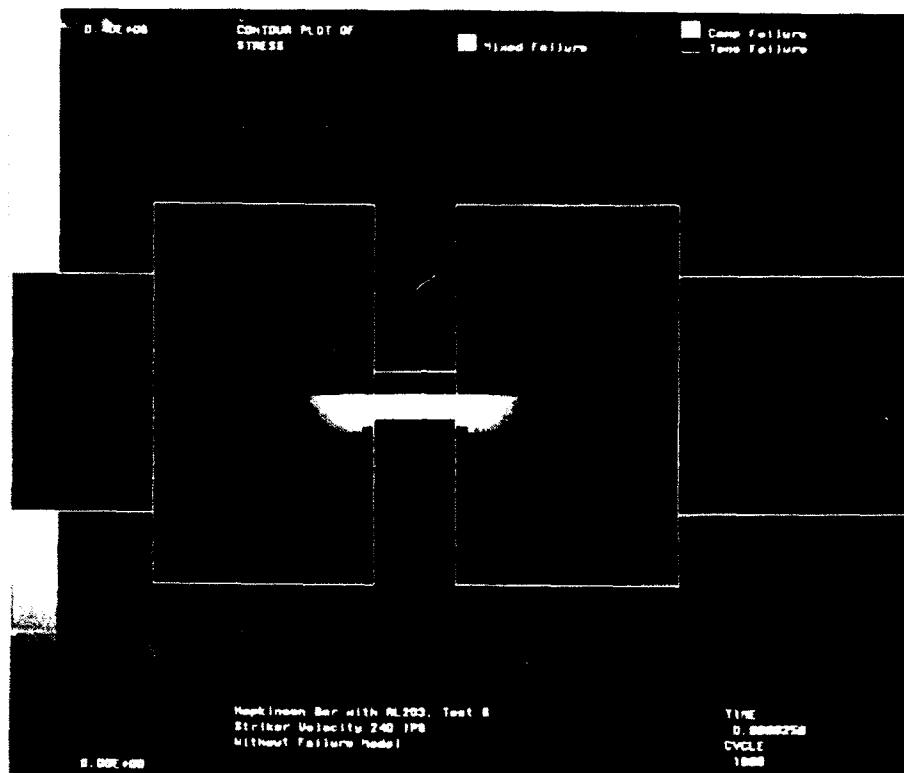


Figure 49. Hopkinson Bar Calculation, Test 6,  
Stress Field for a Strain Rate of  $600 \text{ sec}^{-1}$

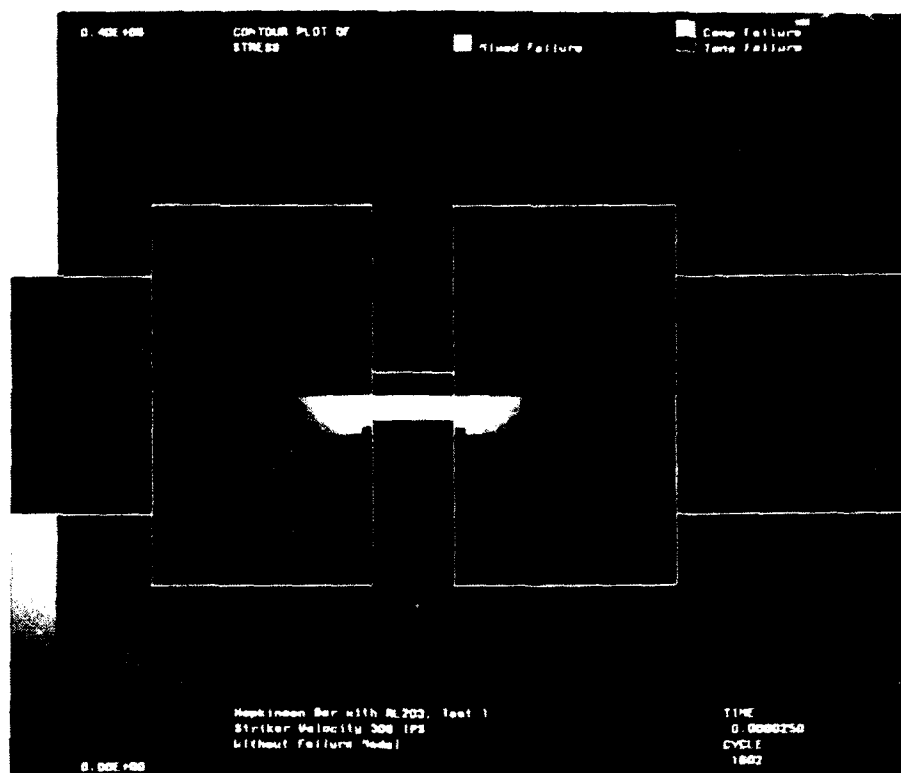


Figure 49. Hopkinson Bar Calculation, Test 1, Stress Field for a Strain Rate of  $800 \text{ sec}^{-1}$  (Concluded)

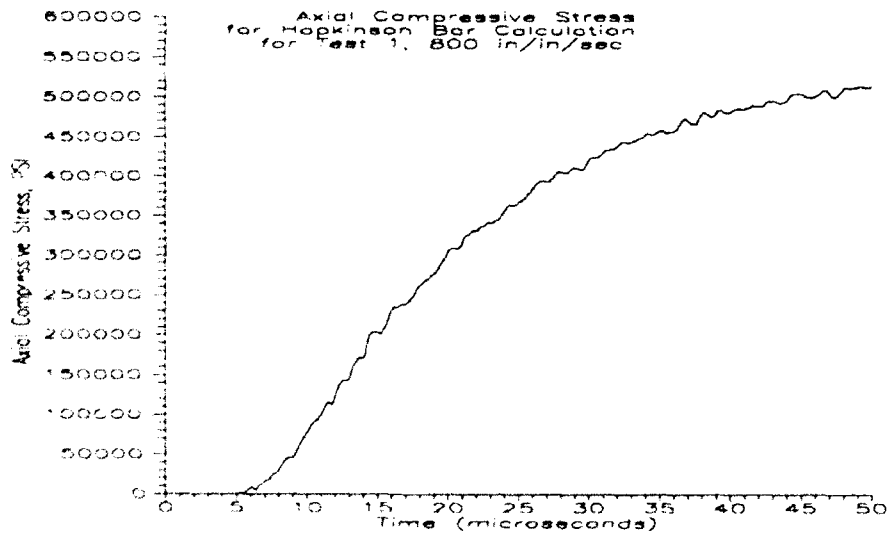
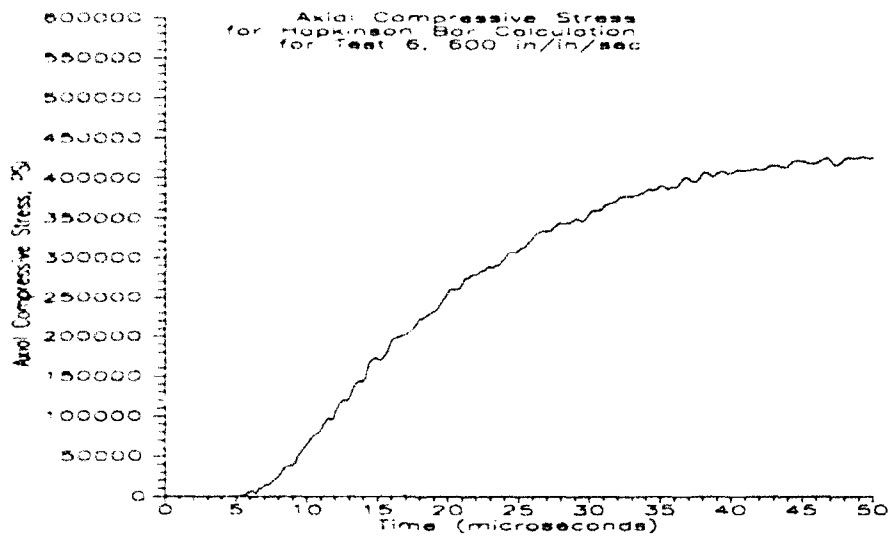


Figure 50. Stress Histories at Station E

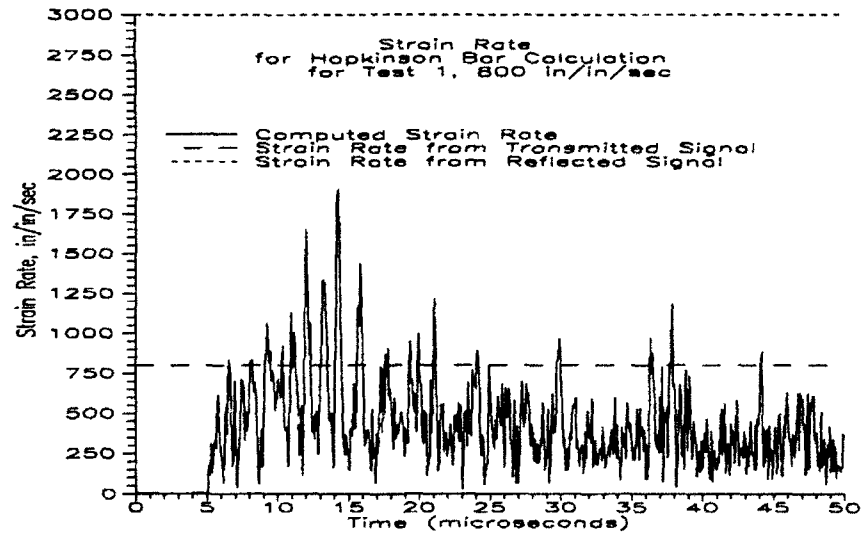
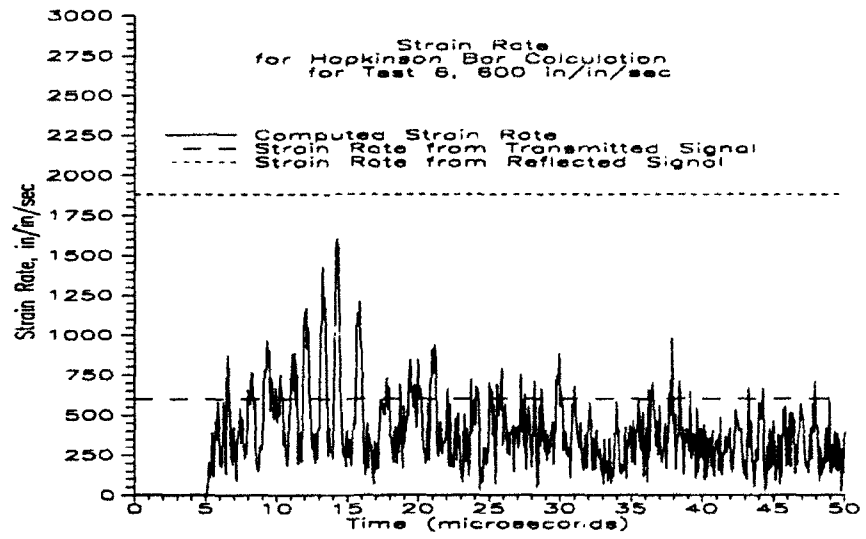


Figure 51. Strain Rate Histories at Station E

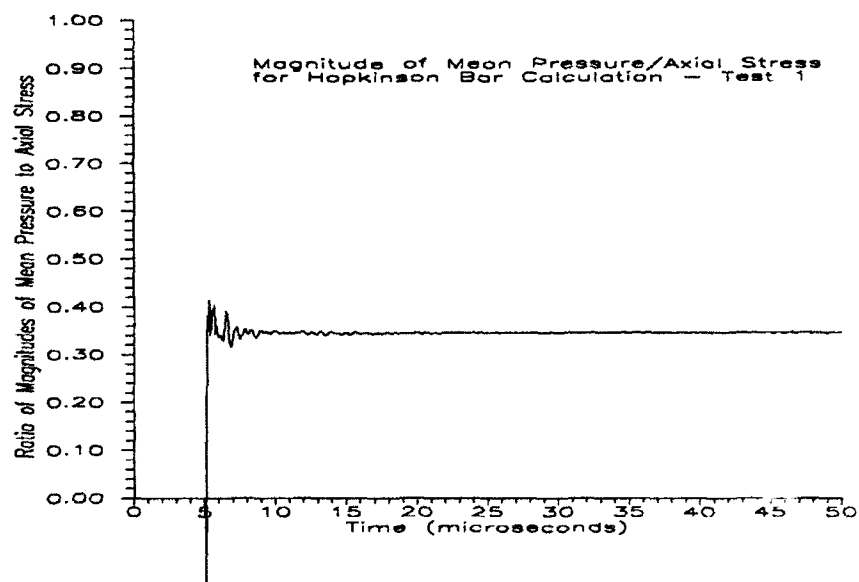
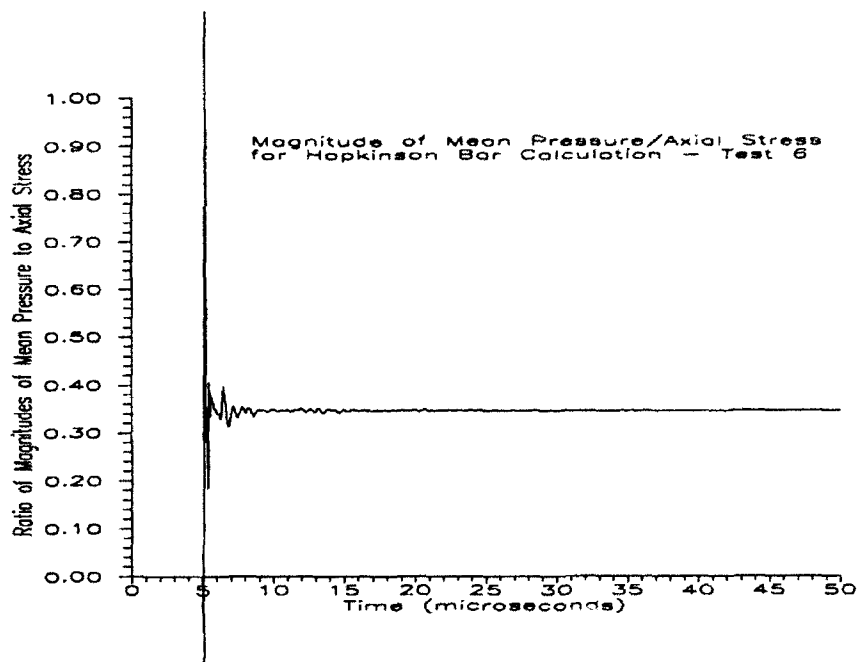


Figure 52. (Mean Pressure/Axial Stress) Histories for Station E

### Fracture Predictions

A fourth Hopkinson bar calculation was performed to observe fracture predictions of the proposed failure model relative to the strength signals observed in a test that achieved complete ceramic failure. Figure 53 shows the calculated transmitted stress profile for this test. The peak is consistent with experimental results, and the dwell at the peak stress level is consistent with some test results, while others have indicated a more rapid loss of strength. Figure 54 shows the failure sequence at five times with the ceramic specimen in the Hopkinson bar. Notable is the conical shaped stress contour at the ends of the specimen-- a shape consistent with the fragments recovered from several tests, and visible in Figure 22. The predicted failure occurs from the center of the specimen, where the stress is most uniform, not near the interfaces where the previously noted nonuniformity occurs. The proposed failure model predicted a range of fragment sizes in general agreement with the experimental observations.

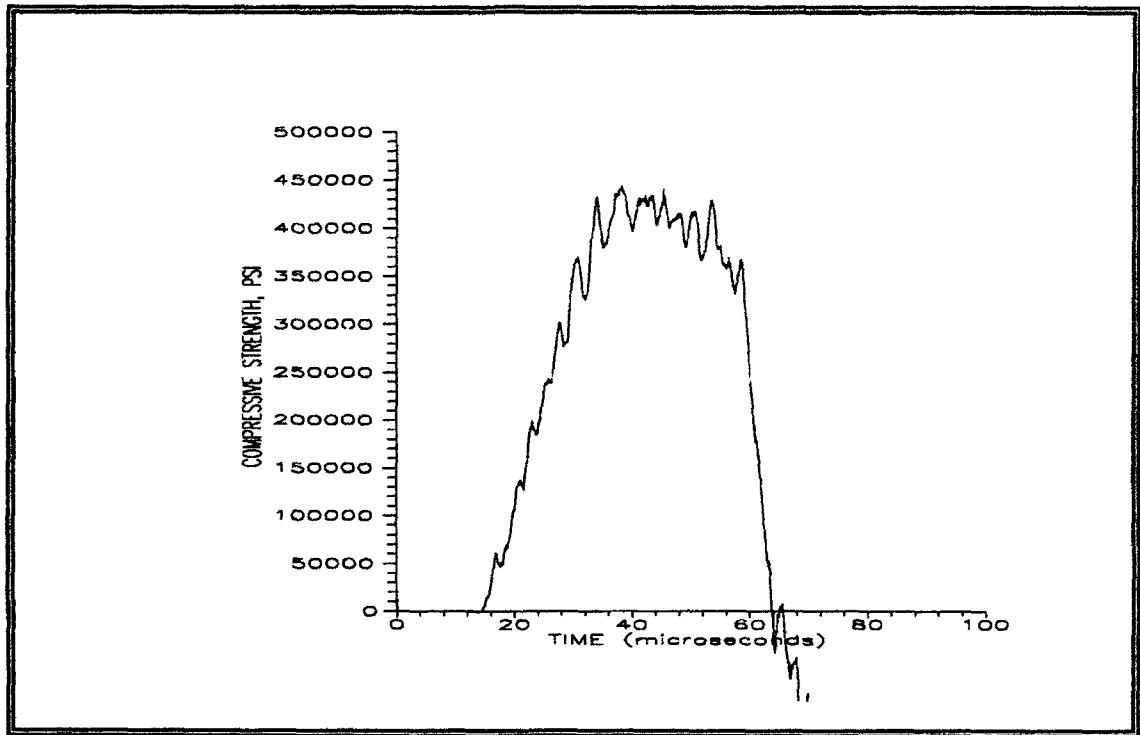
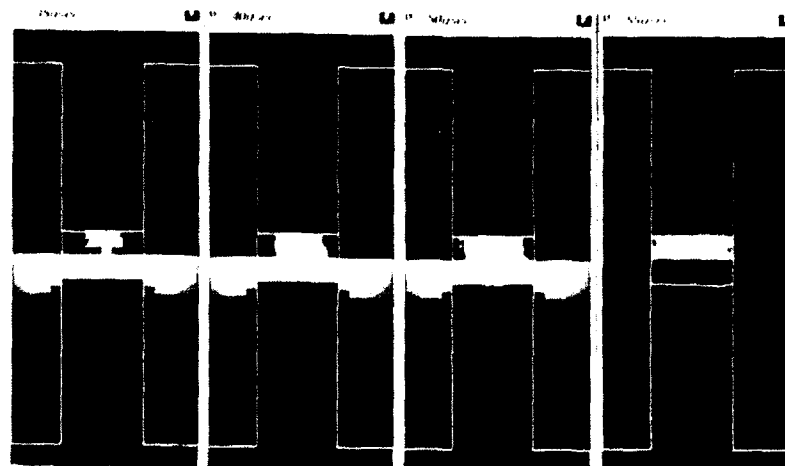


Figure 53. Transmitted Stress - Hopkinson Bar Calculation, Test 1



(A)



(B)

Figure 54. Failure Contours in Split Hopkinson Bar

## Plate Impact Analysis

### Computational Model

Figure 55 shows the calculational model employed to study the response of AD85 under plate impact loading. The setup used a total of 4458 nodes and 4318 elements without sliding surfaces. Although slide lines between components would have permitted separation to isolate the return of reflected waves from surfaces at late times, preliminary calculations with slide lines showed that the surface interfaces generated arbitrary computational stress transients that seriously interfered with interpretation of the failure model's behavior.

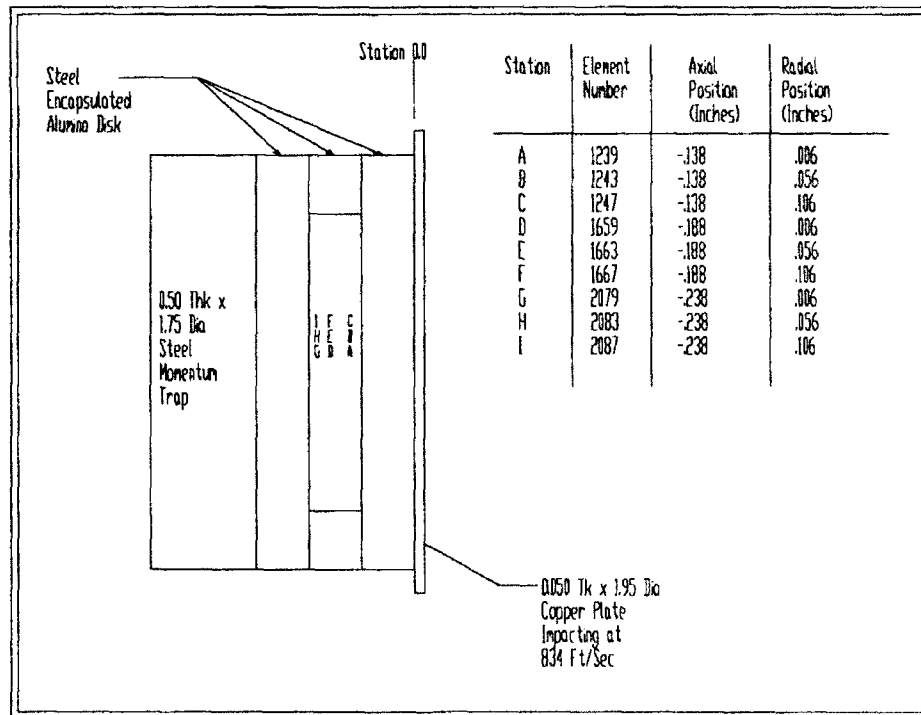
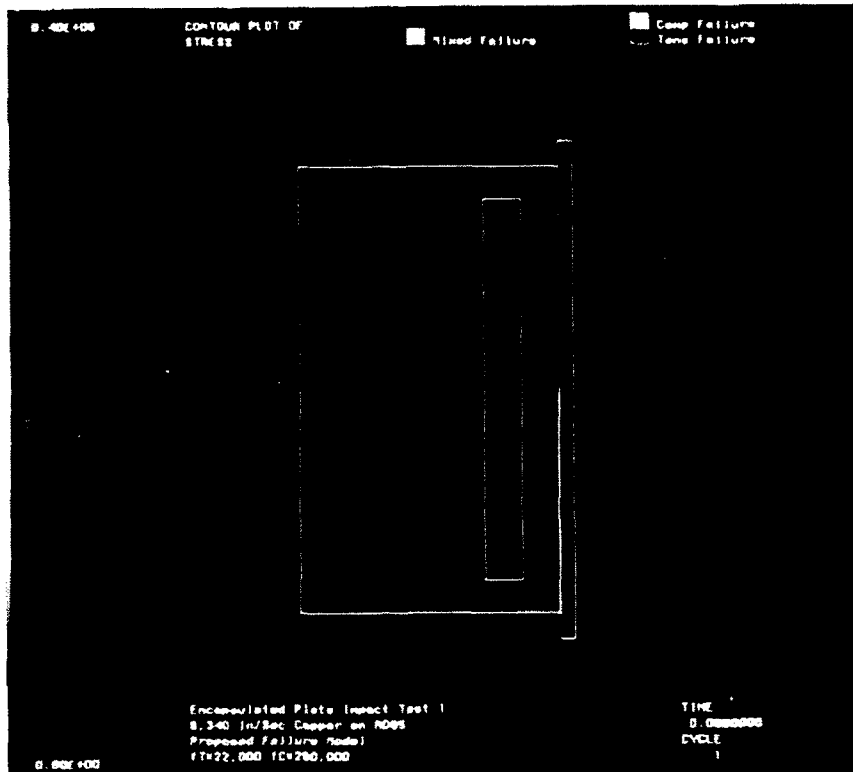


Figure 55. Plate Impact Computational Configuration

### Fracture Predictions

Figure 56 provides a sequence of snapshots of stress profiles in the calculation of plate impact test 1. Although the plate impact tests were designed as carefully as possible to generate data on ceramic fracture under compression, the calculations for all tests indicated that reflected tensile stresses were in fact largely responsible for failure. As Figure 56 shows, the fracture generally proceeds inward from the outer diameter. The failure mode flags generally indicate fracture occurring under principal stresses of mixed signs, but by studying the relative magnitudes of the first and third principal stresses at fracture initiation, the importance of the first principal stress was noted. Figure 57 shows the history for strain rate, pressure, and axial stress for Station E in the impacted ceramic plate. Here, as in all cases where hydrocode results are discussed, the mean pressure is one-third the sum of the principal stresses, and stresses are determined without assumptions about uniaxial stress or strain conditions. Values were consistent with expectations. The predicted fragment sizes in the central region are compared to the experimental results in Figure 58. The fragment size predictions of the model were close to the observed test results without adjustment to the model parameters.



(A)



(B)

Figure 56. Contours of Stress for Plate Impact Test 1

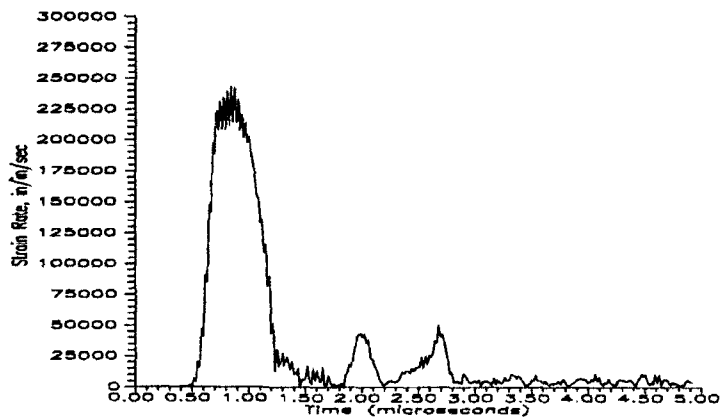
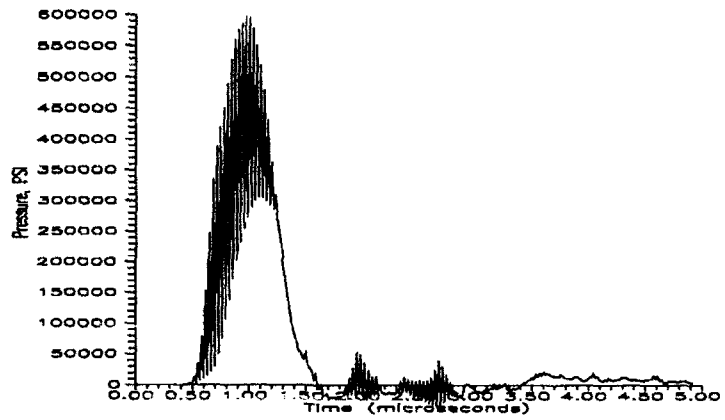
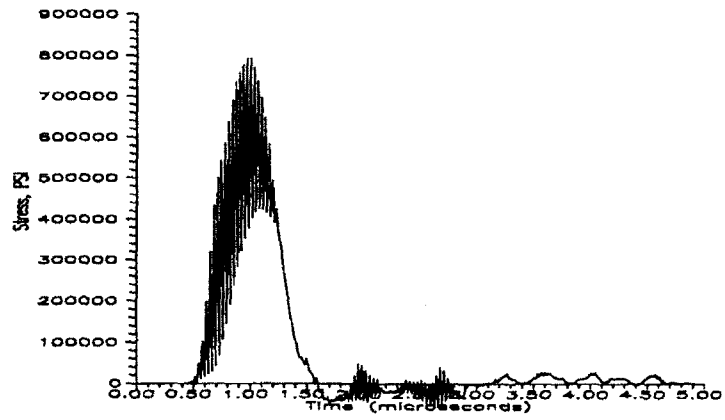


Figure 57. Time History for Element in Plate - Strain Rate, Pressure, and Axial Stress for Station E

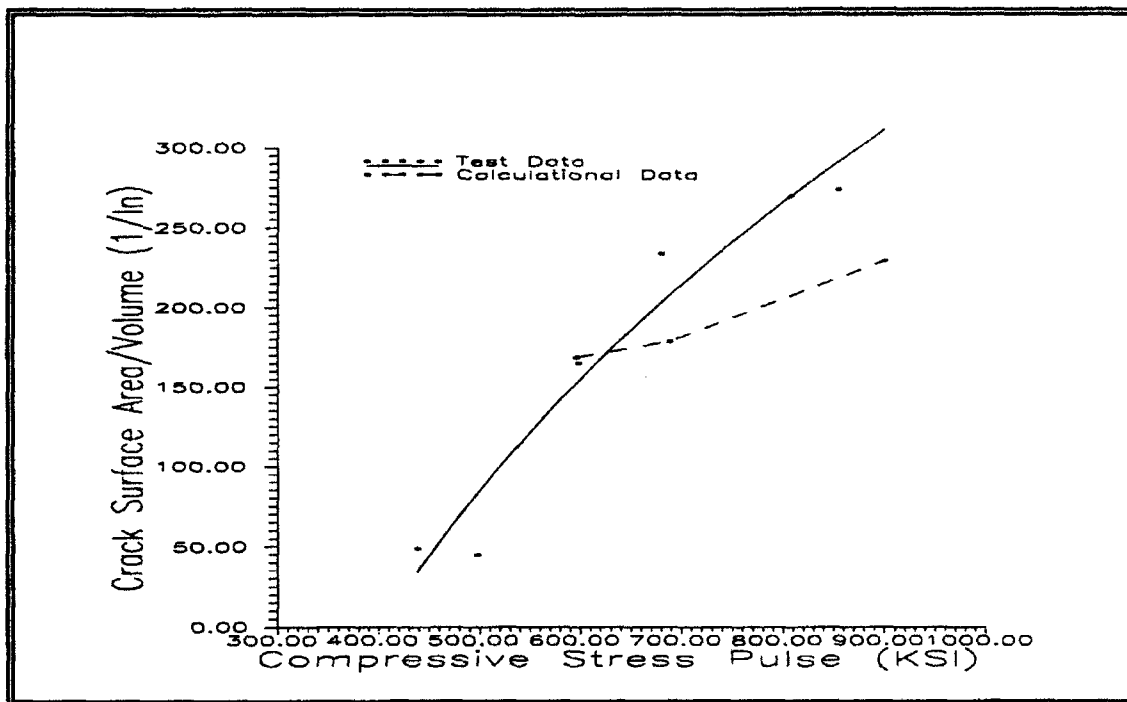


Figure 58. Calculated vs. Experimental Fragment Sizes

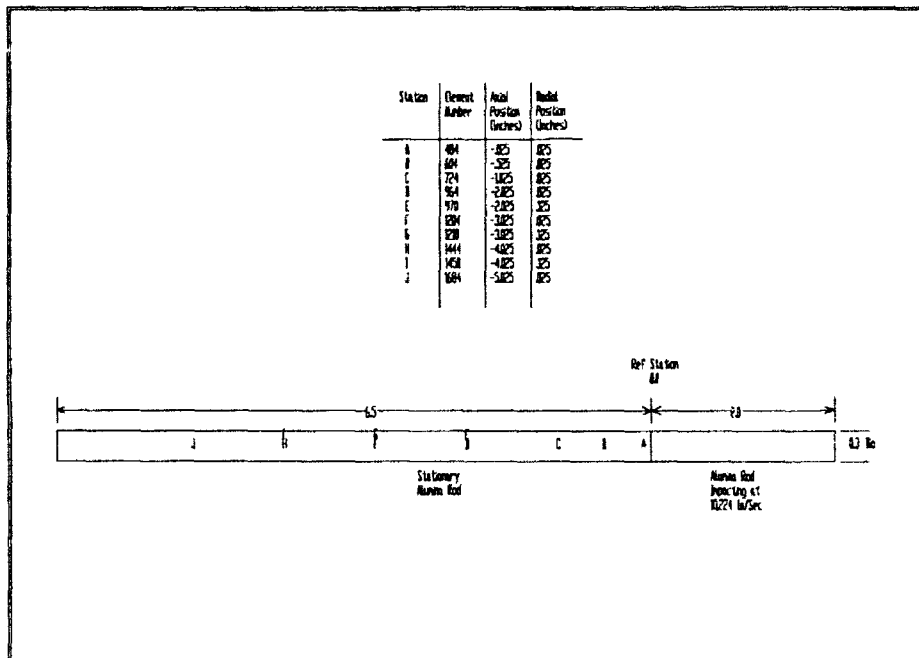


Figure 59. Rod-on-Rod Calculation, Test 14

## Rod-on-rod Impact Analysis

### Computational Model

Figure 59 shows the calculational model employed to study the response of AD85 rods impacting under symmetrical conditions where the rods were photographed during impact, and a momentum trap was used to minimize motion of the target rod. Figures 60 and 61 show similar calculations for two different impact conditions where the rods were recovered and stresses were measured with embedded stress gages. The setups used a total of 1194, 844, and 708 nodes and 2040, 1440, and 1200 elements respectively. Because of symmetry at the impact point, no sliding interface was necessary.

### Fracture Predictions

Figure 62 shows the time sequence of calculations of test 14, which compares directly to the experimentally obtained photographs from Figure 31. The fracture flags in the top half of each part of Figure 62 are similar to those in Figure 56 (and all other hydrocode generated contour plots.) The correlation of the growth in the fracture zone is good. Mixed-mode fracture begins at the interface of the two rods, as seen at 2 microseconds in Figure 62, where it extends from the lateral surface to the centerline, and then spreads along the centerline. (The top half indicates the fracture modes and the bottom equivalent stress; the calculation is axisymmetric). The profile of the fracture zone is an

indication of post fracture strength in the pulverized material, and the time evolution of the profiles also compares favorably. By 4 microseconds, the beginning of radial growth of the impact ends of the rods is obvious in both the experiment (Figure 31), and the calculation (Figure 62.) Transverse cracks that probably are due primarily to tensile reflections from the end of the rod were reproduced as mixed mode failures. Figure 63 shows the sectioned and polished cross-section of a recovered target rod at a position 1 inch from the impact point in test 22. The axial cracking in this recovered specimen matches the geometry predicted for the fracture zone from the calculation of test 22 as shown in Figure 64. The photograph is oriented opposite the calculation, with the end that was toward the impact point on the left. The height of the photograph represents the entire rod diameter, and the left side corresponds to a position 6.6 diameters from the right end of the impacting rod shown in the calculation. Figure 65 shows the calculated axial stress histories at the Manganin gage locations in test 22. Experimental histories are shown in Figure 33. Correlation was good. The measured levels of the stresses in the tests were extremely high relative to the load capacity of the ceramic, even extrapolated to the high strain rates seen here. Figure 66 shows the calculated axial stress histories corresponding to test 6 as shown in Figure 32. Again, correlation was good.

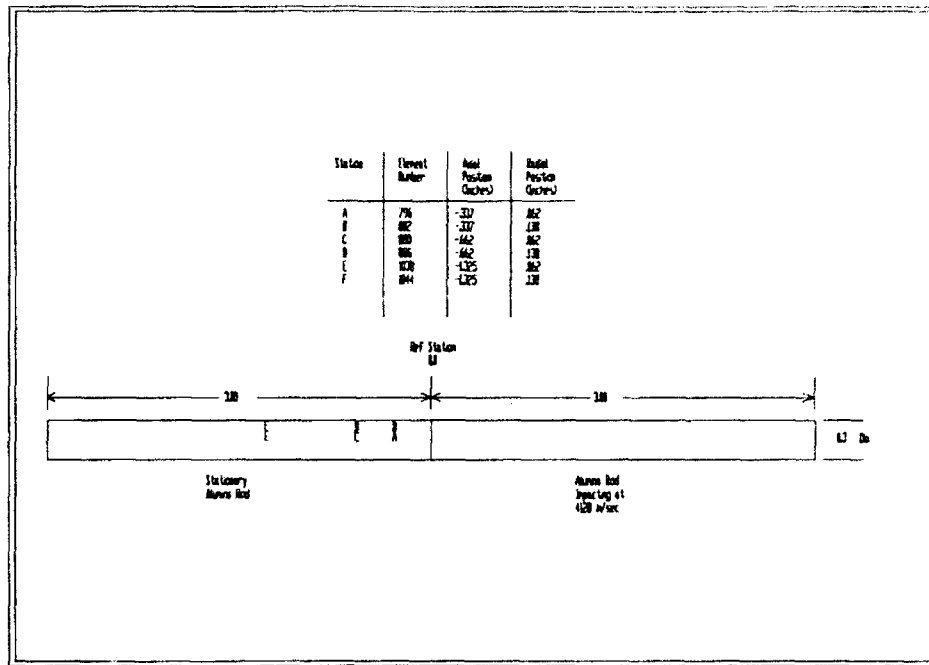


Figure 60. Rod-on-Rod Calculation, Test 6

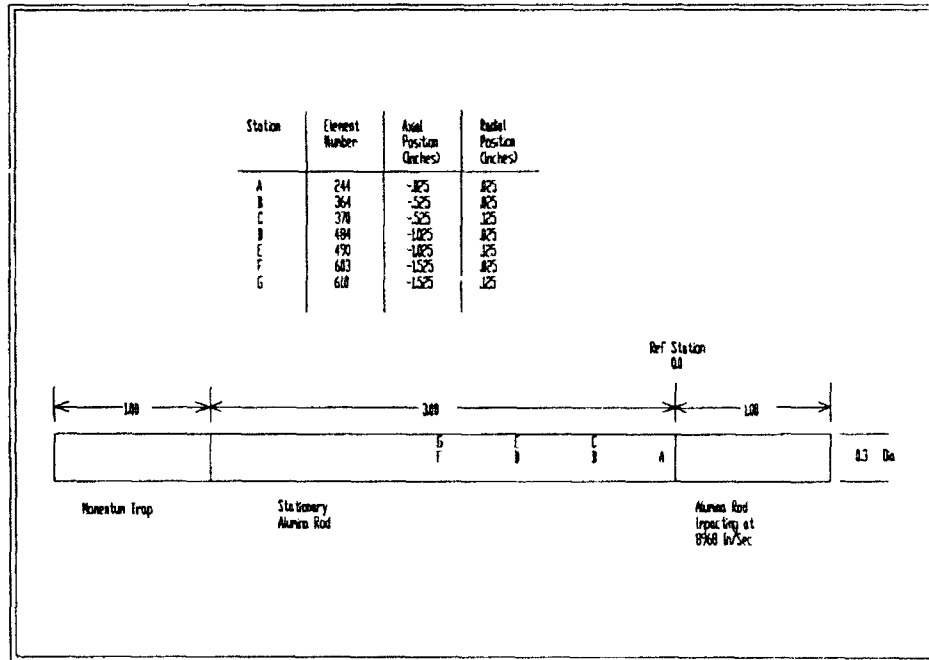


Figure 61. Rod-on-Rod Calculation, Test 22



Figure 62. Calculated Rod Impact Sequence



Figure 63. Recovered Target Rod Damage

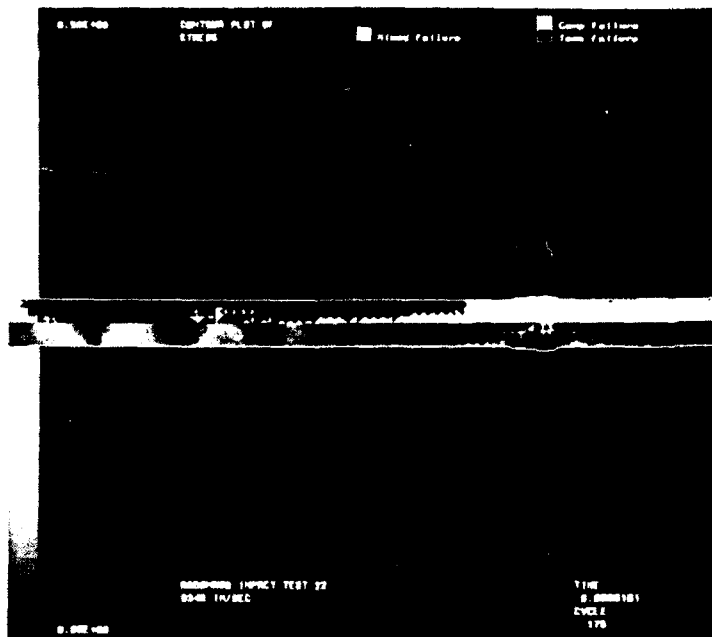


Figure 64. Calculated Target Rod Damage

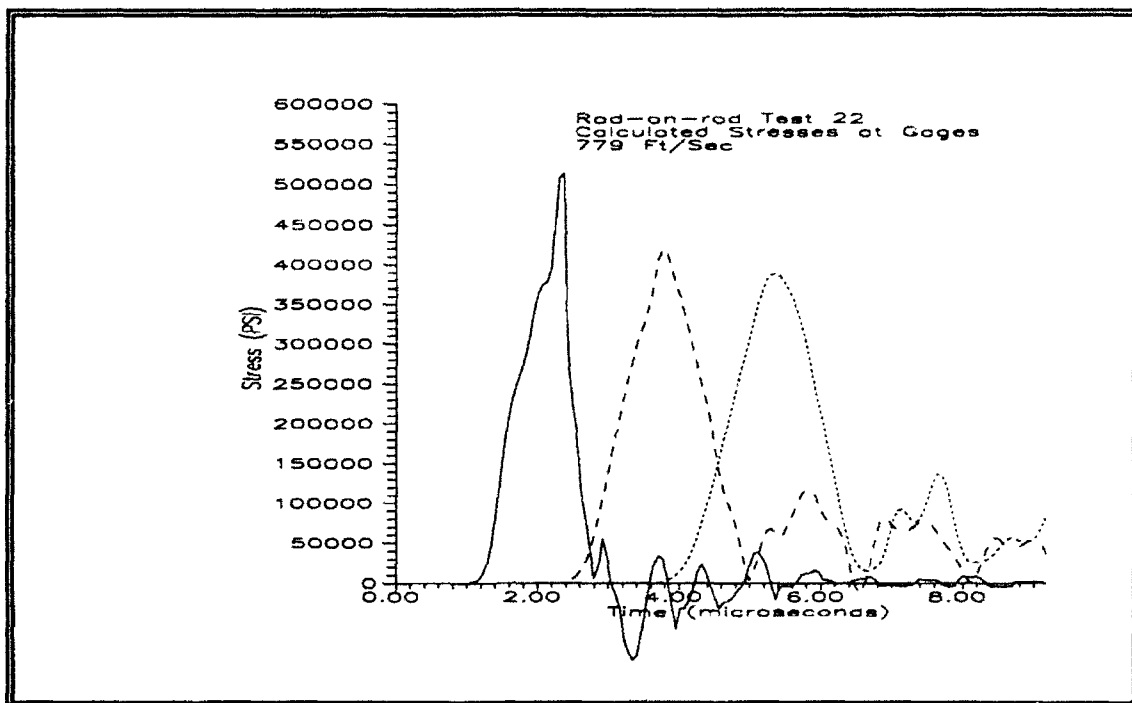


Figure 65. Calculated Axial Stress, Test 22

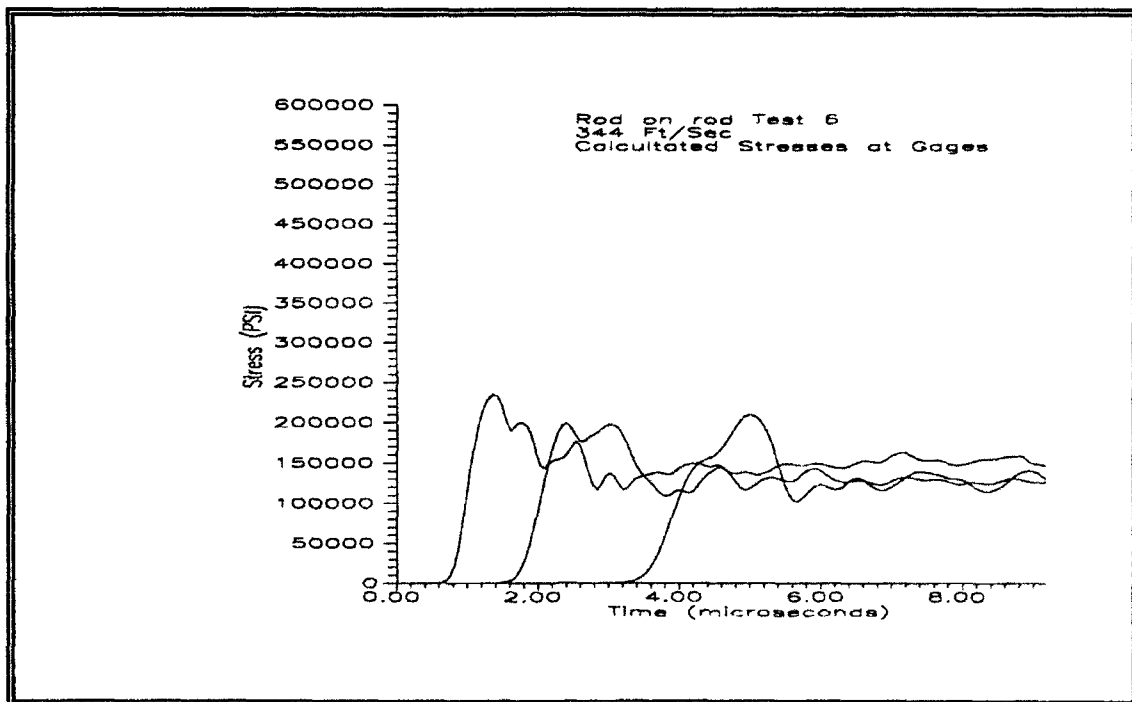


Figure 66. Calculated Axial Stress, Test 6

## Penetration Predictions

### Computational Model

Figure 67 shows the calculational model employed to study the impact and penetration experiments. The setup used a total of 3841 nodes and 7288 elements with 5 sliding surfaces. The most critical sliding surface was placed between the front of the impacting rod and the front surface of the ceramic. This slide line, and all other slide lines in this calculation used the dual pass option, using each side of the interface as the master and then the slave surface. All slide lines were also without friction. The second slide line was between the side of the rod and the inside diameter of the hole in the metal cover plate. The third slide line was between the back of the front metal cover plate and the front surface of the ceramic. The fourth and fifth slide lines were between the steel confining ring and the epoxy, and between the back cover plate and the rear surface of the ceramic. These sliding surfaces permitted flow of the penetrator between the front cover plate and the ceramic, which represented the process observed from the recovered experimental targets. For a similar coarse gridded calculation, 1641 nodes and 3004 elements were used, with a four-fold reduction in elements in the ceramic.

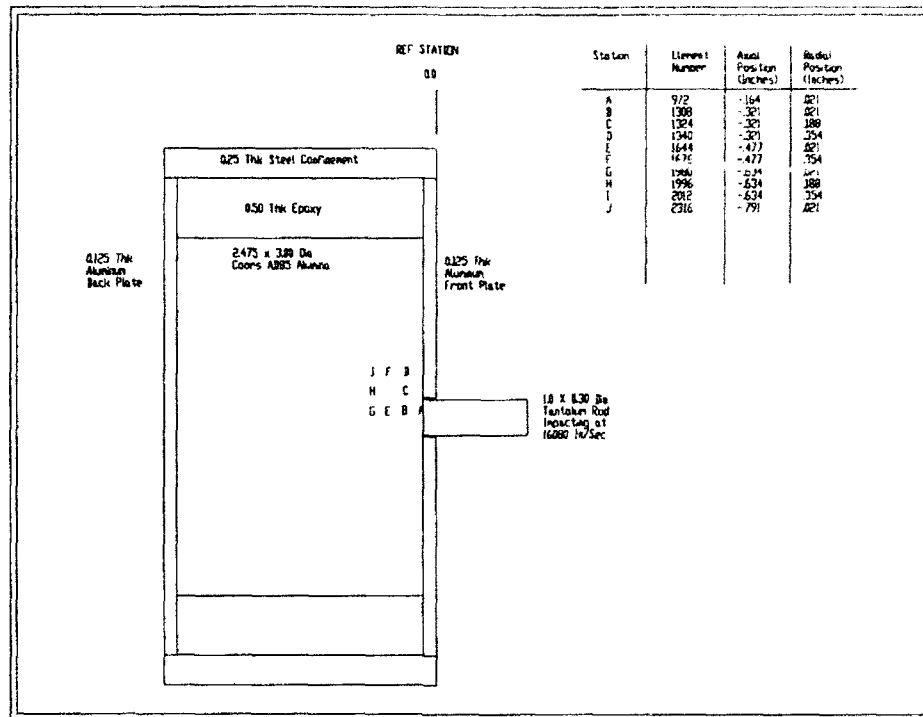


Figure 67. Penetration Calculational Configuration

### Fracture Predictions

The Fracture predictions of the proposed model are shown in Figure 68. This is a slight improvement over the results of the basic Mohr-Coulomb model shown in Figure 1. Both models significantly overpredicted the extent of the failure in the distributed failure zone near the impact point when compared to the actual experiment, test 9 shown in Figure 3. In the Hopkinson bar and rod-on-rod impact calculations, slide lines were observed to initiate unsubstantiated failure in zones adjoining the slide surfaces. Erratic stresses resulting from activity of the first slide line

(between the rod and the front surface of the ceramic) are one possible explanation for the apparently excessive failures predicted. The extending finger cracks predicted by both models showed similarities to cracks observed in the experiment. In the case of both calculations, the incomplete growth of the cracks to the rear surface was due to time and cost considerations of the calculations. In each case, the cracks were still growing when the calculation was stopped, but massive deformations of the impacting rod were controlling the time step, making completion uneconomical without resorting to computational tricks such as deleting the rod. One very significant accomplishment of the proposed model is its performance in matching the lack of cratering that occurred in the front surface of the ceramic. The recovered experimental target similarly showed virtually no penetration of the ceramic, while the Mohr-Coulomb model predicted a noticeable crater by 7.5 microseconds.

#### Zone Size Study

Figure 69 presents results of penetration predictions for a coarse grid comparable to Figure 68 for a fine grid. For this application, the failure model did not provide inconsistent results with a coarse grid, but clearly the higher resolution was necessary to describe adequately the details of the event.

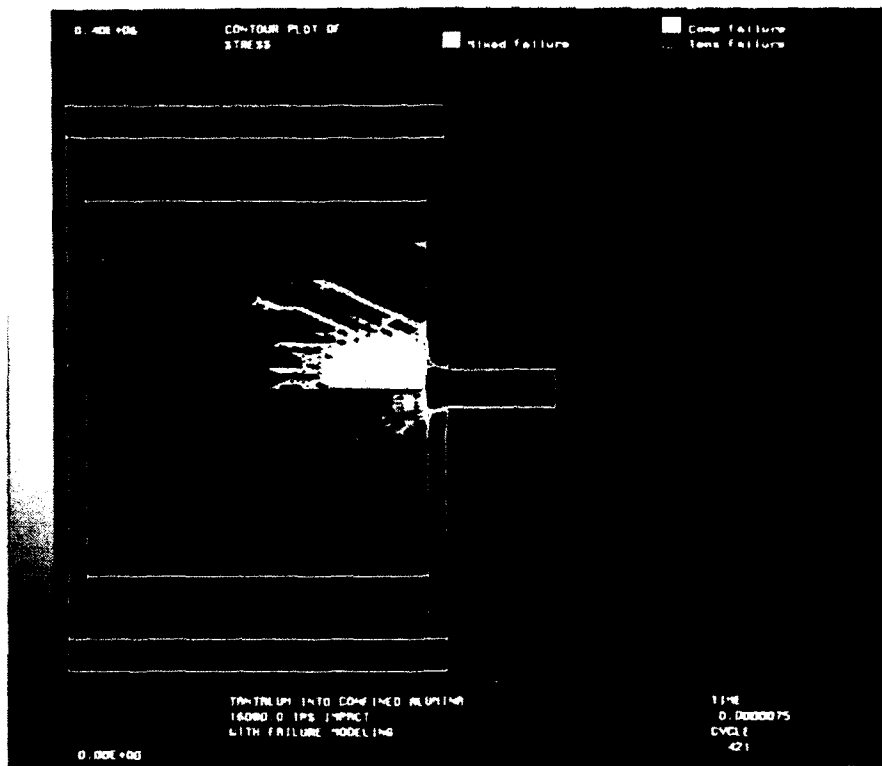


Figure 68. Calculation of Penetration Test



Figure 69. Zone Size Study for Penetration

CHAPTER 9  
SUMMARY AND CONCLUSIONS

A planned sequence of experiments encompassing various loading conditions for high velocity impact of ceramics was completed. Impulsive loads applied at different strain rates resulted in increasing failure strength with increasing strain rates. Crack growth rates were observed photographically during high velocity impact, providing bounds on crack growth rates. Macroscopic damage was observed to increase with increasing impact velocity and with increasing density of impacting material (implying higher compressive stresses under confining pressure), as well as with increasing load pulse duration. Direct observations of damage in recovered specimens were not achieved, but test measurements suggested a damage process.

Based on these experimental observations, a ceramic failure model was developed employing a pressure and strain rate dependent failure surface requiring a pressure dependent strain increment for damage and cracking. The model employed an energy based fragmentation model, and a pressure and fragment size dependent yield surface for the pulverized ceramic. This model was implemented in a hydrocode and shown to represent several critical features

in the physical response of impacted confined alumina. This model predicts failure and provides estimates of the extent of failure in terms of fragment sizes, feeding back into the constitutive model for the ceramic in the manner essential to allow accurate predictions of loading on a penetrator.

Where the objectives of future research are to establish the predominant micromechanical processes involved in ceramic failure, a model material other than AD85 would be desirable. The variations in the material characteristics within AD85 masked micromechanical damage to the extent that exact micromechanisms remain unclear. It is likely that multiple mechanisms are occurring due to the complexity of the material, but this conclusion remains speculative.

APPENDIX  
DETERMINATION OF MATERIAL CONSTANTS

Chapter 8 provided general information on the determination of the eleven material constants required by the proposed model. However, detailed procedures on the method used to perform iterative calculations on rod-on-rod impact tests to obtain the values of seven of the constants were not discussed. The procedures followed are outlined below, since they could be helpful to other users of the proposed model to validate the constants provided, to determine comparable constants for alumina from further testing, and to determine constants for other materials.

As described in Chapter 8, SIGMAT and SIGMAC were taken from the manufacturer's literature, with SIGMAC validated by tests described in Chapter 5. The value of EDOTC was determined based on quasi-static compression tests and compressive split Hopkinson pressure bar tests also described in Chapter 5. The value of K1C was taken from manufacturer's data.

The values of material constants PRESC1, PRESC2, FGMIN, FGMAX, FAILE, CRACKE, and PSTRN were determined from iterative calculations based primarily on the rod-on-rod tests. The value of PSTRN was fixed at approximately the

largest mean-pressure observed in the rod-on-rod tests, which was 140,000 PST. The value of FGMIN was set near zero, and the value of FGMAX was set near the maximum expected density of fragments for the rod-on-rod tests. PRESC1 was set to zero, and PRESC2 was set to three. With these values fixed, the rod-on-rod calculation for test 22 was run with attention directed at the peak stresses at each stress gage and the shape of the falling stress measurement. The value of CRACKE was adjusted to provide the best comparison with the peaks, and the value of FAILE was adjusted for the falling portion of the curve. Once these values provided calculations nearly matching test 22, test 6 was considered, followed by selected other rod-on-rod tests. Where residual stresses remained after the peak, the values of FGMAX and PRESC1 were adjusted followed by FGMIN and PRESC2 to achieve the best comparisons.

When a reasonably good comparison was reached for the rod-on-rod tests, the selected constants were used for calculations of Hopkinson bar tests 1 and 6. Values of FGMAX and PRESC1 were adjusted followed by FGMIN and PRESC2 where required to provide unloading on failure as observed in the transmitted stress signal. These values were then used in repetitions of the rod-on-rod calculations, and best possible compromises were chosen.

The method of choosing constants CRACKE and FAILE outlined above resulted in clear best choices for these values. However, the values for CRACKE and FAILE would change for a different value of PSTRN, which is dependent on the maximum mean-pressure seen in the rod-on-rod tests. The best choices for the values of FGMIN, PRESC1, FGMAX, and PRESC2 were not clear. The values provided were best for the tests available here, but the sensitivity of the calculations to variations over the range suggested was small.

## REFERENCES

1. L. M. VanVlack, ELEMENTS OF MATERIALS SCIENCE, Addison-Wesley Publishing Company, Reading, MA, 1967
2. R. Kinslow, HIGH VELOCITY IMPACT PHENOMENA, Academic Press, New York, 1970
3. M. L. Wilkens, in BALLISTIC MATERIALS AND PENETRATION MECHANICS, edited by R. C. Laible, Elsevier Publishing Company, New York, 1980
4. M. Mayselless, W. Goldsmith, S. P. Virostek, and S. A. Finnegan, "Impact on Ceramic Targets," J Appl Mech, 54, pp 373-378, June 1987
5. J. F. Mescall and C. A. Tracy, "Improved Modeling of Fracture in Ceramic Armors," Army Science Conference, Ithaca, NY, June 1986
6. A. A. Griffith, "Theory of Rupture," Proceedings of the 1st International Conference on Applied Mechanics, Delft, pp 55-63, 1924
7. National Material Advisory Board Committee on Fracture in Compressive Stress Fields, "Fracture in Compression of Brittle Solids," NMAB-404, National Academy of Science, Washington, DC, Aug 1983
8. Z. Rosenberg, "Dynamic Uniaxial Stress Experiments on Alumina with in-material Manganin Gauges," J Appl Phys, 57(11), pp 5087-5088, Jun 1985
9. D. R. Curran, L. Seaman, and D. A. Shockey, "Dynamic Failure of Solids," Physics Reports, 147(5-6), pp 253-388, 1987
10. G. R. Johnson, "Users Instructions for the EPIC-2 Code," AFATL-TR-86-51, Air Force Armament Laboratory, Eglin AFB, FL, 1986
11. G. R. Johnson, "Analysis of Elastic-Plastic Impact Involving Severe Distortion," J Appl Mech, 98, pp 439-444, Sept, 1976

12. M. E. Bachman, TERMINAL BALLISTICS, Naval Weapons Center, China Lake, CA, 1976
13. M. E. Bachman and W. Goldsmith, "The Mechanics of Penetration of Projectiles into Targets," Int J Eng Sci, 16, pp 1-99, 1978
14. J. A. Zukas, T. Nicholas, H. F. Swift, L. B. Greszczuk, and D. R. Curran, IMPACT DYNAMICS, John Wiley and Sons, New York, 1982
15. J. S. Wilbeck, C. E. Anderson, A. B. Wenzel, P. S. Westine, and U. S. Lindholm, course notes for "A Short Course on Penetration Mechanics," Southwest Research Institute, San Antonio, TX, 1986
16. M. Ravid, S. R. Bodner, and I. Holcman, "Application of Two-Dimensional Analytic Models of Ballistic Penetration to Ceramic Armor," Proceedings of the Eleventh International Symposium on Ballistics, Brussels, Belgium, May 1989
17. A. A. Griffith, "The Phenomenon of Rupture and Flow in Solids," Phil Trans Roy Soc, A221, p 163, 1921
18. W. F. Chen and A. F. Saleeb, CONSTITUTIVE EQUATIONS FOR ENGINEERING MATERIALS VOLUME I: ELASTICITY AND MODELING, John Wiley & Sons, New York, 1982
19. W.F.Chen, PLASTICITY IN REINFORCED CONCRETE, McGraw-Hill, New York, 1982
20. D. R. Curran, L. Seaman, and D. A. Shockey, "Dynamic Failure of Solids," Physics Reports, 147(5-6), pp 253-388, 1987
21. D. R. Curran, L. Seaman, and D. A. Shockey, "Dynamic Failure of Solids," Physics Reports, 147(5-6), pp 253-388, 1987
22. D. E. Grady, "Local Inertia Effects in Dynamic Fragmentation," J Appl Phys, 53(1), pp 322-325, 1982
23. D. E. Grady and M. E. Kipp, "The Micromechanics of Impact Fracture of Rock," Intl J Rock Mech and Mining Sci, 16(5), pp 293-302, Oct 1979
24. D. E. Grady, "The Spall Strength of Condensed Matter," J Mech Phys Solids, 36(3), pp 353-384, 1988
25. S. P. Timoshenko and J. N. Goodier, THEORY OF ELASTICITY, McGraw-Hill, New York, 1934

26. S. Nemat-Nasser and H. Horii, "Compression-Induced Nonplanar Crack Extension with Application to Splitting, Exfoliation, and Rockburst," J Geophys Res, 87, pp 6805-6821, 1982
27. H. Horii and S. Nemat-Nasser, "Compression-Induced Microcrack Growth in Brittle Solids: Axial Splitting and Shear Fault," J Geophys Res, 90(B4), pp 3105-3125, Mar 1985
28. H. Horii and S. Nemat-Nasser, "Brittle Failure in Compression: Splitting, Faulting and Brittle-Ductile Transition," Phil Trans Royal Soc, 319(1549), pp 337-374, 16 Sept 1986
29. J. Lankford, "Mechanisms Responsible for Strain-Rate-Dependent Compressive Strength of Ceramic Materials," J Amer Ceramic Society, 64, pp C33-C34, Feb 1981
30. J. Lankford, "Compressive Strength and Microplasticity in Polycrystalline Alumina," J of Mat Sci, 12, pp 791-796, Dec 1977
31. G. Vekinis, M. F. Ashby, and P. W. R. Beaumont, "Direct Observation of Fracture and the Damage Mechanics of Ceramics," CUED/C-MATS/TR 174, Engineering Dept, Cambridge Univ, Cambridge, England, March 1990
32. Coors Ceramics Bulletin No 953, Coors Porcelain Company, Golden, Colorado
33. C. E. Anderson and S. R. Bodner, "The Status of Ballistic Impact Modeling," Third TACOM Coordinating Conference, Naval Post Graduate School, Monterey, CA, 1987
34. W. H. Gust and E. B. Royce, "Dynamic Yield Strength of B4C, BeO, and Al<sub>2</sub>O<sub>3</sub>," J Appl Phys, 42(1), pp 276-295, 1971
35. D. E. Munson and R. J. Lawrence, "Dynamic Deformation of Polycrystalline Alumina," J Appl Phys, 50(10), pp 6272-6282, Oct 1979
36. Z. Rosenberg and Y. Yeshurun, "Release Behavior of Shock Loaded Commercial Alumina," J Appl Phys, 60(5), pp 1844-1846, Sept 1986
37. R. Arrowood and J. Lankford Jr, "Dynamic Characterization of and Alumina Ceramic," Southwest Research Institute, San Antonio, TX, 1982
38. B. R. Lawn, "Physics of Fracture," J Amer Ceramic Society, 66(2), pp 83-91, Feb 1983

39. A. G. Evans, FRACTURE IN CERAMIC MATERIALS, Noyes Publications, Park Ridge, NJ, 1984
40. D. Yaziv, "Shock Fracture and Recompaction of Ceramics," PhD Dissertation, University of Dayton, Dayton, OH, 1985
41. M. L. Wilkens, C. F. Cline, and C. A. Honodel, "Fourth Annual Report of Light Armor Program," UCRL-50694, Lawrence Livermore Laboratory, 1969
42. M. L. Wilkens, in BALLISTIC MATERIALS AND PENETRATION MECHANIC, edited by R. C. Laible, Elsevier Publishing Company, New York, 1980
43. D. G. Brandon, "Fracture and Dynamic Loading," in MATERIALS AT HIGH STRAIN RATES, Chapter 5, edited by T. Z. Blazynski, Elsevier Publishing Company, London, 1987
44. D. G. Brandon, "Mechanisms of Dynamic Failure in Debased Alumina," conference "Ceramic Microstructures '86: The Role of Interfaces," Berkley, CA, 1986
45. J. Sternberg, "Material Properties Determining the Resistance of Ceramics to High Velocity Penetration," J Appl Phys, 65(9), pp 3417-3424, 1 May 1989
46. D. Yaziv, Y. Yeshurun, Y. Partom, and Z. Rosenberg, "Shock Strength and Precursor Decay in Commercial Alumina," in SHOCK WAVES IN CONDENSED MATTER 1987, Elsevier Science Publishers B. V., Amsterdam, The Netherlands, 1988
47. Y. Yeshurun, D. G. Brandon, A. Venkert, and Z. Rosenberg, "The Dynamic Properties of Two-Phase Alumina/Glass Ceramics," Journal De Physique, C3, pp 11-18, Sept 1988
48. J. Cagnoux and F. Longy, "Is the Dynamic Strength of Alumina Rate Dependant?," in SHOCK WAVES IN CONDENSED MATTER 1987, Elsevier Science Publishers B. V., Amsterdam, The Netherlands, 1988
49. J. Cagnoux and F. Longy, "Spallation and Shock-Wave Behaviour of some Ceramics," Journal De Physique, C3, pp 3-10, Sept 1988
50. S. J. Bless, "Impact Behavior of Ceramics," Workshop on Dynamic Constitutive/Failure Models, AFWAL-TR-88-4229, Dayton, Ohio, 1988

51. A. M. Rajendran and W. H. Cook, "A Comprehensive Review of Modeling of Impact Damage in Ceramics," AFATL-TR-88-143, Air Force Armament Laboratory, Eglin AFB, FL, Dec 1988
52. M. A. Dietsenberger, A. M. Rajendran, and D. J. Grove, "A Use of Microphysical Fracture Model to Describe Ceramic Material upon Impact," 1989 American Physical Society Topical Conference on Shock Compression of Condensed Matter, Albuquerque, NM, 1989
53. J. L. Kroupa and A. M. Rajendran, "The Use of Grady-Kipp type Fragmentation Model to Describe the Impact Behavior of Ceramic Materials," 1989 American Physical Society Topical Conference on Shock Compression of Condensed Matter, Albuquerque, NM, 1989
54. A. M. Rajendran and J. L. Kroupa, "Impact Damage Model for Ceramic Materials," J Appl Phys, 66(8), pp 3560-3565, 15 Oct 1989
55. J. R. Furlong and M. L. Alme, "Numerical Modeling of Ceramic Penetration Experiments," TACOM Armor Coordinating Conference for Light Combat Vehicles, Naval Postgraduate School, Monterey, CA, March 1988
56. M. E. Kipp and D. E. Grady, "Numerical Studies of Rock Fragmentation," SAND79-1582, Sandia National Laboratories, Albuquerque, NM, 1978
57. L. N. Taylor, E. P. Chen, and J. S. Kuszmaul, "Microcrack-Induced Damage Accumulation in Brittle Rock under Dynamic Loading," Comp Meth in Appl Mech and Eng, 55, pp 301-320, 1986
58. F. L. Addessio and J. N. Johnson, "A Constitutive Model for the Dynamic Response of Brittle Materials," LA-UR-89-2651, Los Alamos National Laboratory, 1989
59. S. Chung, "Fracture Characterization of Armor Ceramics," Ceramic Bulletin, 69(3), pp 358-365, 1990
60. L. H. L. Louro, "Stress-Wave Induced Damage in Alumina-Based Ceramics," PhD Dissertation, Department of Materials and Metallurgical Engineering, New Mexico Institute of Mining and Technology, Socorro, NM, July 1988
61. G. R. Johnson and T. J. Holmquist, "A Computational Constitutive Model for Brittle Materials Subjected to Large Strains, High Strain Rates, and High Pressures," EXPLOMET Conference, San Diego, CA, August 1990

62. G. R. Johnson and W. H. Cook, "A Constitutive Model and Data for Metals Subjected to Large Strains, High Strain Rates, and High Temperatures," Proceedings of the Seventh International Symposium on Ballistics, The Hague, The Netherlands, 1983
63. G. R. Johnson and W. H. Cook, "Fracture Characteristics of Three Metals Subjected to Various Strains, Strain Rates, Temperatures, and Pressures," Engineering Fracture Mechanics, 21(3), pp 31-48, 1985
64. G. R. Johnson, "Implementation of Simplified Constitutive Models in Large Computer Codes," Workshop on Dynamic Constitutive/Failure Models, AFWAL-TR-88-4229, Dayton, Ohio, 1988
65. D. Steinberg, "Computer Studies in the Dynamic Strength of Ceramics," UCRL-ID-106004, Lawrence Livermore National Laboratory, Sept 1990
66. R. L. Sierakowski, L. E. Malvern, and C. A. Ross, "Compression Testing of Metals at Elevated Temperatures," AFATL-TR-80-76, Air Force Armament Laboratory, Eglin AFB, FL, June 1980
67. R. J. Clifton, G. Raiser, M. Ortiz, and H. Espinosa, "A Soft Recovery Experiment for Ceramics," 1989 American Physical Society Topical Conference on Shock Compression of Condensed Matter, Albuquerque, NM, 1989
68. R. T. DeHoff and F. N. Rhines, QUANTITATIVE MICROSCOPY, McGraw-Hill Book Company, New York, 1968
69. L. H. Bakken and P. D. Anderson, "An Equation of State Handbook (Conversion Relations Between the WONDY/TOODY and the PUFF/KO/HEMP Classes of Shock Wave Propagation Computer Codes," SCL-DR-68-123, Sandia Laboratories, Livermore, CA, Jan 1969

DISTRIBUTION

Defense Technical Info. Center  
Attn: DTIC-DDAC  
Cameron Station  
Alexandria VA 22304-6145  
2

AUL/LSE  
Maxwell AFB AL 36112-5564  
1

WL/MNOI (Scientific and Tech. Info. Facility)  
Eglin AFB FL 32542-6843  
1

WL/MNMW  
Attn: William Cook  
Eglin AFB FL 32542-6810  
3

AFDTC/PA  
Eglin AFB FL 32542-5000  
1